

# **Improving Fine Grid Meteorological Simulations for Air Quality Applications**

Phase 2 Final Report

For

**CRC Project Number A-46**

Submitted to:

Mr. Brent K. Bailey  
Coordinating Research Council  
3650 Mansell Road, Suite 140  
Alpharetta, GA 30022

by

David R. Stauffer and Aijun Deng

Department of Meteorology  
The Pennsylvania State University  
University Park, Pennsylvania 16802

Technical Contact: David R. Stauffer, (814)863-3932, [stauffer@mail.meteo.psu.edu](mailto:stauffer@mail.meteo.psu.edu), FAX (814)865-3663

January 20, 2006

## **ABSTRACT**

A previous inter-regional transport study funded by the Coordinating Research Council (CRC A-28) was conducted by Penn State University using the fifth generation of the Penn State University (PSU) /National Center for Atmospheric Research (NCAR) mesoscale model (MM5). This study was based on the 18-19 September 1983 Cross Appalachian Tracer Experiment (CAPTEX) case. It was found that use of four-dimensional data assimilation (FDDA), along with 12-km model resolution (horizontal grid spacing) and improved model physics, produced the overall best performance. However, further reduction of the model grid length from 12 km to 4 km had detrimental effects on the meteorological and plume dispersion solutions. The primary cause of the poor mesoscale model performance was likely due to the explicit (grid-resolved) representation of convective precipitation accompanying a cold front advancing across the lower Great Lakes and into New England. Because no convective parameterization scheme (CPS) was used on the 4-km grid, the convective updrafts were forced on coarser-than-realistic scales (normal updraft diameter for most storms in the eastern United States is ~ 2 km), and the rainfall and the atmospheric response to the convection were too strong. The evaporative cooling and the associated downdrafts from these unrealistic convective systems also known as “grid-point storms” were too vigorous causing widespread disruption of the low-level winds and spurious transport of the simulated tracer.

To continue the research investigating the “grid-point storm” problem and improving the 4-km resolution mesoscale model simulations building on lessons learned in Phase 1 of CRC A-46 project, ten new mesoscale modeling experiments have been designed and applied in the CAPTEX case study in this second phase of the project. Four MM5 experiments and six experiments using the new Weather Research and Forecast (WRF) model were performed. Since

no FDDA capability is available for WRF at this time, FDDA was not used in any of the ten experiments.

Some of the conclusions of Phase 2 include: 1) MM5 and WRF precipitation amounts although reduced in this study were still too large on the 4-km domain likely due to grid-point storm issues; 2) MM5 and WRF precipitation patterns were different due to different phase errors in the frontal positions, and the fact that FDDA was not used in either model; 3) Although still too large in all experiments likely due to grid-point storm issues, the simulated precipitation amounts were generally reduced in both models by use of a CPS directly on 4-km domain. The underlying assumptions of the CPS normally preclude its use on model domains with grid resolutions finer than  $\sim 10$  km. However, use of a CPS on the 4-km domain may mitigate some of the grid-point storm problems, especially when the spurious convection was very intense and caused anomalous low-level wind flows. Thus, use of a CPS may help reduce the occurrence of unrealistic mesoscale convective systems (MCSs); 4) Although there were no observations to verify the model-simulated planetary boundary layer (PBL) depths, comparison of PBL depths among all ten experiments indicated that the new Yonsei University (YSU) PBL scheme appears to give a PBL depth that is artificially low (lowest model layer) at night time and possibly too high during the daytime with values comparable to those using the Medium Range Forecast (MRF) model PBL in MM5; 5) Overall the MM5 and WRF statistical results were comparable. Use of a CPS directly on the 4-km domain showed some improvements in both models in the statistical results for the mass and wind fields, although the improvements were relatively small and not consistent over all layers and all variables; 6) A fair and direct comparison between the MM5 and WRF models was made for this one case using the same domains, initial conditions and lateral boundary conditions, and comparable model physics, and it was found that WRF

appears to have slightly better performance in the wind field, especially the speed. For the model-simulated temperature field, both models had very similar scores, with MM5 being better in some model layers and WRF being better in other layers. Overall, MM5 was somewhat better than WRF in the simulated temperature fields and sea-level pressure fields. For moisture, WRF was slightly better than the MM5. The statistical differences between the two models without FDDA were again relatively small and suggest that there was no clear advantage of one model over the other for this case.

However, it must be pointed out that this is only one case study, but this case is representative of mid-latitude frontal rain and deep convection cases, so these results should be generally representative of other cases. Additional cases are still needed to determine the general added value of this research.

It has been proven in Phase 1 of this project that FDDA can significantly reduce the model errors. It is extremely important to revisit this subject in WRF in the future. However, WRF does not currently have a FDDA capability to nudge the model solutions to either gridded analysis fields or to individual observations. Thus, the recommendations to CRC for future work based on this research should include development of a nudging capability in WRF, in addition to development of a shallow/deep cumulus parameterization scheme suitable for 4-km resolution modeling.



## TECHNICAL SUMMARY

To further study how to improve 4-km mesoscale model simulations by building on lessons learned in Phase 1 of CRC A-46 project, ten new modeling experiments (four MM5 and six WRF) were designed and applied to a case study in this second phase of the project. Both subjective and objective evaluations have been performed on the model-simulated fields. Subjective evaluation again focused on the model-simulated precipitation field and the surface-layer winds, temperature and sea-level pressure at model hours 21 h (09 UTC 19 September 1983) and 30 h (18 UTC 19 September 1983). The 21-h time represented a night-time period when a mid-latitude frontal system was moving eastward across the northeast US on the 4-km domain, and the 30-h time was a day-time period when intense convective systems formed along the front and caused widespread distortion in the low-level wind flow and mass fields. Objective evaluation was performed by comparing the mean absolute error (MAE) and mean error (ME) distributions (over time at the surface vs. all vertical layers for the 30-h case period) of the model-simulated wind speed, wind direction, vector wind difference, temperature, water vapor mixing ratio and sea-level pressure for all ten model experiments. The conclusions drawn from this second phase of the research include the following:

- 1) Subjective evaluation showed that MM5 and WRF model precipitation amounts were still too large on the 4-km domain likely due to grid-point storm issues. Table 3 and Fig. 37 summarize the 4-km domain maximum 3-hourly precipitation for all ten experiments ending at 21 h and 30 h, and also the 30-h total maximum precipitation for each experiment. The observed precipitation within the 4-km

model domain was generally less than 5 or 10 mm at both model analysis times, and the maximum total precipitation for any location within the 4-km domain was surely less than 20 – 25 mm (1 inch) while the total model-simulated maximum precipitation amounts ranged from 66.7 mm to 128 mm (Table 3). The figure shows that the maximum precipitation was generally reduced at all three ending times by applying a convective parameterization scheme (CPS) on the 4-km domain. One possible exception was Exp. WS2 (WRF using the Yonsei University (YSU) planetary boundary layer (PBL) scheme) in which the precipitation coverage and intensities were increased at both the 21-h and 30-h times when the Kain-Fritsch (KF) scheme was applied to the 4-km domain, but they were reduced for the 30-h total maximum.

In general, the WRF experiments had comparable or somewhat smaller precipitation amounts compared to those from the MM5, but they were all still too large. Thus although precipitation is still overestimated by both models, the amounts were generally reduced or not significantly increased in the experiments applying CPS directly on the 4-km domain.

- 2) MM5 and WRF precipitation patterns were quite different at the two analysis times despite their using the same model initial conditions and lateral boundary conditions, and very similar model physics. The location of the cold front and the intensity and distribution of the precipitation varied widely among the experiments due to different phase errors in the frontal positions, and the fact that

FDDA was not used in either model in this study. A fair and direct comparison between MM5 and WRF was made based on Exps. MS12, MS12KF, WB2 and WB2KF. It was found that at the 21-h time, the precipitation in MM5 was more intense than that in WRF over the Lake Erie region. Precipitation in WRF was located more over the region to the northeast of Lake Ontario in Canada. Observed precipitation at this time was zero or very light. The model-simulated cold fronts were generally too slow for the northern / eastern end and too fast for the southern / western end. Those experiments that produced less rain to the south and west of Lake Huron also produced a better frontal location there. The cold frontal phase error, precipitation amounts and coverage, and the western (back) edge of the frontal precipitation were generally improved by using the CPS directly on the 4-km domain for most of the experiments except WRF WS2 using YSU PBL and WS3 using Grell CPS.

At the 30-h time, most of the precipitation in MM5 was located over Lake Erie and northern Ohio (OH) region, but it was located further north across the southern tip of Lake Huron or western New York (NY) in some WRF experiments. Use of the CPS on the 4-km domain improved the surface wind and temperature fields near Lake Erie at this time in MM5. The front in the WRF experiments was too slow and caused the precipitation at this time to occur further to the north and west than MM5 with southwesterly flow across Lake Erie where observed surface winds were from the northwest. The MM5 simulations, on the other hand, especially the one using KF CPS on the 4-km domain, reproduced the

northwesterly flow over Lake Erie and the southwesterly flow to the south of the front. When the precipitation amounts and coverage were reduced by adding the CPS on the 4-km domain, the surface cold pools and wind anomalies were also weakened.

- 3) It was shown that use of CPS on the 4-km domain in MM5 and WRF may mitigate some of the grid-point storm problems, especially when the spurious convection is very intense and causes anomalous low-level wind and mass fields, while at the same time either improving the simulations or at least not significantly changing the wind and mass fields (Tables 4-7 and Figs. 38 and 39). Use of a CPS on the 4-km domain may reduce the risk that a model produces strong grid point storm issues such as the occurrence of intense and unrealistic mesoscale convective systems (MCSs) as clearly seen in Phase 1 of the study. Use of a CPS directly on the 4-km domain showed some improvements in this study in both models in the mass and wind field statistical results, although the improvements were relatively small and may not be consistent over all layers and all variables.
- 4) Although there were no observations to verify the model-simulated PBL depths, a comparison of PBL depth among all ten experiments for both day-time and night-time periods indicated that the YSU PBL scheme gives a PBL depth that is artificially low (height of first full model layer, 32 m) at night time and likely too high during the day time with values comparable to those in MM5 using the MRF

PBL (~950 m, see Stauffer and Deng 2004). Comparison between both turbulent kinetic energy (TKE)-based PBL schemes (GS PBL and Eta PBL) showed that the GS PBL scheme produced lower PBL depths at night time compared with the Eta PBL scheme, while during the day time, a cold bias at the surface in the Eta PBL experiments contributed to lower PBL depths compared to the other experiments.

- 5) Overall the MM5 and WRF statistical results for the wind and mass fields were generally comparable as shown in Tables 4-7 and Figs. 38 and 39, but some differences are noted. Comparison of the MAE score of model-simulated surface layer wind speed for all ten experiments indicated that the WRF experiment set using the YSU PBL scheme (WS2 and WS2KF) was the worst ( $\sim 2.4 - 2.5 \text{ ms}^{-1}$ ), and the WRF experiment set using M-Y-J Eta TKE PBL physics and either the KF or Grell CPS (WB2KF and WS3GR) was the best ( $1.8 - 1.9 \text{ ms}^{-1}$ ) (see Table 4 and Fig. 38). For wind speed over all layers, Table 6 and Fig. 39 show the MM5 experiment set using GS TKE PBL scheme and KF CPS was the worst ( $2.0 - 2.2 \text{ ms}^{-1}$ ) and the WRF experiments using M-Y-J TKE PBL were the best ( $1.7 - 1.9 \text{ ms}^{-1}$ ). Thus the difference between the worst and best experiments was only around  $0.3 \text{ ms}^{-1}$ . The best surface wind directions were produced by WB2KF but they were less than 1 degree better than the worst experiment (Table 4 and Fig. 38). For all layers, Table 6 and Fig. 39 show WRF had a slight advantage in wind direction by less than 1 degree. In general, the MAE and ME wind direction scores for all ten experiments were very similar, with the WRF experiment set

using M-Y-J TKE PBL physics and Grell CPS and the MM5 experiment set using GS TKE PBL and KF CPS having slight advantage in the boundary layer (Fig. 30).

Comparison of the MAE score of model-simulated temperature field (both surface layer and all layers) for all ten experiments indicated that the MM5 experiment set using GS TKE PBL (MS11 and MS11KF) was the best, and the WRF experiment set using M-Y-J TKE PBL physics and Grell CPS (WS3 and WS3GR) was the worst with around 0.6 °C larger errors at the surface and 0.2 °C larger errors over all layers (Tables 4 and 6, Figs. 38 and 39). Similarly, the MM5 experiment sets MS11 and MS12 produced the best sea-level pressure statistics (~0.9 – 1.0 hPa) while the WS3 experiments produced the worst sea-level pressure scores by about 0.3 hPa. For the model-simulated surface layer water vapor mixing ratio field, the MM5 MS11 experiment set using GS TKE PBL and KF CPS was the best by about 0.1 g kg<sup>-1</sup> (Table 4 and Fig. 38). For all layers, the WRF WS2 experiment set using YSU PBL scheme produced slightly smaller errors (0.1 – 0.2 g kg<sup>-1</sup>) in vapor mixing ratio than the other experiments (Table 6 and Fig. 39).

- 6) A direct and fair comparison between the MM5 and WRF models was made using Exps. MS12, MS12KF, WB2 and WB2KF. It was found that WRF appears to have somewhat better performance in the wind speed field (0.1 – 0.2 ms<sup>-1</sup>), and wind direction differences between MM5 and WRF were less than 1 degree in magnitude on average (Tables 4 and 6, Figs. 38 and 39). For the model-simulated

temperature field, both models had very similar scores, with MM5 being slightly better overall by about 0.1 °C with MM5 being better in some model layers and WRF being better in some other layers. For moisture, WRF was slightly better than MM5 over all layers by about 0.1 g kg<sup>-1</sup>. Again, the statistical differences between these two models without FDDA were relatively small and suggest that there was no clear advantage of one model over the other for this case. WRF was slightly better in the wind fields and slightly worse in the mass fields. The Eta PBL had an advantage in simulating wind speed compared to GS PBL but the mass fields were much better simulated by the GS PBL. The YSU PBL (Exps. WS2 and WS2KF) produced the worst wind statistics at the surface and appeared to over smooth the surface horizontal wind fields compared to the other experiments.

However, it must be pointed out that this is only one case study, but this case is representative of mid-latitude frontal rain and deep convection cases, so these results should be generally representative of other cases. Additional cases are still needed to determine the general added value of this research.

Note that use of a convective sub-grid physics scheme at 4-km resolution for deep (precipitating) convection violates the underlying assumption that the size of the updraft being parameterized is much smaller than the grid size. It is also clear that in general, explicit microphysics alone cannot completely represent deep convection on these 4-km grid scales and some type of parameterization is needed. Since there is no readily identifiable approach to do this, this presents a serious dilemma when using 4-km grids to simulate deep convective

environments. The results presented here show that use of a CPS on the 4-km grid may still be helpful in these situations where 4-km resolution is desired and explicit microphysics alone produces grossly unrealistic precipitation amounts.

The results produced from this research continue to point to our need for development of a new CPS appropriate for application on these very fine scales which are still too coarse for purely resolved-scale explicit-moisture approaches. It is possible that application of an existing CPS on these finer scales may mitigate some of the grid-point storm problems, especially when the spurious convection is very intense and causes anomalous low-level wind flows. Application of a CPS on the 4-km domain causing a slight degradation in the model solution in some layers and in some fields may still be acceptable if it minimizes the potentially significant damage caused by an otherwise intense grid-point storm. Further experimentation with higher resolution models with grid lengths of say 1 – 2 km, where explicit-only approaches would be more valid, should be done for direct comparison with these 4-km results in a future study. There are other issues, however, with model physics as grid lengths approach 1 km such as using 1D versus 3D turbulence schemes, etc.

It has been proven in Phase 1 of this project that FDDA can significantly reduce the model errors. It is extremely important to revisit this subject in WRF in the future. However, WRF does not currently have a FDDA capability to nudge the model solutions to either gridded analysis fields or to individual observations. Thus, the recommendations to CRC for future work based on this research should include development of a nudging capability in WRF, in addition to development of shallow/deep cumulus parameterization scheme suitable for 4-km resolution modeling.



## TABLE OF CONTENTS

	<u>Page</u>
ABSTRACT .....	i
TECHNICAL SUMMARY .....	iv
LIST OF ACRONYMS .....	xiv
LIST OF TABLES .....	xvi
LIST OF FIGURES .....	xvii
1. INTRODUCTION .....	1
1.1 Background .....	1
1.2 Objectives .....	4
2. OVERVIEW OF THE 18-19 SEPTEMBER 1983 CAPTEX CASE .....	6
3. MODEL DESCRIPTIONS .....	8
3.1 MM5 Model .....	8
3.2 Weather Research and Forecast (WRF) Model .....	12
4. EXPERIMENT DESIGN .....	21
4.1 MM5 and WRF Model Domains .....	21
4.2 Initialization and Lateral Boundary Conditions .....	22
4.3 Model Experiments .....	23
4.3.1 Exp. WB1 .....	23
4.3.2 Exp. MS11 and MS11KF .....	24
4.3.3 Exp. MS12 and WB2 .....	25
4.3.4 Exp. MS12KF and WB2KF .....	25

4.3.5	Exp. WS2 and WS2KF .....	26
4.3.6	Exp. WS3 and WS3GR .....	27
4.4	Evaluation Procedures .....	27
5.	MODEL RESULTS .....	29
5.1	Subjective Evaluation of the MM5- and WRF-Simulated Mesoscale Features .....	29
5.1.1	21-h model time .....	30
5.1.2	30-h model time .....	37
5.2	Objective Evaluation of the MM5 and WRF Solutions Using a Statistical Approach .....	42
5.2.1	Wind Speed .....	43
5.2.2	Wind Direction .....	48
5.2.3	Vector Wind Difference .....	49
5.2.4	Temperature .....	51
5.2.5	Water Vapor Mixing Ratio .....	53
5.2.6	Sea-Level Pressure .....	55
6.	CONCLUSIONS .....	57
6.1	Summary .....	57
6.2	Limitations of the Study and Future Work .....	62
Appendix	.....	65
References	.....	66
Tables	.....	70
Figures	.....	77

## LIST OF ACRONYMS

AGL	Above ground level
ARW	Advanced research weather research and forecast model
C	Celsius
CAPE	Convective available potential energy
CAPTEX	Cross Appalachian Tracer Experiment
CAPTEX'83	Cross Appalachian Tracer Experiment of 1983
CONUS	Continental United States
CPS	Convective parameterization scheme
CRC	Coordinating Research Council, Inc.
DEG	Degree
°F	Degree Fahrenheit
FDDA	Four dimensional data assimilation
g/kg or g kg <sup>-1</sup>	Gram per kilogram
Grell CPS	Grell cumulus parameterization scheme
GS TKE PBL	Penn State Gayno-Seaman PBL scheme
hPa	Hectopascal
I	Index of agreement
kg	Kilogram
km	Kilometer
KF2	The new Kain-Fritsch convective parameterization scheme
MSn	MM5 sensitivity experiment n
WB2	WRF baseline experiment 2
WSn	WRF sensitivity experiment n
MAE	Mean absolute error
m/s or m s <sup>-1</sup>	Meter per second
ME	Mean error
mm	Millimeter
MM5	Fifth-generation Penn State/NCAR mesoscale model
MRF	Medium range forecast
MRF PBL	NCEP Hong and Pan MRF PBL scheme
M-Y-J	Mellor-Yamada-Janjic
NCAR	National Center for Atmospheric Research
NCEP	National Centers for Environmental Prediction
PBL	Planetary Boundary Layer
PSU	Pennsylvania State University
QPF	Quantitative precipitation forecast
RRTM	Rapid radiative transfer model
SFC	Surface
TKE	Turbulent Kinetic Energy
YSU	Yonsei University
States:	
CO, IA, MD, ME	Colorado, Iowa, Maryland, Maine
MI, NJ, NY, OH	Michigan, New Jersey, New York, Ohio
PA, WI	Pennsylvania, Wisconsin

UTC  
WRF

Universal time or Greenwich mean time (GMT)  
Weather Research and Forecast model

## LIST OF TABLES

Table 1	Vertical distribution of $\sigma$ (MM5) or $\eta$ (WRF) levels (half layers) and model-layer heights (m AGL) in MM5 for all four domains. Model layer vertical indexing is reversed in WRF (not shown, $k = 1$ for the surface layer) and the model layer heights in WRF (not shown) are generally similar to those in MM5 but vary in time.
Table 2	Summary of experimental design. M__ = MM5 W__ = WRF. Gray shading identifies those experiments used in the direct comparison between MM5 and WRF.
Table 3	Maximum model-simulated precipitation amounts (mm) on the 4-km domain for all experiments for the 3-hour periods ending at 21 hours (0900 UTC 19 September 1983), and 30 hours (1800 UTC 19 September 1983), and the maximum total accumulated precipitation through the entire 30-hour period. These maximum values are computed from the sum of the parameterized subgrid precipitation (if a CPS is used) and the grid-resolved (explicit) precipitation for each model experiment.
Table 4	Thirty-hour mean of the mean absolute error of the model-simulated surface-layer fields and sea level pressure (SLP). Bold values show the better entry between each no-CPS and CPS experiment pair, underlined values denote the best value within each CPS-experiment set and each no-CPS experiment set, and the asterisks indicate the best value over all experiments for each variable.
Table 5	Thirty-hour mean of the mean error of the model-simulated surface-layer fields and sea level pressure (SLP), and index of agreement of the model-simulated wind speed. Bold values show the better entry between each no-CPS and CPS experiment pair, underlined values denote the best value within each CPS-experiment set and each no-CPS experiment set, and the asterisks indicate the best value over all experiments for each variable.
Table 6	Thirty-hour mean of the mean absolute error of the model-simulated profile (32-layer) fields. Bold values show the better entry between each no-CPS and CPS experiment pair, underlined values denote the best value within each CPS-experiment set and each no-CPS experiment set, and the asterisks indicate the best value over all experiments for each variable.
Table 7	Thirty-hour mean of the mean error of the model-simulated profile (32-layer) fields and index of agreement of the model-simulated wind speed profile. Bold values show the better entry between each no-CPS and CPS experiment pair, underlined values denote the best value within each CPS-experiment set and each no-CPS experiment set, and the asterisks indicate the best value over all experiments for each variable.

## LIST OF FIGURES

- Figure 1 Standard surface weather analysis at a) 0900 UTC 19 September 1983, b) 1800 UTC 19 September 1983. Sea-level pressure contour interval is 1 hPa. One barb is  $5 \text{ m s}^{-1}$ . A color-coded station model is used for quick identification of current weather categories: Green symbols indicate reports of rain or showers, blue symbols represent frozen precipitation, red symbols denote thunderstorms, pink symbols indicate a thunderstorm nearby but not overhead, brown symbols represent obstructions to visibility (fog, haze) and black symbols indicate no significant weather.
- Figure 2 Location of 108-km, 36-km, 12-km and 4-km nested domains for MM5 and WRF experiments.
- Figure 3 Terrain (m) for the MM5 and WRF 4-km domains. Contour interval is 100 m. The solid line marks the location of the cross section used in Figs. 14 and 25.
- Figure 4 Model-simulated fields at 21 h (0900 UTC 19 September 1983) on the 4-km domain in Exp. MS11, (a) 3-h total precipitation (mm), (b) Surface-layer wind overlaid with observed surface winds ( $\text{ms}^{-1}$ ). Rain contours are 1, 5, 10 and 25 mm, speed contours are  $5 \text{ ms}^{-1}$  and one barb is  $10 \text{ ms}^{-1}$ . Observed surface front is depicted using traditional frontal symbols and model-simulated front is shown with heavy dashed line.
- Figure 5 Model-simulated fields at 21 h (0900 UTC 19 September 1983) on the 4-km domain in Exp. MS11KF, (a) 3-h total precipitation (mm), (b) Surface-layer wind overlaid with observed surface winds ( $\text{ms}^{-1}$ ). Rain contours are 1, 5, 10 and 25 mm, speed contours are  $5 \text{ ms}^{-1}$  and one barb is  $10 \text{ ms}^{-1}$ . Observed surface front is depicted using traditional frontal symbols and model-simulated front is shown with heavy dashed line.
- Figure 6 Model-simulated fields at 21 h (0900 UTC 19 September 1983) on the 4-km domain in Exp. MS12, (a) 3-h total precipitation (mm), (b) Surface-layer wind overlaid with observed surface winds ( $\text{ms}^{-1}$ ). Rain contours are 1, 5, 10 and 25 mm, speed contours are  $5 \text{ ms}^{-1}$  and one barb is  $10 \text{ ms}^{-1}$ . Observed surface front is depicted using traditional frontal symbols and model-simulated front is shown with heavy dashed line.
- Figure 7 Model-simulated fields at 21 h (0900 UTC 19 September 1983) on the 4-km domain in Exp. WB2, (a) 3-h total precipitation (mm), (b) Surface-layer wind overlaid with observed surface winds ( $\text{ms}^{-1}$ ). Rain contours are 1, 5, 10 and 25 mm, speed contours are  $5 \text{ ms}^{-1}$  and one barb is  $10 \text{ ms}^{-1}$ . Observed surface front is depicted using traditional frontal symbols and model-simulated front is shown with heavy dashed line.

- Figure 8 Model-simulated fields at 21 h (0900 UTC 19 September 1983) on the 4-km domain in Exp. MS12KF, (a) 3-h total precipitation (mm), (b) Surface-layer wind overlaid with observed surface winds ( $\text{ms}^{-1}$ ). Rain contours are 1, 5, 10 and 25 mm, speed contours are  $5 \text{ ms}^{-1}$  and one barb is  $10 \text{ ms}^{-1}$ . Observed surface front is depicted using traditional frontal symbols and model-simulated front is shown with heavy dashed line.
- Figure 9 Model-simulated fields at 21 h (0900 UTC 19 September 1983) on the 4-km domain in Exp. WB2KF, (a) 3-h total precipitation (mm), (b) Surface-layer wind overlaid with observed surface winds ( $\text{ms}^{-1}$ ). Rain contours are 1, 5, 10 and 25 mm, speed contours are  $5 \text{ ms}^{-1}$  and one barb is  $10 \text{ ms}^{-1}$ . Observed surface front is depicted using traditional frontal symbols and model-simulated front is shown with heavy dashed line.
- Figure 10 Model-simulated fields at 21 h (0900 UTC 19 September 1983) on the 4-km domain in Exp. WS2, (a) 3-h total precipitation (mm), (b) Surface-layer wind overlaid with observed surface winds ( $\text{ms}^{-1}$ ). Rain contours are 1, 5, 10 and 25 mm, speed contours are  $5 \text{ ms}^{-1}$  and one barb is  $10 \text{ ms}^{-1}$ . Observed surface front is depicted using traditional frontal symbols and model-simulated front is shown with heavy dashed line.
- Figure 11 Model-simulated fields at 21 h (0900 UTC 19 September 1983) on the 4-km domain in Exp. WS2KF, (a) 3-h total precipitation (mm), (b) Surface-layer wind overlaid with observed surface winds ( $\text{ms}^{-1}$ ). Rain contours are 1, 5, 10 and 25 mm, speed contours are  $5 \text{ ms}^{-1}$  and one barb is  $10 \text{ ms}^{-1}$ . Observed surface front is depicted using traditional frontal symbols and model-simulated front is shown with heavy dashed line.
- Figure 12 Model-simulated fields at 21 h (0900 UTC 19 September 1983) on the 4-km domain in Exp. WS3, (a) 3-h total precipitation (mm), (b) Surface-layer wind overlaid with observed surface winds ( $\text{ms}^{-1}$ ). Rain contours are 1, 5, 10 and 25 mm, speed contours are  $5 \text{ ms}^{-1}$  and one barb is  $10 \text{ ms}^{-1}$ . Observed surface front is depicted using traditional frontal symbols and model-simulated front is shown with heavy dashed line.
- Figure 13 Model-simulated fields at 21 h (0900 UTC 19 September 1983) on the 4-km domain in Exp. WS3GR, (a) 3-h total precipitation (mm), (b) Surface-layer wind overlaid with observed surface winds ( $\text{ms}^{-1}$ ). Rain contours are 1, 5, 10 and 25 mm, speed contours are  $5 \text{ ms}^{-1}$  and one barb is  $10 \text{ ms}^{-1}$ . Observed surface front is depicted using traditional frontal symbols and model-simulated front is shown with heavy dashed line.
- Figure 14 MM5- and WRF-simulated PBL height (m) along the northwest-southeast cross section shown in Fig. 3 for all experiments on the 4-km resolution domain at 21 h (0900 UTC 19 September 1983). The cross-section mean PBL height values are

plotted on the right side of the chart with the digital values also included above the experiment key at the bottom of the figure.

- Figure 15 Model-simulated fields at 30 h (1800 UTC 19 September 1983) on the 4-km domain in Exp. MS11. (a) 3-h total precipitation (mm), (b) Surface-layer wind overlaid with observed surface winds ( $\text{ms}^{-1}$ ), and (c) Surface-layer temperature overlaid with observed surface temperature (C). Rain contours are 1, 5, 10 and 25 mm, speed contours are  $5 \text{ ms}^{-1}$  and one barb is  $10 \text{ ms}^{-1}$ , and temperature contours are 1 C. Heavy dashed lines are used to illustrate wind-shift lines likely associated with convective outflow boundaries and precipitation-induced cold pools. A red L and temperature value (C) is used to denote a surface cold pool (i.e., a surface-layer temperature minimum located within or near a model-precipitation region).
- Figure 16 Model-simulated fields at 30 h (1800 UTC 19 September 1983) on the 4-km domain in Exp. MS11KF. (a) 3-h total precipitation (mm), (b) Surface-layer wind overlaid with observed surface winds ( $\text{ms}^{-1}$ ), and (c) Surface-layer temperature overlaid with observed surface temperature (C). Rain contours are 1, 5, 10 and 25 mm, speed contours are  $5 \text{ ms}^{-1}$  and one barb is  $10 \text{ ms}^{-1}$ , and temperature contours are 1 C. Heavy dashed lines are used to illustrate wind-shift lines likely associated with convective outflow boundaries and precipitation-induced cold pools. A red L and temperature value (C) is used to denote a surface cold pool (i.e., a surface-layer temperature minimum located within or near a model-precipitation region).
- Figure 17 Model-simulated fields at 30 h (1800 UTC 19 September 1983) on the 4-km domain in Exp. MS12. (a) 3-h total precipitation (mm), (b) Surface-layer wind overlaid with observed surface winds ( $\text{ms}^{-1}$ ), and (c) Surface-layer temperature overlaid with observed surface temperature (C). Rain contours are 1, 5, 10 and 25 mm, speed contours are  $5 \text{ ms}^{-1}$  and one barb is  $10 \text{ ms}^{-1}$ , and temperature contours are 1 C. Heavy dashed lines are used to illustrate wind-shift lines likely associated with convective outflow boundaries and precipitation-induced cold pools. A red L and temperature value (C) is used to denote a surface cold pool (i.e., a surface-layer temperature minimum located within or near a model-precipitation region).
- Figure 18 Model-simulated fields at 30 h (1800 UTC 19 September 1983) on the 4-km domain in Exp. WB2. (a) 3-h total precipitation (mm), (b) Surface-layer wind overlaid with observed surface winds ( $\text{ms}^{-1}$ ), and (c) Surface-layer temperature overlaid with observed surface temperature (C). Rain contours are 1, 5, 10 and 25 mm, speed contours are  $5 \text{ ms}^{-1}$  and one barb is  $10 \text{ ms}^{-1}$ , and temperature contours are 1 C. Heavy dashed lines are used to illustrate wind-shift lines likely associated with convective outflow boundaries and precipitation-induced cold pools. A red L and temperature value (C) is used to denote a surface cold pool (i.e., a surface-layer temperature minimum located within or near a model-precipitation region).



- Figure 19 Model-simulated fields at 30 h (1800 UTC 19 September 1983) on the 4-km domain in Exp. MS12KF. (a) 3-h total precipitation (mm), (b) Surface-layer wind overlaid with observed surface winds ( $\text{ms}^{-1}$ ), and (c) Surface-layer temperature overlaid with observed surface temperature (C). Rain contours are 1, 5, 10 and 25 mm, speed contours are  $5 \text{ ms}^{-1}$  and one barb is  $10 \text{ ms}^{-1}$ , and temperature contours are 1 C. Heavy dashed lines are used to illustrate wind-shift lines likely associated with convective outflow boundaries and precipitation-induced cold pools. A red L and temperature value (C) is used to denote a surface cold pool (i.e., a surface-layer temperature minimum located within or near a model-precipitation region).
- Figure 20 Model-simulated fields at 30 h (1800 UTC 19 September 1983) on the 4-km domain in Exp. WB2KF. (a) 3-h total precipitation (mm), (b) Surface-layer wind overlaid with observed surface winds ( $\text{ms}^{-1}$ ), and (c) Surface-layer temperature overlaid with observed surface temperature (C). Rain contours are 1, 5, 10 and 25 mm, speed contours are  $5 \text{ ms}^{-1}$  and one barb is  $10 \text{ ms}^{-1}$ , and temperature contours are 1 C. Heavy dashed lines are used to illustrate wind-shift lines likely associated with convective outflow boundaries and precipitation-induced cold pools. A red L and temperature value (C) is used to denote a surface cold pool (i.e., a surface-layer temperature minimum located within or near a model-precipitation region).
- Figure 21 Model-simulated fields at 30 h (1800 UTC 19 September 1983) on the 4-km domain in Exp. WS2. (a) 3-h total precipitation (mm), (b) Surface-layer wind overlaid with observed surface winds ( $\text{ms}^{-1}$ ), and (c) Surface-layer temperature overlaid with observed surface temperature (C). Rain contours are 1, 5, 10 and 25 mm, speed contours are  $5 \text{ ms}^{-1}$  and one barb is  $10 \text{ ms}^{-1}$ , and temperature contours are 1 C. Heavy dashed lines are used to illustrate wind-shift lines likely associated with convective outflow boundaries and precipitation-induced cold pools. A red L and temperature value (C) is used to denote a surface cold pool (i.e., a surface-layer temperature minimum located within or near a model-precipitation region).
- Figure 22 Model-simulated fields at 30 h (1800 UTC 19 September 1983) on the 4-km domain in Exp. WS2KF. (a) 3-h total precipitation (mm), (b) Surface-layer wind overlaid with observed surface winds ( $\text{ms}^{-1}$ ), and (c) Surface-layer temperature overlaid with observed surface temperature (C). Rain contours are 1, 5, 10 and 25 mm, speed contours are  $5 \text{ ms}^{-1}$  and one barb is  $10 \text{ ms}^{-1}$ , and temperature contours are 1 C. Heavy dashed lines are used to illustrate wind-shift lines likely associated with convective outflow boundaries and precipitation-induced cold pools. A red L and temperature value (C) is used to denote a surface cold pool (i.e., a surface-layer temperature minimum located within or near a model-precipitation region).

- Figure 23 Model-simulated fields at 30 h (1800 UTC 19 September 1983) on the 4-km domain in Exp. WS3. (a) 3-h total precipitation (mm), (b) Surface-layer wind overlaid with observed surface winds ( $\text{ms}^{-1}$ ), and (c) Surface-layer temperature overlaid with observed surface temperature (C). Rain contours are 1, 5, 10 and 25 mm, speed contours are  $5 \text{ ms}^{-1}$  and one barb is  $10 \text{ ms}^{-1}$ , and temperature contours are 1 C. Heavy dashed lines are used to illustrate wind-shift lines likely associated with convective outflow boundaries and precipitation-induced cold pools. A red L and temperature value (C) is used to denote a surface cold pool (i.e., a surface-layer temperature minimum located within or near a model-precipitation region).
- Figure 24 Model-simulated fields at 30 h (1800 UTC 19 September 1983) on the 4-km domain in Exp. WS3GR. (a) 3-h total precipitation (mm), (b) Surface-layer wind overlaid with observed surface winds ( $\text{ms}^{-1}$ ), and (c) Surface-layer temperature overlaid with observed surface temperature (C). Rain contours are 1, 5, 10 and 25 mm, speed contours are  $5 \text{ ms}^{-1}$  and one barb is  $10 \text{ ms}^{-1}$ , and temperature contours are 1 C. Heavy dashed lines are used to illustrate wind-shift lines likely associated with convective outflow boundaries and precipitation-induced cold pools. A red L and temperature value (C) is used to denote a surface cold pool (i.e., a surface-layer temperature minimum located within or near a model-precipitation region).
- Figure 25 MM5- and WRF-simulated PBL height (m) along the northwest-southeast cross section shown in Fig. 3 for all experiments on the 4-km resolution domain at 30 h (1800 UTC 19 September 1983). The cross-section mean PBL height values are plotted on the right side of the chart with the digital values also included above the experiment key at the bottom of the figure.
- Figure 26 Model-simulated surface-layer wind speed statistics ( $\text{ms}^{-1}$ ) on the 4-km domain from 1200 UTC 18 September – 1800 UTC 19 September 1983 for all experiments. a) mean absolute error (MAE), and b) mean error (ME). The 30-hour mean statistics are plotted on the right side of the chart with the digital values also included above the experiment key at the bottom of the figure.
- Figure 27 Model-simulated vertical profile wind speed statistics ( $\text{ms}^{-1}$ ) on the 4-km domain from 1200 UTC 18 September – 1800 UTC 19 September 1983 for all experiments. a) mean absolute error (MAE), and b) mean error (ME). The 32-layer mean statistics are plotted on the top of the chart with the digital values also included above the experiment key at the bottom of the figure.
- Figure 28 Model-simulated index of agreement (fraction) on the 4-km domain for wind speed for all experiments, a) Surface-layer value from 1200 UTC 18 September – 1800 UTC 19 September 1983 for all experiments, b) vertical profile of the 30-h averaged value. The mean statistics are plotted at the top of the chart with the digital values also included above the experiment key at the bottom of the figure.

- Figure 29 Model-simulated surface-layer wind direction statistics (deg) on the 4-km domain from 1200 UTC 18 September – 1800 UTC 19 September 1983 for all experiments. a) mean absolute error (MAE), and b) mean error (ME) . The 30-hour mean statistics are plotted on the right side of the chart with the digital values also included above the experiment key at the bottom of the figure.
- Figure 30 Model-simulated vertical profile wind direction statistics (deg) on the 4-km domain from 1200 UTC 18 September – 1800 UTC 19 September 1983 for all experiments. a) mean absolute error (MAE), and b) mean error (ME). The 32-layer mean statistics are plotted on the top of the chart with the digital values also included above the experiment key at the bottom of the figure.
- Figure 31 Model-simulated vector wind difference ( $\text{ms}^{-1}$ ) on the 4-km domain for all experiments, a) Surface-layer value from 1200 UTC 18 September – 1800 UTC 19 September 1983 for all experiments, b) vertical profile of the 30-h averaged value. The mean statistics are plotted at the top of the chart with the digital values also included above the experiment key at the bottom of the figure.
- Figure 32 Model-simulated surface-layer temperature statistics (C) on the 4-km domain from 1200 UTC 18 September – 1800 UTC 19 September 1983 for all experiments. a) mean absolute error (MAE), and b) mean error (ME) . The 30-hour mean statistics are plotted on the right side of the chart with the digital values also included above the experiment key at the bottom of the figure.
- Figure 33 Model-simulated vertical profile temperature statistics (C) on the 4-km domain from 1200 UTC 18 September – 1800 UTC 19 September 1983 for all experiments. a) mean absolute error (MAE), and b) mean error (ME). The 32-layer mean statistics are plotted on the top of the chart with the digital values also included above the experiment key at the bottom of the figure.
- Figure 34 Model-simulated surface-layer vapor mixing ratio statistics ( $\text{g kg}^{-1}$ ) on the 4-km domain from 1200 UTC 18 September – 1800 UTC 19 September 1983 for all experiments. a) mean absolute error (MAE), and b) mean error (ME) . The 30-hour mean statistics are plotted on the right side of the chart with the digital values also included above the experiment key at the bottom of the figure.
- Figure 35 Model-simulated vertical profile vapor mixing ratio statistics ( $\text{g kg}^{-1}$ ) on the 4-km domain from 1200 UTC 18 September – 1800 UTC 19 September 1983 for all experiments. a) mean absolute error (MAE), and b) mean error (ME). The 32-layer mean statistics are plotted on the top of the chart with the digital values also included above the experiment key at the bottom of the figure.
- Figure 36 Model-simulated sea-level pressure statistics (mb) on the 4-km domain from 1200 UTC 18 September – 1800 UTC 19 September 1983 for all experiments. a) mean absolute error (MAE), and b) mean error (ME) . The 30-hour mean statistics are plotted on the right side of the chart with the digital values also included above the experiment key at the bottom of the figure.

- Figure 37      Maximum model-simulated precipitation amounts (mm) on the 4-km domain for all experiments with and without convective parameterization scheme (CPS), for the three-hour periods ending at 21 hours (0900 UTC 19 September 1983), and 30 hours (1800 UTC 19 September 1983), and the maximum total accumulated precipitation through the entire 30-hour period. These maximum values are computed from the sum of the parameterized subgrid precipitation (if a CPS is used) and the grid-resolved (explicit) precipitation for each model experiment.
- Figure 38      Model-simulated mean absolute error (MAE) for the surface layer averaged over the period 1200 UTC 18 September – 1800 UTC 19 September 1983, for all experiments both with and without convective parameterization scheme (CPS). a) wind speed ( $\text{ms}^{-1}$ ), b) wind direction (deg), c) temperature (C), d) vapor mixing ratio ( $\text{g kg}^{-1}$ ) and e) sea-level pressure (mb).
- Figure 39      Model-simulated mean absolute error (MAE) averaged over all layers over the period 1200 UTC 18 September – 1800 UTC 19 September 1983, for all experiments, both with and without convective parameterization scheme (CPS). a) wind speed ( $\text{ms}^{-1}$ ), b) wind direction (deg), c) temperature (C) and d) vapor mixing ratio ( $\text{g kg}^{-1}$ ).

## 1. INTRODUCTION

### 1.1 *Background*

A previous CRC-funded inter-regional transport study (A-28) was conducted by Seaman et al. (2002) and Deng et al. (2004) using the Penn State/NCAR MM5 based on the 18-19 September 1983 Cross Appalachian Tracer Experiment (CAPTEX) case. It was found that use of FDDA, along with 12-km resolution and improved physics, produced the overall best performance. However, further reduction of the grid length from 12 km to 4 km had detrimental effects on the meteorological and plume dispersion solutions. The primary cause of the poor mesoscale model performance was likely due to the explicit (grid-resolved) representation of convection accompanying a cold front advancing across the lower Great Lakes and into New England. Because no convective parameterization scheme (CPS) was used on the 4-km grid, the convective updrafts were forced on coarser-than-realistic scales (normal updraft diameter for most storms in the eastern United States is  $\sim 2$  km), and the rainfall and the atmospheric response to the convection were too strong. The evaporative cooling and the associated downdrafts from these grid-point storms were too vigorous causing widespread disruption of the low-level winds and spurious advection of the simulated tracer.

To solve this “grid-point storm” problem and improve the MM5 model simulations on the 4-km grid, Phase 1 of CRC project A-46 has focused on a series of experiments to address model sensitivities on the 4-km resolution domain to use of Analysis FDDA versus Obs FDDA, planetary boundary layer (PBL) turbulence, mixed-phase microphysics, CPS and enhanced horizontal diffusion (Stauffer and Deng 2004, Deng and Stauffer 2005). Since there are no CPSs suitable for the 4-km scale at present, various MM5 sensitivity experiments were designed to

find a best approach to improve the 4-km model simulations. Possible approaches include use of data assimilation (important for retrospective air quality studies), use of improved PBL physics, microphysics, use of an existing CPS on the 4-km resolution and numerical diffusion.

It was found in Stauffer and Deng (2004) and Deng and Stauffer (2005) that enhanced vertical mixing in the GS PBL scheme showed marked improvements in the simulated wind and mass fields. However, it was apparent that using the enhanced vertical mixing alone did not alleviate the problem with excessive grid-point precipitation on the 4-km resolution domain.

It was also found that when the MRF PBL scheme was applied in lieu of the GS PBL scheme, MM5 produced a significantly worse model-simulated precipitation field because the spurious convection had spread to a much larger area, associated with an even larger area of disturbed flow with outflow boundaries and cold pools. Statistical evaluation confirmed that the MM5 experiment using the MRF PBL scheme produced degraded model simulations in all fields including wind speed, wind direction and temperature. The only improvement (mainly during night time) was in the water vapor mixing ratio field and was likely caused by the overestimation of the PBL depth.

Use of mixed-phase microphysics (Reisner et al. 1998) produced a precipitation pattern that showed enhanced and more localized precipitation, and sometimes stronger grid-point storms. Experiments using enhanced horizontal diffusion suggested that use of larger horizontal diffusion alone as a solution to this grid-point storm problem was largely ineffective and could also smooth out realistic mesoscale wind structure produced by the model.

When a CPS was applied directly to the 4-km grid, the model-simulated non-convective rain produced by the explicit microphysics was significantly reduced. The convective scheme produced light or no precipitation in northwest PA (at 30 h) where grid-point type storms and a

mesoscale convective system (MCS) had developed in all of the other experiments. Statistical score comparisons with the baseline experiment, MB2, indicated that use of Kain-Fritsch (KF) convective scheme on the 4-km resolution domain had produced some improvements for the model-simulated fields of wind speed, wind direction, temperature and mixing ratio.

Combining Obs FDDA with KF or Grell CPS produced the best overall results in both the subjective and statistical evaluations, with Obs FDDA and KF somewhat better. These experiments did not produce the spurious MCS at 30 h which allowed the simulated low-level flow at this time to be more consistent with the observations. Thus, use of the combination of Obs FDDA and a CPS on the 4-km resolution domain seemed to have the most significant positive impact on the model solutions in this CAPTEX-83 case, with the best overall results obtained using Obs FDDA and KF.

However, finer model resolution does not always produce better simulations, especially for convectively unstable environments. Use of a CPS and Obs FDDA on the 4-km resolution domain produced results more comparable to those using CPS and Obs FDDA on a 12-km resolution domain, and this represented a further improvement to the best MM5 simulation using Analysis FDDA on the 12-km resolution domain reported in Deng et al. (2004).

Since the WRF model (Wicker and Skamarock 2002, Klemp et al. 2003) is a new state-of-the-science meteorological model currently under development and specifically designed for the 1-10 km grid length scales, it is useful to revisit this subject using WRF, because comparison of model performance between MM5 and WRF and lessons learned here can be a significant contribution to developing fine-resolution mesoscale models in the future. The WRF uses an Arakawa-C horizontal grid staggering with higher-order spatial and temporal finite differencing schemes. In addition to updated model physics including PBL physics, microphysics and CPS, it

also contains cloud-scale 3D sub-grid turbulence schemes (Smagorinsky 1965 or TKE-predicting schemes). The WRF should be attractive for future air-quality work due to its mass conservation, improved numerics and expanding physics.

## 1.2 *Objectives*

To further study how to improve 4-km mesoscale model simulations based on lessons learned in the Phase 1 of CRC A-46 project, ten modeling experiments (four MM5 and six WRF) are designed and conducted in Phase 2 of the project. Both subjective and objective evaluations will be performed on the model-simulated fields. Subjective evaluation is again focused on the model-simulated precipitation field and the surface-layer wind field at the two model times: 21 h (09 UTC 19 September 1983) and 30 h (18 UTC 19 September 1983). Objective evaluation will be performed by comparing the MAE and ME error distributions (over time and vertical layers) of the model-simulated wind speed, wind direction, temperature and water vapor mixing ratio for all ten model experiments.

Since there is no FDDA capability available in WRF, all MM5 and WRF experiments conducted in this research do not involve FDDA. Thus, the objectives of this research are to investigate the role of model physics on the accuracy of cloud and precipitation fields, and associated flow fields simulated at  $\Delta x = 4$  km during CAPTEX-83, using both MM5 and WRF. A fair comparison between MM5 and WRF involves four sensitivity experiments (two MM5 and two WRF), with the same initial conditions and lateral boundary conditions and similar physics packages used in each model.

A brief description of the CAPTEX-83 case is given in Section 2. Section 3 of this final report describes the numerical models, MM5 and WRF, and physics options applied to this



study. The experimental design is given in Section 4, and the model results are presented in Section 5. Finally, a summary of the most relevant findings and suggestions for future work is given in Section 6

## **2. OVERVIEW OF THE 18-19 SEPTEMBER 1983 CAPTEX CASE**

The case chosen for experimentation in this study is the 18-19 September episode from the Cross Appalachian Tracer Experiment of 1983 (CAPTEX '83). This is the same case used previously in CRC project A-28 (Seaman et al. 2002, Deng et al. 2004), and Phase 1 of A-46 (Stauffer and Deng 2004, Deng and Stauffer 2005). This case was selected because it was shown by Seaman et al (2002) in their inter-regional transport study that further reduction of the MM5 horizontal grid size to 4 km had detrimental effects on meteorological and plume dispersion solutions in this case. This is likely due to misrepresentation of convection associated with a cold front by the MM5's explicit moist physics. It was shown in Phase 1 of CRC Project A-46 that applying a CPS on the 4-km resolution domain produced improved simulations.

The meteorological conditions for the CAPTEX '83 case (18-19 September 1983) were characterized by a large anticyclone centered over the Mid-Atlantic Coast, with broad southwesterly wind flow over the Midwest and Northeast U.S. To the northwest of the high, warm and cold fronts (associated with a deep 982-mb occluded storm located in central Canada) were approaching the Northeast, but still lay well to the west. The Canadian storm and the pressure gradient in the Midwest ahead of the cold front were rather strong for this early in autumn. Consistent with the strength of the deep baroclinic storm, the frontal system was propagating rapidly through the western Great Lakes at nearly  $15 \text{ m s}^{-1}$ . Meanwhile, ahead of the cold front in southern Michigan (MI), a warm-sector low-level jet (LLJ) at 850 hPa contained wind speeds of  $30 \text{ m s}^{-1}$  at 1200 UTC 18 September 1983 (not shown).

Surface observations over the Midwest and Northeast U.S. indicate that at 1200 UTC on 18 September 1983, there are many thunderstorms close to the warm front from southeastern Wisconsin (WI) to southern MI, with widespread showers throughout the rest of MI. The rain then shifts eastward with the advancing warm front, so that by 1800 UTC, the rain showers are mostly around Lake Ontario before weakening at 0000 UTC 19 September. Later during the night time, by 0600 UTC, thunderstorm activity and showers again become more widespread along the cold frontal boundary and ahead of the warm front. These reinvigorated storms persisted through the night, mostly along the cold front, but weakened toward morning, especially from Lake Erie to Montreal. Satellite imagery at 0830 UTC (not shown) and surface observations at 0900 UTC 19 September (Fig. 1a) confirm that convective clouds existed over the Great Lakes area, although there was no precipitation reported. By 1800 UTC 19 September (Fig. 1b), no frontal showers were observed in the Northeast, although cloudy skies are found further to the north of the cold front. The 24-hour total precipitation distribution over Eastern U.S. on 19 September 1983 (not shown) indicates that insignificant amounts of precipitation ( $< 0.5$  mm) were observed over the Lake Erie region and somewhat larger amounts ( $< 10$  mm) were observed southeast of Lake Ontario. At both 0900 and 1800 UTC the observed surface winds show southwesterly flow through most of Ohio (OH) and Pennsylvania (PA) ( $< 10 \text{ m s}^{-1}$ ).

### 3. MODEL DESCRIPTION

#### 3.1 MM5 Model

The first meteorological model used in this study is the non-hydrostatic Pennsylvania State University/National Center for Atmospheric Research (PSU/NCAR) mesoscale model, known as MM5. The MM5 is a nonhydrostatic, fully compressible three dimensional primitive equation model with a terrain following sigma (non-dimensional pressure) vertical coordinate (Dudhia 1993, Grell et al. 1994), given by

$$\sigma = \frac{p - p_t}{p_s - p_t} \quad (1)$$

where,  $p$  is the pressure,  $p_s$  is the surface pressure, and  $p_t$  is the pressure at the top of the model. All the sigma layers are defined using a time-invariant "background" pressure field, based on a standard atmospheric lapse rate, while a much smaller prognostic pressure perturbation field ( $p' = p'(x, y, \sigma, t)$ ) represents the time-varying 3-D departure from the background. The MM5 also contains prognostic equations for the three wind components ( $u, v, w$ ), temperature ( $T$ ) and water-vapor mixing ratio ( $q_v$ ), each of which are written in flux form. The model uses a split semi-implicit temporal integration scheme to increase computational efficiency. The MM5 is flexible enough to be applied to a wide range of synoptic and mesoscale phenomena, including baroclinic storm development, tropical cyclones, and the role of physical processes, such as convection and planetary boundary layer (PBL) influences. For a more complete description of the MM5 formalism, see Dudhia (1993) and Grell et al. (1994).

The MM5 is a nested grid model with the horizontal grid system of the MM5 domains based on the staggered Arakawa-B grid described by Arakawa and Lamb (1977). In this grid configuration, the wind components,  $u$  and  $v$ , are defined on the so-called "dot points" at the corners of a grid box, while all the other variables are defined on the "cross points" at the center of the boxes. The vertical structure of the model's grid is such that vertical motion,  $w$ , and the  $TKE$  are defined on the full sigma-layer boundaries, while the other variables (e.g.,  $u$ ,  $v$ ,  $T$ , and  $q_v$ ) are defined on the half levels (middle of the layers) (also see Grell et al. 1994).

For this study the nested domains of 108 km, 36 km, 12 km and 4 km are used, as in the original studies by Seaman et al. 2002 and Stauffer and Deng (2004). On all of these domains, resolved-scale moist processes are represented using explicit prognostic equations for cloud water or ice ( $q_c$ ) and rain water or snow ( $q_r$ ) according to a formulation described by Dudhia (1989).

An updated Kain-Fritsch (KF) convective parameterization (Kain and Fritsch 1990, Kain and Fritsch 1993) is used here in both models as described in more detail below. The Kain-Fritsch scheme has a fully entraining/detraining cloud model and uses an energy-equilibrium closure. First, the potential for convective clouds is diagnosed by lifting low-level parcels to their saturation levels. Then, a convection-forming parcel is initiated from the saturated parcel below 700 hPa having the highest  $\theta_e$  (equivalent potential temperature). Rain is triggered when the cloud exceeds a critical depth (3-4 km). Once convection is initiated in a grid column, it continues until all convective available potential energy (CAPE) has been eliminated.

The new version of the Kain Fritsch scheme that has been tested in the National Centers for Environmental Prediction's (NCEP) Eta model (Kain 2004) and used in this study contains a number of modifications to the original scheme. The updraft formulation was changed in several

ways: (1) a minimum entrainment rate (50% of the maximum possible entrainment rate used in the original scheme) is imposed, primarily to suppress convective initiation in marginally buoyant, relatively dry environments, (2) the cloud radius is now specified to vary as a function of subcloud-layer convergence so that it promotes activation in strongly convergent regimes and suppresses deep convection activation in weakly convergent or divergent environments, (3) a minimum cloud depth, required for activation of deep convection (4 km in the original scheme), is allowed to vary as a function of cloud-base temperature so that relatively shallow clouds are allowed, (4) non-precipitating shallow convective clouds are allowed when buoyant updrafts can form but cannot reach the imposed minimum cloud depth for deep convection, with cloud-base mass flux being defined as a function of the turbulent kinetic energy (TKE) in the subcloud layer (Deng et al. 2003), rather than CAPE. The downdraft formulation was also changed.

Downdrafts are formed from air in the layer at 150–200 hPa above cloud base, and they detrain over a fairly deep layer below cloud base. Downdraft mass flux is estimated as a function of the relative humidity and stability just above cloud base but is no longer related to vertical wind shear. Modifications to the closure assumption were made. For the closure assumption, although the scheme is still programmed to eliminate CAPE, the calculation of CAPE is based on the path of an entraining (diluted) parcel rather than one that ascends without dilution.

The Grell CPS is a mass-flux based scheme that contains an entraining/detraining cloud model that involves both updraft and downdraft. Its closure depends on quasi-equilibrium between the large-scale rate of convective destabilization and localized rate of stabilization by (parameterized) convection. The hypothesis that application of these schemes directly on the 4-km domain can reduce the tendency of the explicit moisture scheme to overestimate precipitation

and produce grid point storms is put to the test. These spurious rain areas cause serious disruption of the larger scale wind patterns which largely affect transport and dispersion.

Two different types of planetary boundary layer (PBL: vertical mixing only) turbulence parameterizations are used in the MM5 experiments in this study: the Penn State Gayno-Seaman PBL (GS TKE PBL) (Shafran et al. 2000, Stauffer et al. 1999), and the Eta M-Y PBL scheme. The GSPBL is a 1.5-order closure approach developed by Gayno et al. (1994) and described by Shafran et al. (2000), with additional improvements described by Stauffer et al. (1999). It has a second-order predictive equation for TKE, while the eddy viscosity is a function of the predicted TKE and several stability-dependent mixing lengths. Turbulent fluxes of momentum, moisture and heat are parameterized using K-theory in which the turbulent transfer occurs down gradient. However, since basic K-theory fails under certain convective situations (Moeng and Wyngaard, 1989), countergradient flux terms are included to correct the turbulent transport terms near the surface and near the top of the convective mixed layer (Gayno et al. 1994). The TKE-predicting scheme is representative of newer higher-order PBL physics and has been shown to generate both shear-driven turbulence and in-cloud mixing associated with cloud-top radiative flux divergence (Stauffer et al. 1999). It has also been shown to predict more accurate boundary-layer structure for convectively unstable conditions, compared to the Blackadar scheme (Shafran et al. 2000). In addition, Stauffer et al. (1999) added the capability to account for the effects of saturation on the buoyancy production of TKE, which makes this 1.5-order scheme more accurate in cloudy or foggy conditions than the other turbulence parameterizations available in MM5.

The Eta M-Y PBL scheme is also available in the MM5 modeling system. It was developed by Janjic (1990, 1996, 2002) and it represents a nonsingular implementation of the

Mellor-Yamada Level 2.5 turbulence closure model (Mellor and Yamada, 1982) through the full range of atmospheric turbulent regimes. This scheme is also available in WRF and described in more detail in the following WRF model description section.

For atmospheric radiation, the Rapid Radiative Transfer Model (RRTM) is used for longwave, and the simple Dudhia scheme (Grell et al. 1994) is used for shortwave. The RRTM is based on Mlawer et al. (1997) and is a spectral-band scheme using the correlated-k method. It uses pre-set tables to accurately represent longwave processes due to water vapor, ozone, CO<sub>2</sub>, and trace gases (if present), as well as accounting for cloud optical depth. The Dudhia radiation scheme is based on a two-stream, single-band approach. It is fully interactive with dry air, water vapor and cloud liquid/ice. It has a simple downward integration of solar flux, accounting for clear-air scattering, water vapor absorption (Lacis and Hansen, 1974), and cloud albedo and absorption. It uses look-up tables for clouds from Stephens (1978).

### **3.2 *Weather Research and Forecast (WRF) Model***

The WRF model is a new state-of-the-science meteorological model currently under development and specifically designed for the 1-10 km grid length scales. Currently there are two WRF models available for the research and forecast communities, NCAR advanced research WRF (ARW) and NCEP non-hydrostatic mesoscale model (NMM). The WRF model used in this research is the advanced research WRF (ARW) model developed at NCAR (Skamarock et al. 2005, Klemp et al. 2003, Wicker and Skamarock 2002). The WRF uses an Arakawa-C horizontal grid staggering (u, v and mass each located at different grid locations) with higher-order spatial and temporal finite differencing schemes. In addition to updated model physics including PBL physics, microphysics and CPS, it also contains cloud-scale 3D sub-grid



turbulence schemes (Smagorinsky or TKE-predicting schemes). The WRF should be attractive for future air-quality work due to its mass conservation, improved numerics and expanding physics.

The ARW is a nonhydrostatic, fully compressible three dimensional primitive equation model with a terrain-following hydrostatic pressure vertical coordinate (Skamarock et al. 2005, Laprise 1992), denoted by  $\eta$  and defined as

$$\eta = \frac{p_{dh} - p_{dht}}{\mu_d} \quad (2)$$

$$\mu_d = p_{dhs} - p_{dht} \quad (3)$$

where  $\mu_d$  represent the mass of the dry air in the column,  $p_{dh}$  represents the hydrostatic pressure of the dry atmosphere,  $p_{dhs}$  is the surface pressure of the dry atmosphere, and  $p_{dht}$  is the hydrostatic pressure at the top of the dry atmosphere. Since  $\mu_d$  is the dry mass per unit area within the column in the model domain, the appropriate flux-form variables are defined as

$$\vec{V} = \mu_d \vec{v} = (U, V, W) \quad \vec{\Omega} = \mu_d \dot{\eta} \quad \Theta = \mu_d \theta \quad Q_m = \mu_d q_m \quad (4)$$

where  $\vec{v} = (u, v, w)$  represents the uncoupled wind components,  $\theta$  is the potential temperature, and  $q_m = q_v, q_c, q_i, \dots$  represents the mixing ratios for water vapor, cloud, rain, ice, etc. With the definitions for flux-form variables, the moist Euler equations for the predictive equations for wind, potential temperature, geopotential height, mixing ratios for water species and equation for mass continuity can be written as (Skamarock et al. 2005)

$$\frac{\partial U}{\partial t} + (\nabla \cdot \vec{V}u)_\eta + \mu_d \alpha \frac{\partial p}{\partial x} + \left(\frac{\alpha}{\alpha_d}\right) \frac{\partial p}{\partial \eta} \frac{\partial \phi}{\partial x} = F_U \quad (5)$$

$$\frac{\partial V}{\partial t} + (\nabla \cdot \vec{V}v)_\eta + \mu_d \alpha \frac{\partial p}{\partial y} + \left(\frac{\alpha}{\alpha_d}\right) \frac{\partial p}{\partial \eta} \frac{\partial \phi}{\partial y} = F_V \quad (6)$$

$$\frac{\partial W}{\partial t} + (\nabla \cdot \vec{V}W)_\eta - g\left[\frac{\alpha}{\alpha_d}\frac{\partial p}{\partial \eta} - \mu_d\right] = F_w \quad (7)$$

$$\frac{\partial \Theta}{\partial t} + (\nabla \cdot \vec{V}\Theta)_\eta = F_\Theta \quad (8)$$

$$\frac{\partial \phi}{\partial t} + \frac{1}{\mu_d}[(\vec{V} \cdot \nabla \phi)_\eta - gW] = 0 \quad (9)$$

$$\frac{\partial Q_m}{\partial t} + (\vec{V} \cdot \nabla q_m)_\eta = F_{Q_m} \quad (10)$$

$$\frac{\partial \mu_d}{\partial t} + (\nabla \cdot \vec{V})_\eta = 0 \quad (11)$$

with the diagnostic equation for dry inverse density

$$\frac{\partial \phi}{\partial \eta} = -\alpha_d \mu_d \quad (12)$$

and the diagnostic relation for the full pressure (vapor plus dry air)

$$p = p_0 \left( \frac{R_d \theta_m}{p_0 \alpha_d} \right)^{c_p/c_v} \quad (13)$$

where  $\alpha_d$  is the inverse density of the dry air and

$$\alpha = \alpha_d (1 + q_v + q_c + q_r + q_i + \dots)^{-1} \quad (14)$$

Additionally,

$$\theta_m = \theta \left( 1 + q_v \frac{R_v}{R_d} \right) \approx \theta (1 + 1.61 q_v). \quad (15)$$

In these equations,

$$(\nabla \cdot \vec{V}a)_\eta = \frac{\partial Ua}{\partial x} + \frac{\partial Va}{\partial y} + \frac{\partial \Omega a}{\partial \eta} \quad (16)$$

and

$$(\vec{V} \cdot \nabla a)_\eta = U \frac{\partial a}{\partial x} + V \frac{\partial a}{\partial y} + \Omega \frac{\partial a}{\partial \eta} \quad (17)$$

where  $a$  represents a generic variable. The right-hand-side (RHS) terms  $F_U, F_V, F_W$  and  $F_\Theta$  in equation (5), (6), (7) and (8) represent forcing terms arising from model physics, turbulent mixing, spherical projections, and the earth's rotation.

In order to reduce truncation errors in the horizontal pressure gradient calculations in the discrete solver, and the machine rounding errors in the vertical pressure gradient and buoyancy calculations, perturbation variables are used in the above governing equations. For this purpose, a variable is divided into two parts: a perturbation from a hydrostatically balanced reference state, and a reference state value in hydrostatic balance and a function of height only, that is

$$p = \bar{p}(x, y, \eta) + p'; \phi = \bar{\phi}(x, y, \eta) + \phi'; \alpha = \bar{\alpha}(x, y, \eta) + \alpha'; \mu_d = \bar{\mu}_d(x, y) + \mu'_d \quad (18)$$

Thus, the hydrostatically balanced portion of the pressure gradients in the reference sounding can be removed without approximation to the equations using these perturbation variables. The detailed list of perturbation equations can be found in Skamarock et al. (2005).

For temporal discretization, the ARW solver uses a time-split integration scheme. Slow or low-frequency modes are integrated using a third-order Runge-Kutta (RK3) time integration scheme, while the high-frequency acoustic modes are integrated over smaller time steps to maintain numerical stability (Wicker and Skamarock 2002). For spatial discretization, ARW solver uses Arakawa-C horizontal grid staggering, in which normal velocities are staggered one-half grid length from the thermodynamic variables. The mass point is defined at the grid box center, while wind points are defined at the middle point of on each edge of the same grid box. In the vertical direction, mass fields and horizontal wind components are defined at model half  $\eta$  layers (identical to that in MM5), while the vertical velocity is defined at the full layers.

A number of formulations for turbulent mixing and filtering are available in the ARW solver. Some of them are used for numerical reasons, and other filters are meant to represent

physical sub-grid turbulence processes. Unlike MM5, the ARW allows sub-grid scale turbulence to be parameterized as it is treated in cloud-scale models - including horizontal mixing.

However, when a PBL parameterization is used, all other cloud-scale vertical mixing is disabled, and vertical mixing is parameterized in the chosen PBL scheme.

Like MM5, ARW has a variety of physics options for PBL physics, microphysics, atmospheric radiation and cumulus parameterization. For microphysics, this research uses the Single-Moment 3-class (WSM3) scheme, developed by Hong et al. (1998, 2004). In this scheme a diagnostic relation is used for ice number concentration that is based on ice mass content rather than temperature. Three categories of hydrometers are included: vapor, cloud water/ice, and rain/snow. As with Dudhia (1989), this is a so-called simple-ice scheme wherein the cloud ice and cloud water are counted as the same category. They are distinguished by temperature: namely, cloud ice can only exist when the temperature is less than or equal to the freezing point; otherwise, cloud water can exist. The same condition is applied to rain and snow. Although the ice phase is included, it is considered efficient enough for use in operational models.

For cumulus parameterization, both KF CPS and Grell CPS are used. The KF CPS used in WRF is a modified version of the Kain-Fritsch scheme (KF-Eta) that is based on Kain and Fritsch (1990) and Kain and Fritsch (1993), but has been modified based on testing within the Eta model. As with the original KF scheme, it utilizes a simple cloud model with moist updrafts and downdrafts, including the effects of detrainment, entrainment, and relatively simple microphysics. It differs from the original KF scheme in the following ways: 1) A minimum entrainment rate is imposed to suppress widespread convection in marginally unstable, relatively dry environments; 2) Shallow (non precipitating) convection is allowed for any updraft that does not reach minimum cloud depth for precipitating clouds; this minimum depth varies as a function

of cloud-base temperature; 3) The entrainment rate is allowed to vary as a function of low-level convergence; 4) Downdraft parameterization has changed such that source layer is the entire 150 – 200 hPa deep layer just above cloud base, and that mass flux is specified as a fraction of updraft mass flux at cloud base (fraction is a function of source layer RH rather than wind shear or other parameters, i.e., old precipitation efficiency relationship not used), and that detrainment is specified to occur in updraft source layer and below.

The Grell CPS used in WRF in this research is based on Grell and Devenyi (2002). It introduced an ensemble cumulus scheme in which effectively multiple cumulus schemes and variants are run within each grid box and then the results are averaged to give the feedback to the model. In principle, the averaging can be weighted to optimize the scheme, but the default is an equal weight. The schemes are all mass-flux type schemes, but with differing updraft and downdraft entrainment and detrainment parameters, and precipitation efficiencies. These differences in static control are combined with differences in dynamic control, which is the method of determining cloud mass flux. The dynamic control closures are based on convective available potential energy (CAPE or cloud work function), low-level vertical velocity, or moisture convergence. Those based on CAPE either balance the rate of change of CAPE or relax the CAPE to a climatological value, or remove the CAPE in a convective time scale. The moisture convergence closure balances the cloud rainfall to the integrated vertical advection of moisture. Another control is the trigger, where the maximum cap strength that permits convection can be varied. These controls typically provide ensembles of 144 members.

In WRF the surface layer schemes calculate friction velocities and exchange coefficients that enable the calculation of surface heat and moisture fluxes by the land-surface models and surface stress in the planetary boundary layer scheme. Over water surfaces, the surface fluxes

and surface diagnostic fields are computed in the surface layer scheme itself. The schemes provide no tendencies, only the stability-dependent information about the surface layer for the land-surface and PBL schemes.

Unlike MM5, the surface layer physics is treated outside of a PBL scheme although each surface layer option is tied to particular boundary-layer options. Currently, there are two surface-layer physics options. The first surface-layer option is called Monin-Obukhov scheme. This scheme uses stability functions from Paulson (1970), Dyer and Hicks (1970), and Webb (1970) to compute surface exchange coefficients for heat, moisture, and momentum. A convective velocity following Beljaars (1994) is used to enhance surface fluxes of heat and moisture. No thermal roughness length parameterization is included in the current version of this scheme. A Charnock relation relates roughness length to friction velocity over water. There are four stability regimes following Zhang and Anthes (1982). This surface-layer scheme must be run in conjunction with the MRF or YSU PBL schemes.

The second surface layer option is called Monin-Obukhov-Janjic-Eta scheme, which was developed by Janjic (1996, 2002) and is based on similarity theory (Monin and Obukhov, 1954). The scheme includes parameterizations of a viscous sub-layer. Over water surfaces, the viscous sub-layer is parameterized explicitly following Janjic (1994). Over land, the effects of the viscous sub-layer are taken into account through variable roughness height for temperature and humidity as proposed by Zilitinkevich (1995). The Beljaars (1994) correction is applied in order to avoid singularities in the case of an unstable surface layer and vanishing wind speed. The surface fluxes are computed by an iterative method. This surface layer scheme must be run in conjunction with the Eta (Mellor-Yamada-Janjic) PBL scheme, and is therefore sometimes referred to as the MYJ surface scheme.

No land-surface models are used in this research. However, two PBL physics options have been used: Mellor-Yamada-Janjic PBL (also called M-Y-J Eta TKE PBL) and Yonsei University (YSU) PBL. The M-Y-J Eta TKE PBL scheme (Janjic 1990, 1996, 2002) represents a nonsingular implementation of the Mellor-Yamada Level 2.5 turbulence closure model (Mellor and Yamada, 1982) through the full range of atmospheric turbulent regimes. In this implementation, an upper limit is imposed on the master length scale. This upper limit depends on the TKE as well as the buoyancy and shear of the driving flow. In the unstable range, the functional form of the upper limit is derived from the requirement that the TKE production be nonsingular in the case of growing turbulence. In the stable range, the upper limit is derived from the requirement that the ratio of the variance of the vertical velocity deviation and TKE cannot be smaller than that corresponding to the regime of vanishing turbulence.

The Yonsei University PBL is the next generation of the MRF PBL (Hong and Pan, 1996), also using the countergradient terms to represent fluxes due to non-local gradients. This adds to the MRF PBL an explicit treatment of the entrainment layer at the PBL top. The entrainment is made proportional to the surface buoyancy flux in line with results from studies with large-eddy models. The PBL top is defined using a critical bulk Richardson number of zero (compared to 0.5 in the MRF PBL), so is effectively only dependent on the buoyancy profile which, in general, lowers the calculated PBL top compared to MRF.

For atmospheric radiation used in this research, we use the exact same physics packages as in MM5: RRTM for longwave and Dudhia shortwave. The RRTM is based on Mlawer et al. (1997) and is a spectral-band scheme using the correlated-k method. It uses pre-set tables to accurately represent longwave processes due to water vapor, ozone, CO<sub>2</sub>, and trace gases (if present), as well as accounting for cloud optical depth. The Dudhia radiation scheme is based on

a two-stream, single-band approach. It is fully interactive with dry air, water vapor and cloud liquid/ice. It has a simple downward integration of solar flux, accounting for clear-air scattering, water vapor absorption (Lacis and Hansen, 1974), and cloud albedo and absorption. It uses look-up tables for clouds from Stephens (1978).



## 4. EXPERIMENTAL DESIGN

### 4.1 *MM5 and WRF Model Domains*

For this study the grid configuration is identical to what was used in the Phase 1 study and contains 108, 36, 12 and 4-km domains (Figure 2). The coarsest domain has a resolution of 108 km and covers most of North America with a mesh of 55 X 69 points. The second domain covers the continental United States (CONUS), southern Canada and northern Mexico at 36-km resolution with a mesh of 103 X 151 points. The third domain has a resolution of 12 km and covers the eastern U.S. and parts of southeastern Canada with a mesh of 190 X 208 points. The fourth domain has a resolution of 4 km and is embedded over the Northeast U.S. Inspection of Figure 2 indicates that the area of this 4-km domain covers the entire monitoring network of CAPTEX '83. The 4-km grid has 289 X 316 points, covering an area of 1152 X 1220 km.

The terrain field for the 4-km domain is shown in Figure 3, which shows very detailed mountainous terrain over northeastern U.S. While still not capturing the full height of the actual peaks, it appears that 4-km resolution can adequately represent the height of the main ridges. Thus, the blocking effects of the terrain should be represented well.

Model configuration in the vertical is summarized in Table 1. All four of the domains have 32 layers in the vertical direction. The lowest layer is located at ~29 m AGL. The thickness of the layers increases gradually with height, with 16 layers below 850 m (~1560 m AGL). The top of the model was set at 100 hPa (~ 14 km AGL).

## **4.2      *Initialization and Lateral Boundary Conditions***

The same initial and lateral boundary conditions that were used in the previous studies (Seaman et al. 2002, Deng et al. 2004, Stauffer and Deng 2004, and Deng and Stauffer 2005) are used here. Generation of initial and lateral boundary conditions began with the NCEP 2.5-degree global spectral analyses. The  $1^{\circ} \times 1^{\circ}$  global model fields of temperature, horizontal wind components and relative humidity were accessed at mandatory and supplemental pressure levels (1000, 975, 950, 925, 900, 875, 850, 800, 750, 700, 650, 600, 550, 500, 400, 300, 250, 200, 150, 100 hPa), plus sea-level pressure and ground temperature, and were projected onto the outermost MM5 domains to be used as background (first-guess) fields prior to an objective analysis. Next, in the objective-analysis step, the analyses are enhanced by incorporating standard radiosonde and surface data through use of an anisotropic successive-correction objective analysis (Benjamin and Seaman 1985). The completed pressure-level analyses then are interpolated to the model's sigma levels to be used as initial conditions. For the nested grids, the 108-km analyses also are interpolated to provide initial conditions for the successive nested domains (i.e., 36-km fields are interpolated from the 108-km domain, 12-km fields from the 36-km domain, and 4-km fields from the 12-km domain). To create the WRF initial conditions, software was developed (with help from NCAR) to convert the MM5-formatted initial condition file that was used in Phase 1 of this project to a WRF-formatted initial condition file.

The lateral boundary conditions of the 108-km domains are defined at 12-h intervals from analyses generated in a way similar to that used for the initial conditions. The pressure-level analyses were created at 12-h intervals, while surface fields were generated at 3-h intervals. For the nested grids, the 36-km domain received its lateral boundary conditions directly from the 108-km domain at every time step, since these two domains are run at the same time two-way

interactively. However, the one-way lateral boundary conditions of the 12 and 4-km domain are created by interpolation from the next coarser grid at one-hour intervals.

### **4.3    *Model Experiments***

There are eleven experiments (including a preliminary WRF experiment) conducted in this research involving MM5 and WRF simulations at 4-km resolution. Since WRF currently does not have FDDA capability, all (MM5 and WRF) experiments conducted in this study do not use FDDA on all four domains. For atmospheric radiation, all experiments use Dudhia scheme for short wave and RRTM scheme for long wave. The detailed experimental design is summarized in Table 2 and briefly described below (Note that an experiment name starting with “M” represents a MM5 experiment and an experiment name starting with “W” represents a WRF experiment):

#### **4.3.1    *Experiment WB1***

Similar to the baseline MM5 conducted in Phase 1 of this project, a preliminary baseline WRF experiment was designed. In this first baseline experiment Exp. WB1, the advanced research WRF core (ARW or Eulerian mass) V2.0.2 is used mainly to test the supporting frontend (model input) and backend (model output) processor development work for this project. New software had to be written to convert suitable versions of the MM5 initial conditions and lateral boundary conditions (pressure-level and surface-layer fields) to the WRF vertical coordinate layers and C-grid, and also to convert the WRF output fields on its native model grid and NETCDF format into an MM5-type format that could be read and processed by our verification software. The WRF model output fields were interpolated to the MM5 horizontal B-

grid and vertical grid structures for direct comparison and verification. WRF time steps are set to be 600, 180, 60, 20 seconds for 108-km, 36-km, 12-km and 4-km domains, respectively. This preliminary WRF version WB1 with its bugs and issues was used to report progress in the first quarter and was later replaced several times as updated versions with bug fixes became available (see WB2 below). The following physics options were used on all domains, except that no cumulus parameterization (CPS) is applied on the 4-km domain:

- 1) WSM 3-class simple ice scheme for microphysics,
- 2) RRTM longwave radiation,
- 3) Dudhia shortwave radiation,
- 4) Monin-Obukhov (Janjic Eta) scheme for surface layer option,
- 5) Thermal diffusion scheme for land-surface option,
- 6) Mellor-Yamada-Janjic (Eta) TKE scheme for PBL physics.

#### 4.3.2 *Experiments MS11 and MS11KF*

Since WRF currently does not have a nudging FDDA capability, new MM5 experiments without use of FDDA had to be conducted so that the model simulations between WRF and MM5 can be fairly compared. We also wanted to verify that the grid-point storm problem can be reproduced in MM5 without using FDDA. Thus, the first set of MM5 experiments include Exps. MS11 and MS11KF which are identical to MB2 in Phase 1 of the project, except that FDDA is turned off for all four domains. Exp. MS11 uses GS TKE PBL scheme for PBL physics, simple ice for microphysics, no CPS on the 4-km grid but KF CPS applied on outer domains. Exp. MS11KF is identical to MS11 except that the KF CPS is also applied on the 4-km grid. Comparison between Exp. MS11 and MS11KF indicates the effects of using a CPS on the 4-km

grid when no FDDA is applied, which was found to be one of the major factors that contribute to the improvements of the MM5 simulations in the first phase of the project (see Exp. MS5 in Phase 1).

#### 4.3.3 *Experiments MS12 and WB2*

This set of MM5 and WRF experiments (Exps. MS12 and WB2) are designed so that both models use comparable physics, so the MM5 and WRF simulations can be fairly compared. Exp. MS12 uses Eta M-Y PBL scheme instead of the Penn State GS PBL, simple ice microphysics and no CPS on the 4-km domain, but KF CPS applied on the outer domains. Exp. WB2 uses M-Y-J Eta TKE PBL scheme (which is comparable to the Eta M-Y PBL scheme that is available in MM5), WSM 3-class simple ice microphysics scheme (similar to the MM5 simple-ice microphysics scheme), no CPS on the 4-km domain but KF CPS applied on the outer domains.

#### 4.3.4 *Experiments MS12KF and WB2KF*

It was found in Phase 1 of this project (Stauffer and Deng 2004, Deng and Stauffer 2005) that when a CPS was applied directly to the 4-km grid, the MM5-simulated non-convective rain produced by the explicit microphysics was significantly reduced. For example, The convective scheme in MM5 produced light or no precipitation in northwest PA (at 30 h) where grid-point type storms and a MCS had developed in all of the other experiments. Statistical score comparisons indicated that use of KF on the 4-km resolution domain had produced some improvements for the MM5-simulated fields of wind speed, wind direction, temperature and mixing ratio. Thus in this second phase of this research we revisit this issue in the MM5 without

FDDA on any of the domains and in WRF under the same conditions, and compare the WRF results to those produced in MM5.

Exp. MS12KF is identical to MS12 except that KF CPS is applied on the 4-km domain, and Exp. WB2KF is identical to WB2 except that KF CPS is applied on the 4-km domain. Therefore, Exps. MS12KF and WB2KF are also comparable experiments because both MM5 and WRF use similar physics packages. Comparison between Exp. MS12 and MS12KF, and WB2 and WB2KF indicates the effects of using a CPS on the 4-km grid.

#### 4.3.5 *Experiments WS2 and WS2KF*

It has been shown in Phase 1 of this project that the MM5 simulation is sensitive to the use of PBL physics. When the MRF PBL scheme was applied in lieu of the GS PBL scheme in Phase 1 Exp. MS3, MM5 produced a significantly worse simulation in the model-simulated precipitation field because the spurious convection had spread to a much larger area, associated with an even larger area of disturbed flow with outflow boundaries and cold pools. Statistical evaluation indicated that use of MRF PBL produced degraded model simulations in all fields including wind speed, wind direction and temperature. The only improvement (mainly during night time) was in the water vapor mixing ratio field and was likely caused by the overestimation of the PBL depth.

Since the YSU PBL scheme in WRF is an updated version of the MRF PBL scheme in MM5, it is the purpose of this set of experiments to investigate the performance of the YSU PBL scheme in WRF for grid-point storm issues. Exp. WS2 is identical to Exp. WB2 except that it uses the YSU PBL scheme in lieu of M-Y-J Eta PBL scheme. No CPS is applied on the 4-km but KF CPS is applied on the outer domains. Exp. WS2KF is designed to be identical to WS2

except that KF CPS is applied on the 4-km domain as well. Comparison between Exps. WS2 and WS2KF indicates the effects of using a CPS on the 4-km grid along with the YSU PBL scheme.

#### 4.3.6 *Experiments WS3 and WS3GR*

Another CPS tested to improve the MM5 simulations in Deng and Stauffer (2005) was the Grell CPS. It was found that when the Grell CPS is used with Obs FDDA in the Phase 1 MM5 experiment set on the 4-km grid, the simulated precipitation field is even better with the use of the Grell scheme, with very light precipitation simulated over the entire 4-km resolution domain. The simulated wind field is very similar to that in experiments using KF CPS, with no divergent outflow boundaries or cold pools.

As summarized in Table 2, Exp. WS3 uses the M-Y-J Eta TKE PBL scheme, and WSM 3-class simple ice scheme. No CPS is applied on the 4-km domain but Grell CPS is applied on all the outer domains. To investigate the sensitivity of use of Grell CPS on the 4-km resolution grid, Exp. WS3GR is designed to be identical to WS3 except that it uses Grell CPS on the 4-km domain.

#### 4.4 *Evaluation Procedures*

Evaluation of a complex set of output fields generated by a numerical model is always a challenging task. There are several ways to verify the model's accuracy, but no single method is adequate by itself. For example, a statistical analysis of model performance, calculated from the errors between observed and simulated values of key variables, can give very useful insights that help to quantify the level of skill. However, because the statistics are generally calculated over

all the observing sites on an entire domain, they also may mask problems regarding how the model treats important mesoscale features, which cover only a portion of the domain. Therefore, subjective comparison of individual mesoscale features is a useful complement to a statistical analysis.

In this research we perform both subjective and objective evaluations of the model results. Evaluation of simulated meteorological features is accomplished by subjectively comparing the model's 4-km surface fields including precipitation and wind to the observed surface data and satellite images. The most effective objective approach to statistical evaluation of meteorological model fields is to use a variety of measures, instead of relying on one particular statistical score. In this research as discussed above, we developed software to convert the WRF output format to MM5 output format, so that our statistical software, VEROBS, can also be used to verify the WRF simulations.

Here, we use mean absolute errors (*MAE*), mean errors (*ME*), and index of agreement (*I*). The definition of each statistical measure is summarized here in the Appendix. Generally, these quantities are calculated as domain-wide averages for one or more layers. *MAE* gives a measure of the most "typical" error, in the sense that it is the average size of the absolute value of individual errors. Thus positive and negative errors cannot cancel one another (in contrast to *ME*, which reflects biases). The value of *I* ranges from 0 to 1, with a score of 1 representing perfect agreement to the data. It measures here how well the variability in the model wind speed matches the variability in the data, in a spatially paired manner. In mesoscale model applications, a value of *I* on the order of 0.5-0.6 is considered to be typical for a successful simulation of the wind field (e.g., Seaman et al. 1995, Lyons et al. 1995, Shafran et al. 2000).



## 5. MODEL RESULTS

To evaluate the model performance, both subjective and objective approaches are used in this research. Evaluation of simulated meteorological features is accomplished by subjectively comparing the model's 4-km surface fields including precipitation, surface wind, surface temperature and sea-level pressure to the observed surface data and satellite images. Objective evaluation is performed by comparing the statistical scores of the model-simulated fields including wind speed, wind direction, temperature, water vapor mixing ratio and sea-level pressure.

### 5.1 *Subjective Evaluation of the MM5- and WRF-Simulated Mesoscale Features*

To compare the structure of mesoscale features for the experiments listed in Table 2, we will mainly focus our discussion on the precipitation fields and the surface fields at the two model times used in Phase 1: 0900 UTC 19 September 1983 (21 h) and 1800 UTC 19 September 1983 (30 h). The 21-h time represents a night-time condition and the 30-h time represents a day-time condition. The 21-h model time is chosen because an infrared (IR) satellite image (not shown) is available near this time (0830 UTC 19 September 1983). It shows the cloud band associated with the frontal system and can be used to subjectively evaluate the model skill for precipitation. The current weather conditions were shown in Fig. 1a. The 30-h time is chosen because this is the time at which poor MM5 simulations on the 4-km grids were reported in the previous studies by Seaman et al. (2002), Stauffer and Deng (2004) and Deng and Stauffer (2005). The current weather conditions for this time are shown in Fig. 1b.

#### 5.1.1 *21-h model time*

Figures 4 through 13 show the MM5- and WRF-simulated 3-h precipitation fields and surface winds at 0900 UTC 19 September 1983 (21 h). Although the mesoscale features of the precipitation fields are somewhat different from one experiment to another, all experiments produce a banded structure of heavy precipitation associated with the frontal system. The observed frontal location for 0900 UTC 19 September 1983 is shown in Fig. 1a, and is included in all the precipitation panels in Figures 4 through 13. The model-simulated frontal position, plotted as a dashed curve in these figures, is determined using the low-level wind, temperature and sea-level pressure fields. Figure 1a confirms that convective clouds existed over the Great Lakes area, although there was no precipitation reported. Examination of the wind field at the lowest model layer indicates that the simulated frontal positions for each experiment are quite similar, and they are generally slower than the observed front at this time except at its southern edge to the west of Lake Erie. It is interesting that the larger errors in the position of the front at its southern extent occur in those experiments with the larger precipitation amounts and coverage at this time. Conversely, smaller frontal position errors to the west of Lake Erie occur in those experiments with the least amount of precipitation in that region (e.g., Exp. WB2 in Fig. 7, WB2KF in Fig. 9, WS2 in Fig. 10, and WS2KF in Fig. 11),

In order to compare the WRF simulations directly with MM5 simulations, a comparable MM5 experiment (Exp. MS11) that does not use FDDA is included because WRF currently does not have a FDDA capability. This MM5 experiment uses GSPBL scheme, RRTM radiation scheme for longwave, Dudhia scheme for the shortwave, simple ice microphysics and the new

Kain-Fritsch CPS on the 108/36/12-km domain. No convective scheme is applied on the 4-km domain.

Figure 4 shows the MM5-simulated 3-h precipitation field at 21 h in Exp. MS11. The observed (solid curve) and MM5-simulated (dashed curve) are also drawn in the figure. The simulated precipitation shows banded structure along the front through this region, and clearly shows over prediction of precipitation amount, with 57.6 mm over the region between Lake Huron and Lake Erie, 30.2 mm over Lake Erie, 26.9 mm over southern MI, 30.2 mm over Lake Erie and 17.0 mm over eastern New York (NY). Most of precipitation maxima are located ahead of the simulated front. The simulated cold front is slower to the north in Canada and faster over southern MI compared to the observed frontal locations.

Figure 5 shows the MM5-simulated 3-h precipitation field at 21 h in Exp. MS11KF, in which KF CPS is applied on the 4-km grid. As expected, the precipitation amounts are reduced due to the use of a CPS directly on the 4-km domain. The simulated precipitation still shows a banded structure along the front through this region, and the simulated maximum over the region between Lake Huron and Lake Erie is reduced from 57.6 mm in Exp. MS11 to 28.2 mm in Exp. MS11KF. This amount is still too high compared to the light observed precipitation, and the front is still moving too fast at its southern extent. The precipitation maximum over Lake Erie has now disappeared and precipitation maximum to the west of Lake Erie is reduced to 16.3 mm. The precipitation maxima over eastern NY is also reduced from 17.0 mm in Exp. MS11 to 10.2 mm in Exp. MS11KF. Also notice that the phase lag of the front in Canada is reduced compared to that in MS11 as the front and the back end of the frontal precipitation have moved eastward (compare Figs. 4a and 5a). Simulated winds generally agree with the overlaid observed winds in

Figs. 4b and 5b with southwesterly flow ahead of the front and northwesterly or westerly flow behind the front.

As described in the previous section, Exps. MS12 and WB2 are designed for a fair comparison between the MM5 and WRF simulations. Both experiments use similar physics (e.g., Eta M-Y PBL physics in MM5 and M-Y-J Eta TKE PBL in WRF, simple ice scheme microphysics in MM5 and WSM 3-class simple ice scheme in WRF). No CPS is applied on either 4-km domain. Figure 6 shows the MM5-simulated 3-h precipitation field and surface winds at 21 h in Exp. MS12 are fairly similar to those in MS11. Figure 7 shows the WRF-simulated 3-h precipitation field and surface winds at 21 h in Exp. WB2.

Comparison between MS12 and WB2 indicates that the 3-h precipitation amounts are again quite large (54.2 mm in MS12 and 33.6 mm in WB2). Experiment WB2, which uses a similar PBL scheme to that used in MS12, produces a very different precipitation pattern with no precipitation over Lake Erie and Lake Ontario. The 0600 UTC surface map (not shown) indicates convective precipitation near the western shore of Lake Erie, and the satellite photo at 0900 UTC 19 September 1983 (not shown) indicates enhanced cloudiness over Lake Erie and Ontario, but the 0900 UTC surface chart with limited data density in this region showed no precipitation. The MM5 experiment produced banded precipitation along the front through this region while Exp. WB2 produced most of its precipitation north of Lake Ontario in Canada. Some precipitation was observed in northwestern New York at 0900 UTC. The lack of precipitation over the Lake Erie region in Exp. WB2 may be related to the fact that the cold front in WB2 moves more slowly towards this region compared with that in the MM5 experiment, and there is no FDDA applied to correct phase errors in any of these MM5 or WRF experiments. The weak  $1.0 \text{ ms}^{-1}$  southerly wind to the south of the simulated front of WB2 in Fig. 7b suggests

that its position may be correct but there are no other observations in this region for corroboration.

When the KF CPS is directly applied on the 4-km domain, WRF and MM5 may be directly compared again in Exps. MS12KF and WB2KF. Figure 8 shows the MM5-simulated 3-h precipitation field at 21 h in Exp. MS12KF. Figure 9 shows the WRF-simulated 3-h precipitation field at 21 h in Exp. WB2KF. Comparison between Exps. MS12KF and WB2KF indicates that the WRF experiment produced less intense precipitation along the frontal system (e.g., 46.3 mm in MM5 vs. 17.9 mm in WRF to the north of Lake Erie) with its frontal system moving slower than that in MM5. Comparison between the experiments with and without KF CPS on the 4-km domain (i.e., MS12KF vs MS12 and WB2KF vs WB2) indicates that use of CPS on the 4-km domain does appear to generally reduce the precipitation amounts in both models, and the phase lag in the northern portion of the front is reduced in both models as the back end of the frontal precipitation also moves further eastward. Precipitation amounts are still grossly overestimated (exceeding 25 mm or one inch for this 3-hour period) in isolated areas with MS12KF values somewhat greater than those in MS11KF. Exp. WB2KF seems to have produced somewhat more precipitation coverage than WB2 towards the southern end of the front where narrow precipitation bands are oriented northwest-southeast. This peculiar banded structure does not appear in the MM5 experiments using KF on the 4-km domain. These bands in WRF are transverse to its low-level southwesterly wind flow (Fig. 9b).

Figures 10 and 11 show the WRF-simulated 3-h precipitation field at 21 h in Exp. WS2 and Exp. WS2KF, respectively, with no CPS applied on the 4-km domain in Exp. WS2 and with CPS in Exp. WS2KF. This set of experiments is identical to the previous set of baseline WRF experiments (Exp. WB2 and WB2KF) except that the YSU PBL scheme is used. Comparison of

Exp. WS2 (Fig. 10) with WB2 (Fig. 7) indicates that both experiments show quite similar 3-hourly precipitation patterns, with 12.6 mm in Exp. WS2 vs. 2.55 mm in Exp. WB2 over the area to the north of Lake Erie, and 20.5 mm in Exp. WS2 vs. 33.6 mm in Exp. WB2 near the northeastern side of Lake Ontario. Over the area north of Lake Ontario, the WS2 cold front moves slower than that in Exp. WB2 which may explain why its precipitation maxima is weaker over the northern side of Lake Ontario. The model-simulated surface-layer winds from these two YSU PBL simulations are much smoother than those in the WB2 experiments using a TKE PBL scheme. For example, the cyclonic wind shift across the front is much smoother in Fig. 10b (WS2) compared to Fig. 7b (WB2). Both YSU PBL experiments produce weaker precipitation amounts to the west of Lake Erie compared to MS12, and also have frontal positions closer to the analyzed front south of Lake Huron.

Using KF2 CPS on the 4-km domain in Exp. WS2KF produces more widespread precipitation patterns. Although some of the precipitation maxima are reduced, some new maxima have also appeared compared to Exp. WS2 in Fig. 10a. Again there are northwest-southeast bands apparent in the simulated 3-hourly precipitation. Thus, there is some degradation in the simulated 3-h precipitation field due to use of KF CPS on the 4-km domain at this time for this experiment. Comparison between Exp. WB2KF and WS2KF indicates some similarity in terms of precipitation distribution (Fig. 9a and Fig. 11a), but the western edge of the WB2KF precipitation region has advanced further east in Canada and its front is closer to the analyzed position.

Figures 12 and 13 show the WRF-simulated 3-h precipitation field at 21 h in Exps. WS3 and WS3GR, with no CPS applied on the 4-km domain in Exp. WS3 and with the Grell CPS applied directly to the 4-km domain in Exp. WS3GR. This set of experiments is identical to the

baseline WRF experiments (Exp. WB2 and WB2KF) except that Grell CPS scheme is used. In Exp. WS3, Grell CPS is applied only on the outer domains (108/36/12 km), and no CPS is applied on the 4-km domain. In Exp. WS3GR, Grell CPS is used on the 4-km domain as well. Comparison between Exp. WS3 (Fig. 12) and Exp. WB2 (Fig. 7) indicates that precipitation patterns in Exp. WS3 are more widespread, and several more precipitation maxima have appeared in MI, with 29.5 mm over central MI and 27.8 mm south of Lake Huron. The surface-layer winds also indicate that the southwestern part of the cold front moves faster in WS3 and crosses the MI and OH border. Applying GR CPS in Exp. WS3GR (Fig. 13) does not seem to reduce the precipitation amounts or frontal position errors at this time. Figure 13a shows 37.6 mm on the western lateral boundary (values in the artificial lateral boundary zone are ignored here) and 29.6 mm to the south of Lake Huron, compared to the 27.8 mm in this region in WS3 (Fig. 12a). Although some maxima are reduced (e.g., from 19.6 mm in Exp. WS3 to 13.5 mm in Exp. WS3GR) over the eastern side of Lake Ontario, precipitation coverage is also increased. It is interesting that WS3GR does not show the northwest-southwest narrow precipitation bands apparent in WB2KF (Fig. 9a) and WS2KF (Fig. 11a) at this time. Perhaps the Grell CPS scheme, known to transition convective precipitation more quickly to the grid-resolved precipitation than KF CPS, may be expected to produce results more similar to those using only explicit grid-resolved precipitation. It is not clear why there are no narrow northwest-southeast precipitation bands in the MM5 experiments at this time using KF on the 4-km domain (Figs. 5a and 8a).

Table 3 summarizes the maximum 3-hourly precipitation values for all experiments ending at 21 h (0900 UTC 19 September 1983). Exp. WS2 using the YSU PBL produces the smallest precipitation amounts and coverage at this time, but the baseline WRF experiment WB2

appears to have some advantages over WS2 in terms of the frontal location and surface-layer winds. The WS2 surface-layer wind field is generally smoother than that of any of the other experiments, and does not appear to agree as well with the surface observations overlaid on the simulated wind fields. Addition of a CPS on the 4-km domain does appear to significantly reduce the maximum precipitation values, “grid point storms”, on the 4-km domain while moving the back (western) edge of the precipitation area further to the east and closer to the analyzed front for all experiments except WS2 and WS3. Experiments WS2KF and WS3GR also produce greater precipitation coverage at this time than WS2 and WS3, respectively.

Figure 14 shows the MM5- and WRF-simulated PBL height along the northwest-southeast cross section shown in Fig. 3 for all experiments on the 4-km resolution domain at 21 h (0900 UTC 19 September 1983). The PBL depths are generally shallower along the eastern portion (right side) of the cross section over the ocean. It is shown that the WRF experiments that use the YSU PBL scheme (curves 6 and 7, Exps. WS2 and WS2KF) produce a PBL height equal to the first model layer depth (32 m) for these night-time conditions. The YSU PBL scheme in WRF uses stability based on bulk Richardson number to determine the PBL depth, instead of using TKE. The MM5 experiments using the GS PBL (curves 0 and 1) produce night-time PBL depths of around 210 m, the MM5 experiments using M-Y Eta PBL (curves 2 and 3) produce somewhat deeper PBL depths of 336 and 370 m. The M-Y-J Eta PBL experiments in WRF (curves 4 and 5) produce even deeper PBL depths of 516 and 534 m, and the deepest PBL depths of 537 and 620 m are found in those WRF experiments using the Grell CPS (curves 8 and 9, WS3 and WS3GR). Observed PBL depth is not available for comparison, but those experiments with night-time PBL depths exceeding 1000 m (WS3 and WS3GR) are noted



### 5.1.2 30-h model time

Observed surface conditions at 1800 UTC 19 September 1983 over the 4-km domain indicate no reported precipitation (Fig. 1b). Note the general southwesterly flow through most of Ohio (OH) and Pennsylvania (PA) to the south of the stationary front. There are some surface stations having obstructions to visibility (e.g., fog, haze, etc.) mainly along the front from west to east through northern Lake Erie and central NY and also along a trough extending northeast-southwest through New England into New Jersey (NJ) and Maryland (MD). Cloudy skies are found further to the north of the cold front. The satellite photo at this time (not shown) confirmed the absence of significant clouds over PA and southern NY.

At the 30-h time, Fig. 15a shows the MM5-simulated 3-h precipitation field at 1800 UTC September 1983 (30 h) in Exp. MS11. The simulated precipitation indicates a banded structure along the front and clearly shows over prediction of precipitation amounts, with 38.0 mm, 22.5 mm and 31.3 mm over northern OH and over Lake Erie, and 32.8 mm near the NY and PA border. Most of precipitation maxima are located near or behind the dashed wind shift line in the simulated surface wind field (Fig. 15b). This wind shift line marks the southern edge of convective outflow boundaries as revealed by several cold pools (i.e., minimum surface temperature values highlighted in red) and surrounding surface temperature gradient fields (Fig. 15c). These divergent northerly winds in northern OH do not agree with the surface wind observations. Over Lake Erie, to the north of the wind shift line, there are two northwesterly wind observations over Lake Erie where model-simulated flow is also weak and northerly. To the south of this wind shift line, the simulated surface layer southwesterly flow over most of PA is quite consistent with the observed wind field. These outflow boundaries related to intense grid point storms seriously disrupt the low-level flow fields.

When the KF CPS is applied on the 4-km domain in Exp. MS11KF, the MM5-simulated 3-h total precipitation field (Fig. 16a) indicates that the precipitation maxima are generally reduced over the Lake Erie region and the cold pool (Fig. 16c) is also more than 1 °C warmer than that in Fig. 15. The simulated surface wind shift location in Fig. 16b is similar to that in Exp. MS11, but the northwesterly winds over Lake Erie are closer in magnitude and direction to the observed values. Reducing the intensity of the grid point storm problem reduces the model precipitation and hence improves the low-level mass and wind fields in that region.

Figure 17a shows the MM5 simulated 3-h total precipitation in Exp. MS12 at 30 h (1800 UTC 19 September 1983). It is shown that MS12 produces similar precipitation patterns to Exp. MS11 along the front over Lake Erie, but Exp. MS12 using the M-Y Eta PBL scheme produces much larger precipitation maxima (e.g., 69.8 mm/3h over Lake Erie, 41.2 mm over northern OH). The simulated surface wind field is similar to that in Exp. MS11, but the wind shift line extends even further east over northern PA and southern NY where the observed surface flow is from the southwest (Fig. 17b). Some of the surface cold pools are more than 1.5 – 2.0 °C cooler (15.2 °C to 13.6 °C, 18.9 °C to 16.8 °C) with the larger precipitation amounts in MS12 compared to MS11.

The WRF-simulated 3-h total precipitation at 30 h for Exp. WB2 (Fig. 18a) shows that that the 3-h precipitation at this time is located further north between Lake Erie and Lake Huron, with precipitation maxima of 38.4 mm/3 hour to the southwest of Lake Huron. The location of the precipitation band is consistent with the location of the wind shift line in Fig. 18b. The precipitation is again behind the wind shift line as expected. The WB2 surface cold pools in Fig. 18c are somewhat warmer and located to the northwest of those in MS12.

The 3-h total precipitation at 30 h with the addition of the CPS on the 4-km domain in Exp. MS12KF (Fig. 19a) is similar to MS12 in its general precipitation patterns along the front over Lake Erie, but MS12KF produces much lower maxima in northwest PA (18.2 mm vs. 69.8 mm) and north central OH (33.3 mm vs. 41.2 mm). Apparently the convective energy is reduced near the grid point storm locations but is spread to other surrounding areas by applying KF on the 4-km domain, and some precipitation amounts are made larger in southwestern NY. The simulated surface wind field (Fig. 19b) is also quite similar to MS12, but the wind shift line extends from northern OH to central NY where the simulated winds show good agreement with the northwesterly surface wind observations north of the front (see Fig. 1b). The cold pools are weaker in Fig. 19c due to the lighter precipitation amounts, and the simulated surface meteorology is improved.

When the KF CPS is applied on the 4-km domain in WRF, Exp. WB2KF (Fig. 20a) produces a similar precipitation pattern compared to Exp. WB2 but with somewhat greater coverage and reduced precipitation maxima (e.g., 31.1 mm vs. 38.4 mm south of Lake Huron). Both WRF experiments produce precipitation patterns shifted somewhat to the northwest of those produced by using the MM5. WRF 3-h precipitation ending at this time covers the southern tip of Lake Huron while that in MM5 is located further south and east. Again both models still have 3-hourly precipitation amounts exceeding 25 mm, so the grid-point storm problems have not been completely eliminated. The heaviest precipitation band being located further to the north in WRF compared to that in MM5, suggests different phasing in the frontal system between the two models. The corresponding wind shift line in the WRF-simulated surface wind field is also displaced to the north and west of that in MM5 (compare Fig. 20b to Fig. 19b). Both WRF experiments produce southwesterly flow over Lake Erie where surface

observations and the MM5 experiment MS12KF in Fig. 19b show northwesterly winds. The front in WRF appears to be too slow at this time. The cold pools in Fig. 20c for Exp. WB2KF are a few tenths of a degree °C warmer than those in WB2, consistent with the reduced precipitation amounts caused by applying CPS on the 4-km domain.

Figure 21a shows the WRF-simulated 3-h total precipitation at 30 h in Exp. WS2, which uses the YSU PBL scheme and no CPS is applied on the 4-km domain. It is shown that the WRF-simulated precipitation is mainly located over western NY and the Lake Ontario region, with the maximum precipitation amount of 12.8 mm over western NY. The simulated surface wind field (Fig. 21b) shows southwesterly flow over Lake Erie and the same northward shift of the front as seen in WB2 and WB2KF, but it does not show any significant wind shift line near the precipitation maxima, only some diffluence to the east of the northern shore of Lake Erie. As expected the cold pools in Fig. 21c are very weak (19 – 20 °C) associated with the much lighter precipitation amounts.

The WRF-simulated 3-h total precipitation at 30 h for Exp. WS2KF is shown in Fig. 22a. Again, the use of KF CPS on the 4-km domain with the YSU PBL causes the precipitation patterns to become more wide spread with increased precipitation amounts. There is a 3-hourly precipitation maximum of 23.9 mm near the Niagara Falls region. Thus the use of KF CPS directly on the 4-km domain in this experiment has some negative effects on precipitation. As in Exp. WS2, the simulated surface wind field is one of the smoothest surface wind patterns (Fig. 22b) and it shows only a slight wind shift line to the east of Lake Erie. Again, Fig. 22c shows that the cold pools have surface temperature minima between 19 °C and 20 °C and are very weak.

Figure 23a shows the WRF-simulated 3-h total precipitation at 30 h in Exp. WS3, which uses the Eta PBL scheme and no CPS is applied on the 4-km domain, but Grell CPS is applied on

all outer domains rather than KF. The WS3 WRF-simulated precipitation distribution has less coverage and organization compared to the baseline WB2, but its isolated patterns include a 40.0 mm maximum over southwestern NY. The other precipitation areas are much weaker. The simulated surface wind field (Fig. 23b) shows the typical WRF southwesterly flow over Lake Erie at this time and a weak wind shift to the east of the maximum precipitation region where a minimum surface temperature of 18.5 °C is located in Fig. 23c.

The 30-h 3-hourly total precipitation results for Exp. WS3GR are shown in Figure 24a. Experiment WS3GR uses the Eta PBL scheme but with Grell CPS also applied directly on the 4-km domain. The use of Grell CPS on the 4-km domain causes the precipitation patterns to become more wide spread and there are precipitation maxima of 23.0 mm and 33.8 mm over southwestern NY and northeastern OH. A weak wind shift line (Fig. 24b) exists in northwestern PA where an 18.2 °C surface temperature minimum is located (Fig. 24c). Thus, use of Grell CPS on the 4-km grid reduced the maximum precipitation amount at this time but failed to completely eliminate the grid point storm issues.

So overall, the MM5 experiments produced somewhat better results for the position of the front around Lake Erie at this 30-h time, and except for Exp. WS2, the addition of a CPS on the 4-km domain generally reduced the total 3-hourly precipitation (Table 3) and the grid point storm problems in both models. Although reduced precipitation amounts produced weaker surface cold pools and less disruption to the low-level wind flows, precipitation totals were still too large and grid-point storm issues still remain. Table 3 also shows that Exp. WS2 again produced the smallest amounts of precipitation of any of the experiments at this time. These conclusions regarding reduction of maximum total precipitation with the addition of CPS on the 4-km domain are also generally valid for the 30-h total precipitation maxima as well (Table 3).

Figure 25 shows the MM5- and WRF-simulated PBL height for the day time along the same northwest-southeast cross section shown in Fig. 3 for all experiments on the 4-km resolution domain at 30 h (1800 UTC 19 September 1983). There are no measurements at this time for verification so this figure only documents the differences among all the model experiments. Similar to the MM5 MRF PBL results in Phase 1 of this study, the YSU PBL in WRF in Exps. WS2 and WS2KF (curves 6 and 7) produces the deepest PBL heights of 948 and 942 m. Among all the other PBL schemes that are based on TKE to determine the PBL depth, the GS TKE PBL scheme in MM5 (curves 0 and 1) and the Eta M-Y PBL in MM5 (curves 2 and 3) produce lower PBL depths (on average) than the M-Y-J Eta TKE PBL scheme in WRF (curves 4, 5, 8 and 9). The lowest PBL heights at this time (449 m and 552 m) are produced by the Eta TKE PBL in MM5 experiments MS12 and MS12KF. In the next section, the surface temperature biases and many other statistics will be examined to further understand the subjective results reported in this section.

## **5.2 *Objective Evaluation of the MM5 and WRF Solutions Using a Statistical Approach***

The subjective examination of the mesoscale and synoptic-scale structures simulated by the MM5 and WRF models in the previous section led to some preliminary conclusions; this section objectively examines the model's statistical performance for Episode 1 of the CAPTEX '83 study to further test these findings. The statistical measures of accuracy selected for this evaluation were described in the previous section and are summarized in Appendix A. The statistics are calculated over the entire 4-km domain.

Since WRF uses a different terrain-following vertical coordinate (see Section 2 for model descriptions), in order to use the existing verification software that was used in Phase 1 of this

project to verify the MM5 model output, a WRF to MM5 output converter was developed in this phase of the project. The converting software interpolates the WRF output from WRF vertical coordinate heights onto the MM5 vertical model layer heights, so that the existing VEROBS verification software can be used with minimal modification.

Although all statistical measures including root mean square errors (RMSE), mean absolute errors (MAE), mean errors (ME), index of agreement (I) (Willmott et al. 1985) are computed for the MM5- and WRF-simulated wind and mass fields, only MAE and ME scores are discussed here. It is worth noting that interpolations necessarily cause the initial-condition statistics between the two models, MM5 and WRF, in the time series plots below to be somewhat different, and the vertical interpolations of the raw WRF profiles to the MM5 sigma levels for verification against sonde data at 0, 12 and 24 h also introduces some uncertainty in the direct comparison.

#### *5.2.1. Wind Speed*

Figure 26 shows the MAE and ME as a function of time for model-simulated surface layer wind speed for all experiments, Exps. MS11, MS11KF, MS12, MS12KF, WB2, WB2KF, WS2, WS2KF, WS3 and WS3GR, in CAPTEX-83 Episode 1 (1200 UTC 18 September - 1800 UTC 19 September 1983) on the 4-km verification domain. This order will be the exact order of all experiment curves used in any of the statistical plots in this section. So Exp. MS11 will always be curve 0 and WS3GR will always be curve 9. This format was already adopted for Figs. 14 and 25 showing model-simulated PBL height in the last section. The 30-hour mean statistics are plotted on the right side of the chart with the digital values also included above the experiment key at the bottom of the figure. These 30-h mean values are also summarized in

Tables 4 and 5 for the surface-layer MAE and ME statistics for all variables. Bold values in the tables show the better entry between each no-CPS and CPS experiment, underlined values denote the best value within each CPS-experiment set and each no-CPS experiment set, and the asterisk indicates the best value over all experiments for each variable.

For MAE surface wind speed score, Fig. 26a shows that the WRF experiment using YSU PBL scheme (Exp. WS2 and WS2KF) has the largest surface wind speed errors, and the WRF experiments using the M-Y-J Eta TKE PBL (Exp. WB2, WB2KF, WS3 and WS3GR) produce the smallest error in surface layer wind speed. The errors are generally larger during the night-time hours (12- 24 h) for most experiments. The MM5 experiment using GS TKE PBL (Exp. MS11 and MS11KF) also shows relatively large error in surface layer wind speed, but it is similar to or smaller than that in the WRF experiment using YSU PBL scheme (Exp. WS2 and WS2KF). Differences in the surface wind statistics due to the addition of CPS on the 4-km domain (see each pair of curves with the same color) are generally small and statistical results are sometimes better and sometimes worse with the CPS.

As described in the experimental design section, a fair direct comparison between MM5 and WRF can only be made among Exps. MS12, MS12KF, WB2 and WB2KF. Figure 26a also shows that the WRF experiments (Exp. WB2 and WB2KF) have slightly smaller ( $0.1 - 0.2 \text{ ms}^{-1}$ ) MAE error in surface layer wind speed than the MM5 experiments (Exp. MS12 and MS12KF). Thus, WRF appears to have a small advantage over MM5 in simulating the surface layer wind speed in this case.

For ME score of the model-simulated surface layer wind field, all experiments appear to have a positive bias, meaning that the wind speed is  $1 - 2 \text{ ms}^{-1}$  too fast on average in the model, especially during the night-time hours. Comparison among all experiments indicates that the



WRF experiment using YSU PBL scheme has the largest bias (curves 6 and 7). The smallest bias errors belong to the WRF experiments using M-Y-J Eta TKE PBL scheme (Exps. WB2, WB2KF, WS3 and WS3GR). The MM5 and WRF comparison between Exps. MS12 and MS12KF (curves 2 and 3) with Exps. WB2 and WB2KF (curves 4 and 5) indicates that WRF again has small advantage over MM5 in the ME score of the model-simulated surface layer wind speed. Again the case-mean statistics for each CPS pair of experiments are generally similar.

Figure 27 shows the vertical profiles of the 30-h averaged MAE and ME for MM5- and WRF-simulated wind speed for all experiments on the 4-km verification domain. The 32-layer mean statistics are plotted on the top of the chart with the digital values also included above the experiment key at the bottom of the figure. Tables 6 and 7 summarize the ME and MAE averaged in the vertical and over the 30-h period for each experiment and variable. Figure 27a shows that above the surface layer Exp. MS11 (curve 0) has the largest MAE error. Use of the KF CPS on the 4-km domain has improved its MAE (Exp. MS11KF, curve 1), starting in the lower PBL and moving upwards. The experiment with the smallest MAE error (on average) appears to be the WRF experiments using the M-Y-J Eta TKE PBL and Grell CPS (Exps. WS3 and WS3GR). However the added value of using a CPS on the 4-km domain (comparing curves 8 and 9) is not clear, with improvements in some layers and degradations in others and both showing the same vertical average statistic ( $1.72 \text{ ms}^{-1}$ , Table 6). Experiment WS2 (curve 6) has the largest value at the surface and lowest value near 200 m, and use of KF CPS in Exp. WS2KF produces a slight degradation throughout the entire atmosphere for MAE and ME (Fig. 27b).

The comparison between MM5 and WRF indicates that Exp. WB2 and WB2KF (curves 4 and 5) have smaller MAE error in the boundary layer, but larger error above the boundary layer than Exp. MS12 and MS12KF (curves 2 and 3). The WRF wind speed bias is somewhat lower

than MM5 on average with MM5 having a small positive bias of  $\sim 0.3 \text{ ms}^{-1}$  and WRF a small negative bias of  $\sim 0.4 \text{ ms}^{-1}$  (Table 7). Overall the WRF experiments are slightly better than MM5 experiments in MAE wind speed scores. For both WRF and MM5 sets of experiments, use of CPS on the 4-km domain does not indicate any consistent significant improvement in MAE wind speed scores.

In general, the ME wind speed scores, in Fig. 27b show that MM5- and WRF-simulated wind speed is too fast in the lower portion of the boundary layer, and too slow in the upper part of the atmosphere, with WRF experiments involving YSU PBL scheme having the largest negative bias overall. In the boundary layer, both MM5 sets of experiments (Exps. MS11, MS11KF, MS12 and MS12KF) show relatively large positive bias in model-simulated wind speed, with Eta PBL scores slightly better than GS PBL. The WRF experiments involving M-Y-J Eta TKE PBL and Grell CPS have the smallest bias overall, and especially in the middle portion of the atmosphere, between 400 and 2000 m.

Comparing Exps. WB2 and WB2KF with Exps. MS12 and MS12KF also indicates that WRF appears to have smaller bias in the boundary layer, but larger bias in the upper atmosphere than MM5. Again, use of CPS on the 4-km domain does not produce significant improvements in ME scores. However, some apparent improvement in ME scores by use of CPS on the 4-km domain does appear in Exp. MS11KF in the boundary layer, and in WS3GR and WS2KF in the middle layers.

The index of agreement (I) as a function of time for model-simulated surface layer wind speed and 30-h mean wind speed profile for all experiments is shown in Fig. 28. Recall that the perfect score for I is 1.0. The 30-hour mean statistics are plotted on the right side of the chart with the digital values also included above the experiment key at the bottom of the figure. All

experiments show  $I$ , representing the wind anomaly structure at the surface, generally decreasing with time through the period. It is shown that consistent with the MAE and ME scores discussed above, WRF experiments using YSU PBL physics receive the worst  $I$  score for wind anomaly structure at the surface. This is not too surprising since these WS2 YSU-PBL experiments did show very smooth horizontal wind fields in the last section. The WRF experiments using M-Y-J Eta TKE PBL have better (higher)  $I$  scores. The best  $I$  scores at the surface belongs to WB2 and WB2KF by a very small margin (0.01) over WS3 and WS3GR. The comparison between MM5 and WRF shows that WRF has a small advantage (0.02 or 0.03) over MM5 in  $I$  score in the model-simulated surface layer wind speed when both models use the Eta TKE PBL. Use of the Eta PBL in MM5 in MS12 and MS12KF improved the surface  $I$  score by 0.03 – 0.04 compared to GS PBL in MS11 and MS11KF (Table 5). Experiments MS11 and MS11KF have the second worst  $I$  scores at the surface, Use of CPS on the 4-km domain produces little change and increases or decreases the surface  $I$  score by only  $\sim 0.01$  for each set of the experiments (Table 5).

The vertical profiles of the 30-h averaged  $I$  score for MM5- and WRF simulated wind speed for all experiments (Fig. 28b) indicate that WRF experiments using M-Y-J Eta TKE PBL and Grell CPS produce the best  $I$  score profile on average by a small margin (0.01 – 0.03), and that all of the experiments have very similar values ranging from 0.89 to 0.93 (Table 7). Comparison between MM5 (Exp. MS12 and MS12KF) and WRF (WB2 and WB2KF) indicates that MM5 has a slightly better  $I$  score overall for the vertical profile of horizontal wind anomaly structure (0.91 vs. 0.90). In the low layers MM5 and WRF have comparable  $I$  scores, and in the middle layers, MM5 is better than WRF.

### 5.2.2. Wind Direction

Figure 29 shows the MAE and ME as a function of time for model-simulated surface layer wind direction for all ten experiments, Exp. MS11, MS11KF, MS12, MS12KF, WB2, WB2KF, WS2, WS2KF, WS3 and WS3GR, in CAPTEX-83 Episode 1 (1200 UTC 18 September - 1800 UTC 19 September 1983) on the 4-km verification domain. The 30-hour mean statistics are again plotted on the right side of the chart with the digital values also included above the experiment key at the bottom of the figure. Figure 29a shows that the MAE scores for all ten experiments are very similar, with Exps. WB2KF and MS12KF having the best two scores at 30.62 and 30.72 degrees, and Exp. WS2KF having the worst score at 31.89 degrees for the model-simulated surface layer wind direction. Thus the range in wind direction errors is only about 1.0 degree on average with an average MAE of around 30 degrees (Table 4). For ME score, Fig. 29b shows that the surface values are generally in the range of plus or minus 15 degrees. WRF experiments involving use of YSU PBL physics have the largest bias on average in the WRF-simulated surface layer wind direction (7 – 8 degrees, Table 5). The comparison between MM5 (Exp. MS12 and MS12 KF) and WRF (Exp. WB2 and WB2KF) indicates that MM5 has the smaller bias errors through the first 24 hours and then somewhat larger values during the last 6 hours when convective outflow boundaries are simulated in both models.

Figure 30 shows the vertical profiles of the 30-h averaged MAE and ME for MM5- and WRF-simulated wind direction for all ten experiments. The 32-layer mean statistics are plotted on the top of the chart with the digital values also included above the experiment key at the bottom of the figure. The difference among all experiments in the vertical mean MAE wind direction is only around 2 degrees but larger differences exist from layer to layer. The WRF experiments (Exp. WS3 and WS3GR) using M-Y-J Eta TKE physics and Grell CPS have the

smallest MAE error in the boundary layer and on average, and the use of CPS on the 4-km domain in Exp. WS3GR shows some slight degradation in the boundary layer. Experiments MS11 and MS11KF appear to have the next best MAE scores in model-simulated wind direction in the boundary layer. The rest of the experiments have very similar MAE scores, and their differences are not significant. Thus direct comparison between MM5 (Exp. MS12 and MS12KF) and WRF (Exp. WB2 and WB2KF) does not produce a clear winner in MAE for model-simulated wind direction for which there is only a  $\sim 1.0$  degree difference on average (Table 6) .

The vertical profiles of the 30-h averaged ME (Fig. 30b) show that the WRF experiments using YSU PBL physics (Exp. WS2 and WS2KF) have large positive bias in the lower portion of the boundary layer, although their ME scores are quite small in the upper atmosphere, and they are smallest over all layers (Table 7). The ME wind direction profiles are very similar among the set of experiments.

### 5.2.3. Vector Wind Difference

Figure 31a shows the surface-layer MAE vector wind difference (VWD) as a function of time. The VWD MAE combines both the speed and direction errors. Because the VWD is positive definite, the ME and MAE VWD would be exactly the same value so it does not matter which statistic is chosen. Similar to the MAE score of the model-simulated surface-layer wind speed, the WRF experiments using YSU PBL physics (Exps. WS2 and WS2KF) show the largest MAE VWD errors ( $3.59 \text{ ms}^{-1}$  and  $3.66 \text{ ms}^{-1}$ , Table 4). The second largest MAE error belongs to the MM5 set of experiments using GS TKE PBL scheme (Exps. MS11 and M11KF). Both above WRF and MM5 experiment sets indicate some slight degradation in MAE scores when KF

CPS is applied on the 4-km domain. A fair direct comparison between MM5 (Exps. MS12 and MS12KF, curves 2 and 3) and WRF (Exps. WB2 and WB2KF, curves 4 and 5) experiment sets indicates that WRF appears to have around  $0.1 - 0.2 \text{ ms}^{-1}$  better MAE scores in the model-simulated surface VWD. The WRF experiments using M-Y-J Eta TKE PBL and Grell CPS (Exp. WS3 and WS3GR) also show quite small MAE errors (similar to Exps. WB2 and WB2KF) in the surface VWD.

Figure 31b shows the vertical profiles of the 30-h averaged MAE VWD for all ten experiments. Similar to the MAE score of the model-simulated wind speed (Fig. 27a), the best MAE VWD score belongs to the WRF experiment using M-Y-J Eta TKE PBL and Grell CPS (Exp. WS3 and WS3GR), especially in the boundary layer, with slight degradation of MAE score when Grell CPS is also applied on the 4-km domain (Exp. WS3GR). The next best MAE VWD score belongs to the WRF experiment using YSU PBL physics (Exp. WS2 and WS2KF), again with slight degradation when KF CPS is also applied on the 4-km domain. Overall, the MM5 experiment with GS TKE PBL and KF CPS indicates the largest MAE errors.

Direct comparison between MM5 and WRF (Exps. MS12 vs WB2 and MS12KF vs WB2KF) indicates that, overall, the results are similar with and without CPS on the 4-km domain, and WRF is  $\sim 0.2 \text{ ms}^{-1}$  better than MM5 on average. The WRF experiments for the vertical profiles in Fig. 31b show slightly better performance in the lowest few hundred meters and MM5 is somewhat better at higher layers. The VWD errors in this case largely reflect the wind speed errors since the wind direction errors are very similar among the set of experiments.

#### 5.2.4. Temperature

Figure 32 shows the MAE and ME as a function of time for model-simulated surface-layer temperature for all ten experiments, Exp. MS11, MS11KF, MS12, MS12KF, WB2, WB2KF, WS2, WS2KF, WS3 and WS3GR, in CAPTEX-83 Episode 1 (1200 UTC 18 September - 1800 UTC 19 September 1983) on the 4-km verification domain. Surface temperature errors are generally largest in the last 6 h of the simulation when convection and surface cold pools are affecting most of the model experiments, as discussed in the previous section. Figure 32a and Table 4 shows that the MM5 experiment set using GS TKE PBL and KF CPS (Exp. MS11 and MS11KF) have the smallest MAE errors (1.76 °C and 1.82 °C) in simulated surface-layer temperature. Thus use of KF CPS on the 4-km domain in MM5 produces a slight improvement in the MAE score. The second best experiment set is the WRF experiment set using the YSU PBL scheme and KF CPS (Exp. WS2 and WS2KF). The WRF experiment set that uses M-Y-J Eta TKE PBL physics and Grell CPS has the largest MAE in the simulated surface-layer temperature (2.34 °C and 2.38 °C).

Comparison of MM5 and WRF using Exps. MS12 and WB2, and Exps. MS12KF and WB2KF reveals that Exp. MS12 is slightly better than WB2, and Exp. MS12KF is slightly better than WB2KF in MAE score of the model-simulated surface layer temperature field (Table 4). Thus, MM5 appears to have some small advantage in simulating the surface-layer temperature field when both models use Eta PBL, and the MM5 advantage is especially large when using the GS PBL in MS11 and MS11KF where the surface temperature errors are around 0.5 °C smaller than those in WRF.

For ME score, Fig. 32b shows the large negative bias in surface temperature related to the cold pools in the last 6 h of the simulations. The WRF experiment set that uses the YSU PBL

scheme and produces the least precipitation also has the smallest surface temperature bias. Experiments MS11 and MS11KF also show relatively small bias, and the use of KF CPS on the 4-km domain slightly improves the ME score (Exp. MS11KF vs. Exp. MS11). The WRF experiment set, Exps. WS3 and WS3GR, shows very similar ME distribution to that in Exps. WB2 and WB2KF, and the MM5 experiments MS12 and MS12KF, implying that the PBL physics play a major role in controlling the model performance in this case.

Figure 33 shows the vertical profiles of the 30-h averaged MAE and ME for MM5- and WRF-simulated temperature field for all ten experiments. The MAE distribution (Fig. 32a) shows that both MM5 experiment set using GS TKE PBL scheme and KF CPS and the WRF experiment set using YSU PBL scheme and KF CPS have relatively small MAE error in model-simulated temperature field, with WRF slightly better in the lower PBL and MM5 better in the upper PBL. Overall the MM5 is better and Exp. MS11KF has the smallest MAE error of all experiments. The WRF experiment using M-Y-J Eta TKE PBL scheme and Grell CPS (Exps. WS3 and WS3GR) have relatively large MAE error in model-simulated temperature field, with Exp. WS3GR having the largest MAE error overall. Direct comparison between MM5 (Exp. MS12 and MS12KF) and WRF (Exp. WB2 and WB3KF) shows that the MAE score for MM5 and WRF are quite similar, with WRF being slightly better in lower atmosphere and MM5 being slightly better in upper atmosphere. On average, MM5 (curves 2 and 3) is better than WRF (curves 4 and 5). It is also noticed that curve 3 is better than curve 2, and curve 5 is better than curve 4, indicating that use of CPS on the 4-km domain has improved the model-simulated temperature field, although the improvement is small.

The ME score distribution (Fig. 33b) shows the MM5 experiment set, Exps. MS11 and MS11KF, to have the smallest bias on average through all the model layers. The WRF



experiment set, Exps. WS2 and WS2KF, also has small bias in the boundary layer, with slightly positive bias in the lower PBL and slightly negative bias in the upper PBL. All the WRF experiments (Exps. WB2, WB2KF, WS3 and WS3GR) that use M-Y-J Eta TKE PBL scheme appear to have very similar ME score distribution in the boundary layer, with the largest ME in middle of the boundary layer around 500 m. All ten experiments have a mean vertical profile temperature bias less than 0.25 °C (Table 7).

#### 5.2.5. *Water Vapor Mixing Ratio*

Figure 34 shows the MAE and ME as a function of time for model-simulated surface-layer water vapor mixing ratio for all ten experiments, Exp. MS11, MS11KF, MS12, MS12KF, WB2, WB2KF, WS2, WS2KF, WS3 and WS3GR, in CAPTEX-83 Episode 1 (1200 UTC 18 September - 1800 UTC 19 September 1983) on the 4-km verification domain. Figure 34a shows that on average over the 30-h period, the MAE increases with time for all experiments. The MM5 experiment set, Exps. MS11 and MS11KF, has the best MAE score in model-simulated surface-layer water vapor mixing ratio, and the MM5 experiment set, Exps. MS12 and MS12KF, has the worst MAE score. Closer examination of all the curves in Fig.34a indicates use of CPS on the 4-km domain does not show significant differences in simulated surface-layer water vapor mixing ratio. The range of values over all experiments is only 0.15 g kg<sup>-1</sup>. The WRF experiment set, Exps. WS2 and WS2GR, which uses the YSU PBL scheme and KF CPS shows an interesting error distribution with time, with MAE error initially increasing more rapidly than the other experiments until 9 h, and then decreasing until 15 h and then increasing again. This may be related to its higher day-time PBL heights compared to the other experiments (Fig. 25) mixing down much drier air to the surface. Note that the YSU PBL experiments (WS2 and

WS2KF) have a much larger dry bias during this day-time period and a dry bias on average for the entire 30-h period (Fig. 34b).

The ME score distribution as a function of time (Fig. 34b) shows larger positive (moist) errors during the night-time hours (12 – 24 h) and smaller negative (dry) errors during the day-time hours. Note that the daytime dry bias may be correlated to the depths of the day-time mixed layer shown in Fig. 25 with the driest experiments (WS2 and WS2KF) also producing the highest PBL depths and the moistest model runs (MS12 and MS12KF) producing the lowest PBL depths. The moistest model runs with the lowest PBL depths also had the coldest surface temperature bias (see Exp. MS12 in Table 5). Experiments MS11 and MS11KF have the smallest bias in simulated surface-layer water vapor mixing ratio, with Exp. MS11KF (which uses KF CPS on the 4-km domain) having smaller bias than Exp. MS11. Experiment MS12KF also has a slightly smaller moist bias at the surface than MS12. The direct comparison between MM5 and WRF (comparing Exp. MS12 and MS12KF with WB2 and WB2KF) indicates that WRF has a smaller bias score in model-simulated surface-layer water vapor mixing ratio by about  $0.3 \text{ g kg}^{-1}$ .

Figure 35 shows the vertical profiles of the 30-h averaged MAE and ME for MM5- and WRF-simulated water vapor mixing ratio field for all ten experiments. It is shown in Figure 35a that the WRF experiment set, Exps. WS2 and WS2KF that use the YSU PBL scheme, has the smallest MAE error in the boundary layer, with use of KF CPS on the 4-km domain showing further improvement in the simulated water vapor mixing ratio field. The behavior of YSU PBL scheme in WRF seems to have a similar behavior to the MRF scheme in MM5 (Deng and Stauffer 2005). The MM5 experiment set (Exps. MS12 and MS12KF) has the largest MAE error, with use of KF CPS on the 4-km domain having some improvement in the model-

simulated water vapor mixing ratio field. Thus, the comparison between MM5 and WRF (comparing Exps. MS12 and MS12KF with WB2 and WB2KF) shows that WRF performs slightly better than MM5 (by  $0.1 \text{ g kg}^{-1}$ ) in simulating water vapor mixing ratio. Note that the MM5 experiment set, Exps. MS11 and MS11KF, that uses GS TKE PBL scheme and KF CPS, has very similar MAE vapor mixing ratio to MS12 and MS12KF (Table 6).

Figure 35b shows the vertical distribution of the ME score in model-simulated water vapor mixing ratio. It is shown again that WRF experiment set, Exp. WS2 and WS2KF, has the smallest moisture bias, and the next best experiment set is the MM5 experiments, Exps. MS11 and MS11KF (Table 7). The worst ME score belongs to the MM5 experiment set, Exp. MS12 and MS12KF, and the second worst belongs to Exps. WS3 and WS3GR. Thus, the fair comparison between MM5 and WRF (comparing Exp. MS12 and MS12KF with WB2 and WB2KF) indicates that WRF is slightly better (by  $0.05 \text{ g kg}^{-1}$ ) in simulating water vapor mixing ratio, based on the ME vertical distribution.

#### 5.2.6. *Sea-Level Pressure*

Figure 36 shows the MAE and ME versus time for model-simulated sea-level pressure for all ten experiments over the entire 4-km domain. The MAE generally increases with time through the period with the 30-h mean MAE varying from 0.93 hPa and 0.96 hPa for MM5 experiments MS11 and MS11KF to 1.26 hPa and 1.21 hPa for WRF experiments WS3 and WS3GR. The MM5 versus WRF comparison (Exps. MS12 and MS12KF versus WB2 and WB2KF) finds that MM5 MAE is 0.1 - 0.2 hPa smaller than that in WRF. The WRF experiments which have somewhat larger errors than MM5 show about 0.1 – 0.2 hPa smaller errors for those experiments including a CPS on the 4-km domain. The magnitude of the ME

also increases with time through the period and again the MM5 experiments have the lowest ME for sea-level pressure (Table 5). It is interesting that the MM5 experiments have a small negative bias while all the WRF experiments have a somewhat larger positive bias. All the 30-h ME values are less than 1.0 hPa.

## 6. CONCLUSIONS

### *6.1. Summary*

To further study how to improve 4-km mesoscale model simulations by building on lessons learned in Phase 1 of CRC A-46 project, ten new modeling experiments (four MM5 and six WRF) were designed and applied to a case study in this second phase of the project. Both subjective and objective evaluations have been performed on the model-simulated fields. Subjective evaluation again focused on the model-simulated precipitation field and the surface-layer winds, temperature and sea-level pressure at model hours 21 h (09 UTC September 19, 1983) and 30 h (18 UTC September 19, 1983). The 21-h time represented a night-time period when a mid-latitude frontal system was moving eastward across the northeast US on the 4-km domain, and the 30-h time was a day-time period when intense convective systems formed along the front and caused widespread distortion in the low-level wind flow and mass fields. Objective evaluation was performed by comparing the MAE and ME error distributions (over time at the surface vs. all vertical layers for the 30-h case period) of the model-simulated wind speed, wind direction, vector wind difference, temperature, water vapor mixing ratio and sea-level pressure for all ten model experiments. The conclusions drawn from this second phase of the research are summarized in this section.

Subjective evaluation showed that MM5 and WRF precipitation amounts were still too large on the 4-km domain likely due to grid-point storm issues. At the 21-h time, the maximum 3-h precipitation near the frontal system for each experiment was as follows (see Table 3): 57.6 mm for Exp. MS11 and 28.2 mm for Exp. MS11KF, 54.2 mm for Exp. MS12 and 46.3 mm in Exp. MS12KF, 33.6 mm in Exp. WB2 and 26.6mm in Exp. WB2KF, 20.5 mm in Exp. WS2 and

20.9 mm in Exp. WS2KF, and 29.5 mm in Exp. WS3 and 29.6 mm in Exp. WS3GR. At the 30-h time, the maximum 3-h precipitation near the frontal system for each experiment was the following: 38.0 mm in Exp. MS11 and 38.7mm in Exp. MS11KF, 69.8 mm in Exp. MS12 and 35.9 mm in Exp. MS12KF, 38.4 mm in Exp. WB2 and 31.3 mm in Exp. WB2KF, 12.8 mm in Exp. WS2 and 23.9 mm in Exp. WS2KF, 40.0 mm in Exp. WS3 and 33.8 mm in Exp. WS3GR. Thus precipitation was still overestimated by both models, but the amounts were generally reduced or not significantly increased in the experiments applying CPS directly on the 4-km domain.

Figure 37 summarizes the 4-km domain maximum 3-hourly precipitation for all ten experiments ending at 21 h and 30 h, and also the 30-h total maximum precipitation for each experiment. The observed precipitation within the 4-km model domain was generally less than 5 or 10 mm at both model analysis times, and the maximum total precipitation for any location within the 4-km domain was surely less than 20 – 25 mm (1 inch) while the total model-simulated maximum precipitation amounts ranged from 66.7 mm to 128 mm (Table 3). The figure shows that the maximum precipitation was generally reduced at all three ending times by applying a CPS on the 4-km domain. One possible exception was Exp. WS2 (WRF using the YSU PBL scheme) in which the precipitation coverage and intensities were increased at both the 21-h and 30-h times when the KF scheme was applied to the 4-km domain, but they were reduced for the 30-h total maximum.

In general, the WRF experiments had comparable or somewhat smaller precipitation amounts compared to those from the MM5, but they were all still too large. Thus although precipitation was still overestimated by both models, the amounts were generally reduced or not significantly increased in the experiments applying CPS directly on the 4-km domain.

MM5 and WRF precipitation patterns were quite different at the two analysis times despite their using the same model initial conditions and lateral boundary conditions, and very similar model physics. The location of the cold front and the intensity and distribution of the precipitation varied widely among the experiments due to different phase errors in the frontal positions, and the fact that FDDA was not used in either model in this study. A fair and direct comparison between MM5 and WRF was made based on Exps. MS12, MS12KF, WB2 and WB2KF. It was found that at the 21-h time, the precipitation in MM5 was more intense than that in WRF over the Lake Erie region. Precipitation in WRF was located more over the region to the northeast of Lake Ontario in Canada. Observed precipitation at this time was zero or very light. The model-simulated cold fronts were generally too slow for the northern / eastern end and too fast for the southern / western end. Those experiments that produced less rain to the south and west of Lake Huron also produced a better frontal location there. The cold frontal phase error, precipitation amounts and coverage, and the western (back) edge of the frontal precipitation were generally improved by using the CPS directly on the 4-km domain for most of the experiments except WRF WS2 using YSU PBL and WS3 using Grell CPS.

At the 30-h time, most of the precipitation in MM5 was located over Lake Erie and northern OH region, but it was located further north across the southern tip of Lake Huron or western NY in some WRF experiments. Use of the CPS on the 4-km domain improved the surface wind and temperature fields near Lake Erie at this time in MM5. The front in the WRF experiments was too slow and caused the precipitation at this time to occur further to the north and west than MM5 with southwesterly flow across Lake Erie where observed surface winds were from the northwest. The MM5 simulations, on the other hand, especially the one using KF CPS on the 4-km domain, reproduced the northwesterly flow over Lake Erie and the

southwesterly flow to the south of the front. When the precipitation amounts and coverage were reduced by adding the CPS on the 4-km domain, the surface cold pools and wind anomalies were also weakened.

It was shown that use of CPS on the 4-km domain in MM5 and WRF may mitigate some of the grid-point storm problems, especially when the spurious convection is very intense and causes anomalous low-level wind and mass fields, while at the same time either improving the simulations or at least not significantly changing the wind and mass fields (Tables 4-7 and Figs. 38 and 39). Use of a CPS on the 4-km domain may reduce the risk that a model produces strong grid point storm issues such as the occurrence of intense and unrealistic mesoscale convective systems (MCSs) as clearly seen in Phase 1 of the study. Use of a CPS directly on the 4-km domain showed some improvements in this study in both models in the mass and wind field statistical results, although the improvements were relatively small and may not be consistent over all layers and all variables.

Although there were no observations to verify the model-simulated PBL depths, a comparison of PBL depth among all ten experiments for both day-time and night-time periods indicated that the YSU PBL scheme gives a PBL depth that is artificially low (height of first full model layer, 32 m) at night time and likely too high during the day time with values comparable to those in MM5 using the MRF PBL (~950 m, see Stauffer and Deng 2004). Comparison between both TKE-based PBL schemes (GS PBL and Eta PBL) showed that the GS PBL scheme produced lower PBL depths at night time compared with the Eta PBL scheme, while during the day time, a cold bias at the surface in the Eta PBL experiments contributed to lower PBL depths compared to the other experiments.



Overall the MM5 and WRF statistical results for the wind and mass fields were generally comparable as shown in Tables 4-7 and Figs. 38 and 39, but some differences are noted. Comparison of the MAE score of model-simulated surface layer wind speed for all ten experiments indicated that the WRF experiment set using the YSU PBL scheme (WS2 and WS2KF) was the worst ( $\sim 2.4 - 2.5 \text{ ms}^{-1}$ ), and the WRF experiment set using M-Y-J Eta TKE PBL physics and either the KF or Grell CPS (WB2KF and WS3GR) was the best ( $1.8 - 1.9 \text{ ms}^{-1}$ ) (see Table 4 and Fig. 38). For wind speed over all layers, Table 6 and Fig. 39 show the MM5 experiment set using GS TKE PBL scheme and KF CPS was the worst ( $2.0 - 2.2 \text{ ms}^{-1}$ ) and the WRF experiments using M-Y-J TKE PBL were the best ( $1.7 - 1.9 \text{ ms}^{-1}$ ). Thus the difference between the worst and best experiments was only around  $0.3 \text{ ms}^{-1}$ . The best surface wind directions were produced by WB2KF but they were less than 1 degree better than the worst experiment (Table 4 and Fig. 38). For all layers, Table 6 and Fig. 39 show WRF had a slight advantage in wind direction by less than 1 degree. In general, the MAE and ME wind direction scores for all ten experiments were very similar, with the WRF experiment set using M-Y-J TKE PBL physics and Grell CPS and the MM5 experiment set using GS TKE PBL and KF CPS having slight advantage in the boundary layer.

Comparison of the MAE score of model-simulated temperature field (both surface layer and all layers) for all ten experiments indicated that the MM5 experiment set using GS TKE PBL (MS11 and MS11KF) was the best, and the WRF experiment set using M-Y-J TKE PBL physics and Grell CPS (WS3 and WS3GR) was the worst with around  $0.6 \text{ }^{\circ}\text{C}$  larger errors at the surface and  $0.2 \text{ }^{\circ}\text{C}$  larger errors over all layers (Tables 4 and 6, Figs. 38 and 39). Similarly, the MM5 experiment sets MS11 and MS12 produced the best sea-level pressure statistics ( $\sim 0.9 - 1.0 \text{ hPa}$ ) while the WS3 experiments produced the worst sea-level pressure scores by about  $0.3 \text{ hPa}$ . For

the model-simulated surface layer water vapor mixing ratio field, the MM5 MS11 experiment set using GS TKE PBL and KF CPS was the best by about  $0.1 \text{ g kg}^{-1}$  (Table 4 and Fig. 38). For all layers, the WRF WS2 experiment set using YSU PBL scheme produced slightly smaller errors ( $0.1 - 0.2 \text{ g kg}^{-1}$ ) in vapor mixing ratio than the other experiments (Table 6 and Fig. 39).

A direct and fair comparison between the MM5 and WRF models was made using Exps. MS12, MS12KF, WB2 and WB2KF. It was found that WRF appears to have somewhat better performance in the wind speed field ( $0.1 - 0.2 \text{ ms}^{-1}$ ), and wind direction differences between MM5 and WRF were less than 1 degree in magnitude on average (Tables 4 and 6, Figs. 38 and 39). For the model-simulated temperature field, both models had very similar scores, with MM5 being slightly better overall by about  $0.1 \text{ }^{\circ}\text{C}$  with MM5 being better in some model layers and WRF being better in some other layers. For moisture, WRF was slightly better than MM5 over all layers by about  $0.1 \text{ g kg}^{-1}$ . Again, the statistical differences between these two models without FDDA were relatively small and suggest that there was no clear advantage of one model over the other for this case. WRF was slightly better in the wind fields and slightly worse in the mass fields. The Eta PBL had an advantage in simulating wind speed compared to GS PBL but the mass fields were much better simulated by the GS PBL. The YSU PBL (Exps. WS2 and WS2KF) produced the worst wind statistics at the surface and appeared to over smooth the surface horizontal wind fields compared to the other experiments.

## 6.2 *Limitations of the Study and Future Work*

However, it must be pointed out that this is only one case study, but this case is representative of mid-latitude frontal rain and deep convection cases, so these results should be

generally representative of other cases. Additional cases are still needed to determine the general added value of this research.

Note that use of a convective sub-grid physics scheme at 4-km resolution for deep (precipitating) convection violates the underlying assumption that the size of the updraft being parameterized is much smaller than the grid size. It is also clear that in general, explicit microphysics alone cannot completely represent deep convection on these 4-km grid scales and some type of parameterization is needed. Since there is no readily identifiable approach to do this, this presents a serious dilemma when using 4-km grids to simulate deep convective environments. The results presented here show that use a CPS on the 4-km grid may still be helpful in these situations where 4-km resolution is desired and explicit microphysics alone produces grossly unrealistic precipitation amounts.

The results produced from this research continue to point to our need for development of a new CPS appropriate for application on these very fine scales which are still too coarse for purely resolved-scale explicit-moisture approaches. It is possible that application of an existing CPS on these finer scales may mitigate some of the grid-point storm problems, especially when the spurious convection is very intense and causes anomalous low-level wind flows. Application of a CPS on the 4-km domain causing a slight degradation in the model solution in some layers and in some fields may still be acceptable if it minimizes the potentially significant damage caused by an otherwise intense grid-point storm. Further experimentation with higher resolution models with grid lengths of say 1 – 2 km, where explicit-only approaches would be more valid, should be done for direct comparison with these 4-km results in a future study. There are other issues, however, with model physics as grid lengths approach 1 km such as using 1D versus 3D turbulence schemes, etc.

It has been proven in Phase 1 of this project that FDDA can significantly reduce the model errors. It is extremely important to revisit this subject in WRF in the future. However, WRF does not currently have a FDDA capability to nudge the model solutions to either gridded analysis fields or to individual observations. Thus, the recommendations to CRC for future work based on this research should include development of a nudging capability in WRF, in addition to development of shallow/deep cumulus parameterization scheme suitable for 4-km resolution modeling.

## Appendix: A List of Statistical Measures Used in This Study

1). Mean Error ( $ME$ )

$$ME = \left[ \sum_{n=1}^N (\alpha_n - \alpha_n^O) \right] / N \quad (1)$$

2). Mean Absolute Error ( $MAE$ )

$$MAE = \left[ \sum_{n=1}^N |\alpha_n - \alpha_n^O| \right] / N \quad (2)$$

3). Index of agreement ( $I$ ) (Willmott 1982, Willmott et al. 1985).

$$I = 1 - \left[ \sum_{n=1}^N (\alpha_n - \alpha_n^O)^2 / \sum_{n=1}^N (|\alpha_n'| + |\alpha_n'^O|)^2 \right], \quad 0 \leq I \leq 1 \quad (3)$$

Note, for (1) and (2)  $\alpha_n^O$  is the  $n^{th}$  observation of some scalar variable  $\alpha$ ,  $N$  is the total number of observations on the verification domain, and  $\alpha_n$  is the model field for variable  $\alpha$  interpolated to the observation site. For (3),  $\alpha_n' = (\alpha_n - \bar{\alpha})$ ,  $\alpha_n'^O = (\alpha_n^O - \bar{\alpha})$ , and  $\bar{\alpha}$  is the mean of the observed wind speed on the verification domain.

## REFERENCES

- Arakawa, A., and V.R. Lamb, 1977: Computational design of the basic dynamical process of the UCLA general circulation model. *Methods in Comp. Physics*, **17**, 173-265.
- Beljaars, A.C.M., 1994: The parameterization of surface fluxes in large-scale models under free convection, *Quart. J. Roy. Meteor. Soc.*, **121**, 255–270.
- Benjamin, S.G. and N.L. Seaman, 1985: A Simple Scheme for Objective Analysis in Curved Flow. *Mon. Wea. Rev.*, **113**, 1184-1198.
- Deng, A, N.L. Seaman and J.S. Kain, 2003: A shallow-convection parameterization for mesoscale models Part I: Sub-model description and preliminary applications. *J. Atmos. Sci.*, **60**, 34-56.
- Deng, A., N. L. Seaman, G. K. Hunter and D. R. Stauffer, 2004: Evaluation of interregional transport using the MM5-SCIPUFF system. *J. Appl. Meteor.*, **43**, 1864-1886.
- Deng, A, and D. R. Stauffer, 2006: On improving 4-km mesoscale model simulations. Accepted for publication in *J. Appl. Meteor.*, 27 pp.
- Dudhia, J., 1989: Numerical study of convection observed during the Winter Monsoon Experiment using a mesoscale two-dimensional model. *J. Atmos. Sci.*, **46**, 3077-3107.
- Dudhia, J., 1993: A nonhydrostatic version of the Penn State/NCAR mesoscale model: Validation tests and simulation of an Atlantic cyclone and cold front. *Mon. Wea. Rev.*, **121**, 1493-1513.
- Dyer, A. J., and B. B. Hicks, 1970: Flux-gradient relationships in the constant flux layer, *Quart. J. Roy. Meteor. Soc.*, **96**, 715–721.
- Gayno, G.A., N.L. Seaman, A.M. Lario, and D.R. Stauffer, 1994: Forecasting visibility using a 1.5-order closure boundary layer scheme in a 12-km non-hydrostatic model. 10<sup>th</sup> AMS Conf. on Num. Wea. Pred., Portland, OR, 18-22 July, 18-20.
- Grell, G. A., J. Dudhia and D. R. Stauffer, 1994: A description of the fifth generation Penn State/NCAR mesoscale model (MM5). NCAR Tech. Note NCAR/TN-398+STR, 138 pp. [Available from NCAR Information Support Services, P.O. Box 3000, Boulder, CO 80397]
- Grell, G. A., and D. Devenyi, 2002: A generalized approach to parameterizing convection combining ensemble and data assimilation techniques. *Geophys. Res. Lett.*, **29(14)**, Article 1693.
- Hong, S.-Y., H.-L. Pan, 1996: Nonlocal boundary vertical diffusion in a medium-range forecast model. *Mon. Wea. Rev.*, **124**, 2322-2339

- Hong, S.-Y., H.-M. H. Juang, and Q. Zhao, 1998: Implementation of prognostic cloud scheme for a regional spectral model, *Mon. Wea. Rev.*, **126**, 2621–2639.
- Hong, S.-Y., J. Dudhia, and S.-H. Chen, 2004: A Revised approach to ice microphysical processes for the bulk parameterization of clouds and precipitation, *Mon. Wea. Rev.*, **132**, 103–120.
- Janjic, Z. I., 1990: The step-mountain coordinate: physical package, *Mon. Wea. Rev.*, **118**, 1429–1443.
- Janjic, Z. I., 1994: The step-mountain eta coordinate model: further developments of the convection, viscous sublayer and turbulence closure schemes, *Mon. Wea. Rev.*, **122**, 927–945.
- Janjic, Z. I., 1996: The surface layer in the NCEP Eta Model, Eleventh Conference on Numerical Weather Prediction, Norfolk, VA, 19–23 August; Amer. Meteor. Soc., Boston, MA, 354–355.
- Janjic, Z. I., 2002: Nonsingular Implementation of the Mellor–Yamada Level 2.5 Scheme in the NCEP Meso model, NCEP Office Note, No. 437, 61 pp.
- Kain, J. S. and J. M. Fritsch, 1990: A one-dimensional entraining/detraining plume model and its application in convective parameterization. *J. Atmos. Sci.*, **47**, 2784–2802.
- Kain, J.S. and J.M. Fritsch, 1993: Convective parameterization for mesoscale models: The Kain-Fritsch scheme. The Representation of cumulus in numerical models. K. A. Emanuel and D. J. Raymond, eds, Meteorological Monographs. Amer. Meteor. Soc., 165-170.
- Kain, J. S., 2004: The Kain-Fritsch convective parameterization: An update. *J. Appl. Meteor.*, **43**, 170–181.
- Klemp, J.B., W.C. Skamarock and O. Fuhrer, 2003: Numerical consistency of metric terms in terrain-following coordinates. *Mon. Wea. Rev.* **131**, 1229–1239.
- Lacis, A. A., and J. E. Hansen, 1974: A parameterization for the absorption of solar radiation in the earth's atmosphere. *J. Atmos. Sci.*, **31**, 118–133.
- Laprise, R., 1992: The Euler equations of motion with hydrostatic pressure as an independent variable. *Mon. Wea. Rev.*, **120**, 197-207.
- Lyons, W. A., C. J. Tremback, and R. A. Pielke, 1995: Applications of the Regional Atmospheric Modeling System (RAMS) to provide input to photochemical grid models for the Lake Michigan Ozone Study (LMOS). *J. Appl. Meteor.*, **34**, 1762-1784.

- Mellor, G. L., and T. Yamada, 1982: Development of a turbulence closure model for geophysical fluid problems. *Rev. Geophys. Space Phys.*, **20**, 851–875.
- Mlawer, E. J., S. J. Taubman, P. D. Brown, M. J. Iacono, and S. A. Clough, 1997: Radiative transfer for inhomogeneous atmosphere: RRTM, a validated correlated-k model for the longwave. *J. of Geophys. Res.*, **102** (D14), 16663-16682.
- Moeng, C.-H., and J.C. Wyngaard, 1989: Evaluation of turbulent transport and dissipation closures in second-order modeling. *J. Atmos. Sci.*, **46**, 2311-2330.
- Monin, A.S. and A.M. Obukhov, 1954: Basic laws of turbulent mixing in the surface layer of the atmosphere. *Contrib. Geophys. Inst. Acad. Sci., USSR*, (151), 163–187.
- Paulson, C. A., 1970: The mathematical representation of wind speed and temperature profiles in the unstable atmospheric surface layer. *J. Appl. Meteor.*, **9**, 857–861.
- Reisner, J., R. M. Rasmussen, and R. T. Brintjes, 1998: Explicit forecasting of supercooled liquid water in winter storms using the MM5 mesoscale model. *Quart. J. Roy. Meteor. Soc.*, **124** B, 1071-1107.
- Seaman, N.L., D.R. Stauffer and A.M. Lario-Gibbs, 1995: A multi-scale four-dimensional data assimilation system applied in the San Joaquin valley during SARMAP: Part I: Modeling design and basic performance characteristics. *J. Appl. Meteor.*, **34**, 1739-1761.
- Seaman, N. L., A. Deng, G. K. Hunter and D. R. Stauffer, 2002: Evaluation of a regional model for interregional transport. Final report for CRC Contract No. A-28. 216 pp.
- Shafran, P.C., N.L. Seaman and G.A. Gayno, 2000: Evaluation of Numerical Predictions of Boundary-Layer Structure during the Lake Michigan Ozone Study (LMOS). *J. Appl. Meteor.*, **39**, 412-426.
- Skamarock, W. J. B. Klemp, J. Dudhia, D. O. Gill, D. M. Barker, W. Wang and J. G. Powers, 2005: A description of the Advanced Research WRF Version2. NCAR Tech. Note NCAR/TN-468+STR, 88 pp. [Available from NCAR Mesoscale and Microscale Meteorology Division, Boulder, CO 80397]
- Smagorinsky, J., S. Manabe and J.L. Holloway, Jr., 1965: Numerical results from a nine-level general circulation model of the atmosphere. *Mon. Wea. Rev.*, **93**, 727-768.
- Stauffer, D. R., and A. Deng, 2004: Improving fine grid meteorological simulations for air quality applications. Phase 1 final report for CRC Contract No. A-46, 179 pp.
- Stauffer, D.R., R.C. Munoz, and N.L. Seaman, 1999: In-cloud turbulence and explicit microphysics in the MM5. 9<sup>th</sup> PSU/NCAR Mesoscale Model Users' Workshop. Boulder, CO, 23-25 June, 177-180.



- Stephens, G. L., 1978: Radiation profiles in extended water clouds. Part II: Parameterization schemes, *J. Atmos. Sci.*, **35**, 2123–2132.
- Webb, E. K., 1970: Profile relationships: The log-linear range, and extension to strong stability, *Quart. J. Roy. Meteor. Soc.*, **96**, 67–90.
- Wicker, L.J. and W.C. Skamarock, 2002: Time-splitting methods for elastic models using forward time schemes. *Mon. Wea. Rev.*, **130**, 2088–2097.
- Willmott, C.J., 1982: Some comments on the evaluation of model performance. *Bull. Amer. Meteor. Soc.*, **63**, 1309–1313.
- Willmott, C.J., S.G. Ackleson, R.E. Davis, J.J. Feddema, K.M. Klink, D.R. Legates, J. O'Donnell, and C.M. Rowe, 1985: Statistics for the evaluation and comparison of models. *J. of Geophys. Res.*, **90**, 8995–9005.
- Zhang, D.-L., and R.A. Anthes, 1982: A high-resolution model of the planetary boundary layer—sensitivity tests and comparisons with SESAME–79 data. *J. Appl. Meteor.*, **21**, 1594–1609.
- Zilitinkevich, S. S., 1995: Non-local turbulent transport: pollution dispersion aspects of coherent structure of convective flows, *Air Pollution III — Volume I. Air Pollution Theory and Simulation*, Eds. H. Power, N. Moussiopoulos and C.A. Brebbia. Computational Mechanics Publications, Southampton Boston, 53–60.

Table 1. Vertical distribution of  $\sigma$  (MM5) or  $\eta$  (WRF) levels (half layers) and model-layer heights (m AGL) in MM5 for all four domains. Model layer vertical indexing is reversed in WRF (not shown,  $k = 1$  for the surface layer) and the model layer heights in WRF (not shown) are generally similar to those in MM5 but vary in time.

Layer	$\sigma$ or $\eta$	MM5 Height (m)
32	0.996	28.9
31	0.988	85.9
30	0.980	143.3
29	0.972	201.0
28	0.964	259.0
27	0.955	324.7
26	0.945	398.3
25	0.935	472.4
24	0.925	547.0
23	0.915	622.3
22	0.900	736.3
21	0.880	890.4
20	0.860	1047.1
19	0.840	1206.4
18	0.820	1368.3
17	0.800	1533.1
16	0.780	1700.8
15	0.760	1871.6
14	0.730	2133.7
13	0.690	2494.9
12	0.650	2870.8
11	0.610	3262.7
10	0.570	3672.1
9	0.525	4156.0
8	0.475	4726.1
7	0.425	5335.4
6	0.375	5990.3
5	0.325	6699.2
4	0.275	7472.8
3	0.225	8325.9
2	0.150	9802.3
1	0.050	12347.4

Table 2. Summary of experimental design. M\_\_ = MM5 W\_\_ = WRF. Gray shading identifies those experiments used in the direct comparison between MM5 and WRF.

Exp. No.	Exp. Name	PBL Physics	Microphysics	CPS	Radiation	FDDA
0	WB1 (prelim. version)	M-Y-J Eta TKE PBL	WSM 3-class simple ice scheme	None	LW: RRTM SW: Dudhia	None
1	MS11	GS TKE PBL	Simple ice	None	LW: RRTM SW: Dudhia	None
2	MS11KF	GS TKE PBL	Simple ice	KF	LW: RRTM SW: Dudhia	None
3	MS12	Eta M-Y PBL	Simple Ice	None	LW: RRTM SW: Dudhia	None
4	WB2	M-Y-J Eta TKE PBL	WSM 3-class simple ice scheme	None	LW: RRTM SW: Dudhia	None
5	MS12KF	Eta M-Y PBL	Simple Ice	KF	LW: RRTM SW: Dudhia	None
6	WB2KF	M-Y-J Eta TKE PBL	WSM 3-class simple ice scheme	KF	LW: RRTM SW: Dudhia	None
7	WS2	YSU PBL	WSM 3-class simple ice scheme	None	LW: RRTM SW: Dudhia	None
8	WS2KF	YSU PBL	WSM 3-class simple ice scheme	KF	LW: RRTM SW: Dudhia	None
9	WS3	M-Y-J Eta TKE PBL	WSM 3-class simple ice scheme	None	LW: RRTM SW: Dudhia	None
10	WS3GR	M-Y-J Eta TKE PBL	WSM 3-class simple ice scheme	Grell	LW: RRTM SW: Dudhia	None

Table 3. Maximum model-simulated precipitation amounts (mm) on the 4-km domain for all experiments for the 3-hour periods ending at 21 hours (0900 UTC 19 September 1983), and 30 hours (1800 UTC 19 September 1983), and the maximum total accumulated precipitation through the entire 30-hour period. These maximum values are computed from the sum of the parameterized subgrid precipitation (if a CPS is used) and the grid-resolved (explicit) precipitation for each model experiment.

<b>Exp. Name</b>	<b>18-21 hours</b>	<b>27-30 hours</b>	<b>0-30 hours</b>
MS11	57.6	38.0	128.0
MS11KF	28.2	38.7	92.6
MS12	54.2	69.8	121.0
MS12KF	46.3	35.9	79.1
WB2	33.6	38.4	69.1
WB2KF	26.6	31.3	76.9
WS2	20.5	12.8	73.3
WS2KF	20.9	23.9	66.7
WS3	29.5	40.0	101.0
WS3GR	29.6	33.8	98.1

Table 4. Thirty-hour mean of the mean absolute error of the model-simulated surface-layer fields and sea level pressure (SLP). Bold values show the better entry between each no-CPS and CPS experiment pair, underlined values denote the best value within each CPS-experiment set and each no-CPS experiment set, and the asterisks indicate the best value over all experiments for each variable.

Exp. Name	Wind Speed (ms <sup>-1</sup> )	Wind Direction (deg)	Vector Wind Difference (ms <sup>-1</sup> )	Temperature (°C)	Water Vapor Mixing Ratio (g kg <sup>-1</sup> )	SLP (hPa)
MS11	<b>2.31</b>	31.69	<b>3.35</b>	<u>1.82</u>	<b><u>1.30*</u></b>	<b><u>0.93*</u></b>
MS11KF	2.50	<b>31.31</b>	3.51	<b><u>1.76*</u></b>	<u>1.31</u>	<u>0.96</u>
MS12	<b>2.03</b>	<u>31.18</u>	<b>3.13</b>	2.31	<b>1.46</b>	<b>0.99</b>
MS12KF	2.10	<b>30.72</b>	3.19	<b>2.27</b>	<b>1.46</b>	1.00
WB2	<u>1.86</u>	31.35	<u>2.98</u>	2.36	1.35	1.18
WB2KF	<b><u>1.84*</u></b>	<b><u>30.62*</u></b>	<b><u>2.95*</u></b>	<b>2.32</b>	<b>1.34</b>	<b>1.09</b>
WS2	<b>2.43</b>	<b>31.70</b>	<b>3.59</b>	1.88	1.35	1.11
WS2KF	2.49	31.89	3.66	<b>1.86</b>	<b>1.33</b>	<b>1.03</b>
WS3	1.87	<b>31.19</b>	3.02	<b>2.34</b>	<b>1.38</b>	1.26
WS3GR	<b><u>1.84*</u></b>	31.34	<b>2.99</b>	2.38	1.40	<b>1.21</b>

Table 5. Thirty-hour mean of the mean error of the model-simulated surface-layer fields and sea level pressure (SLP), and index of agreement of the model-simulated wind speed. Bold values show the better entry between each no-CPS and CPS experiment pair, underlined values denote the best value within each CPS-experiment set and each no-CPS experiment set, and the asterisks indicate the best value over all experiments for each variable.

Exp. Name	Wind Speed ( $\text{ms}^{-1}$ )	Wind Direction (deg)	Index of Agreement (fraction)	Temperature ( $^{\circ}\text{C}$ )	Water Vapor Mixing Ratio ( $\text{g kg}^{-1}$ )	SLP (hPa)
MS11	<b>1.37</b>	<b>-0.08</b>	<b>0.66</b>	-0.42	0.29	<b>-0.27</b>
MS11KF	1.66	3.33	0.65	<b>-0.28</b>	<b><u>0.14*</u></b>	-0.41
MS12	<b>1.35</b>	<b>2.22</b>	<b>0.69</b>	-1.35	0.82	<b><u>-0.15*</u></b>
MS12KF	1.44	2.52	<b>0.69</b>	<b>-1.29</b>	<b>0.81</b>	<b><u>-0.28</u></b>
WB2	<b><u>1.08*</u></b>	<u>-0.07</u>	<u>0.71</u>	-1.09	0.50	0.80
WB2KF	1.09	<b><u>-0.04*</u></b>	<b><u>0.72*</u></b>	<b>-1.06</b>	<b>0.50</b>	<b>0.68</b>
WS2	<b>1.88</b>	<b>7.05</b>	<b>0.65</b>	<u>-0.04</u>	<b><u>-0.28</u></b>	0.65
WS2KF	1.96	7.70	0.64	<b><u>-0.03*</u></b>	-0.30	<b>0.53</b>
WS3	1.12	1.78	0.70	<b>-1.04</b>	<b>0.58</b>	0.92
WS3GR	<b><u>1.08*</u></b>	<b>0.84</b>	<b>0.71</b>	-1.11	0.63	<b>0.83</b>

Table 6. Thirty-hour mean of the mean absolute error of the model-simulated profile (32-layer) fields. Bold values show the better entry between each no-CPS and CPS experiment pair, underlined values denote the best value within each CPS-experiment set and each no-CPS experiment set, and the asterisks indicate the best value over all experiments for each variable.

Exp. Name	Wind Speed ( $\text{ms}^{-1}$ )	Wind Direction (deg)	Vector Wind Difference ( $\text{ms}^{-1}$ )	Temperature ( $^{\circ}\text{C}$ )	Water Vapor Mixing Ratio ( $\text{g kg}^{-1}$ )
MS11	2.17	<b>11.24</b>	3.34	<u>0.85</u>	0.78
MS11KF	<b>2.02</b>	11.44	<b>3.25</b>	<b><u>0.84*</u></b>	<b>0.76</b>
MS12	1.95	<b>11.63</b>	<b>3.22</b>	0.97	0.92
MS12KF	<b>1.94</b>	11.64	<b>3.22</b>	<b>0.93</b>	<b>0.87</b>
WB2	<b>1.87</b>	10.75	<b>2.98</b>	1.00	0.78
WB2KF	1.89	<b>10.65</b>	2.99	<b>0.96</b>	<b>0.77</b>
WS2	<b>1.85</b>	<b>10.36</b>	<b>2.88</b>	0.88	<u>0.66</u>
WS2KF	1.89	10.78	2.92	<b>0.86</b>	<b><u>0.64*</u></b>
WS3	<b><u>1.72*</u></b>	<b><u>9.53*</u></b>	<b><u>2.74*</u></b>	<b>1.02</b>	<b>0.73</b>
WS3GR	<b><u>1.72*</u></b>	<u>9.76</u>	<u>2.75</u>	1.05	0.74

Table 7. Thirty-hour mean of the mean error of the model-simulated profile (32-layer) fields and index of agreement of the model-simulated wind speed profile. Bold values show the better entry between each no-CPS and CPS experiment pair, underlined values denote the best value within each CPS-experiment set and each no-CPS experiment set, and the asterisks indicate the best value over all experiments for each variable.

Exp. Name	Wind Speed ( $\text{ms}^{-1}$ )	Wind Direction (deg)	Index of Agreement (fraction)	Temperature ( $^{\circ}\text{C}$ )	Water Vapor Mixing Ratio ( $\text{g kg}^{-1}$ )
MS11	0.49	<b>-1.23</b>	0.89	<u><b>-0.00*</b></u>	0.12
MS11KF	<b>0.46</b>	-2.09	<b>0.91</b>	0.04	<b>0.09</b>
MS12	<b>0.41</b>	<b>-1.74</b>	<b>0.91</b>	-0.22	0.23
MS12KF	0.42	-2.26	<b>0.91</b>	<b>-0.18</b>	<b>0.20</b>
WB2	<b>-0.30</b>	<b>-0.88</b>	<b>0.90</b>	-0.03	0.18
WB2KF	-0.31	-0.92	<b>0.90</b>	<u><b>-0.00*</b></u>	<b>0.16</b>
WS2	-0.54	<u>-0.12</u>	<b>0.90</b>	<b>0.17</b>	<u><b>-0.00*</b></u>
WS2KF	<b>-0.50</b>	<u><b>-0.05*</b></u>	<b>0.90</b>	<b>0.17</b>	<u>-0.05</u>
WS3	<u>-0.22</u>	<b>-1.44</b>	<u>0.92</u>	<b>-0.09</b>	<b>0.14</b>
WS3GR	<u><b>-0.11*</b></u>	-1.55	<u><b>0.93*</b></u>	-0.13	0.18



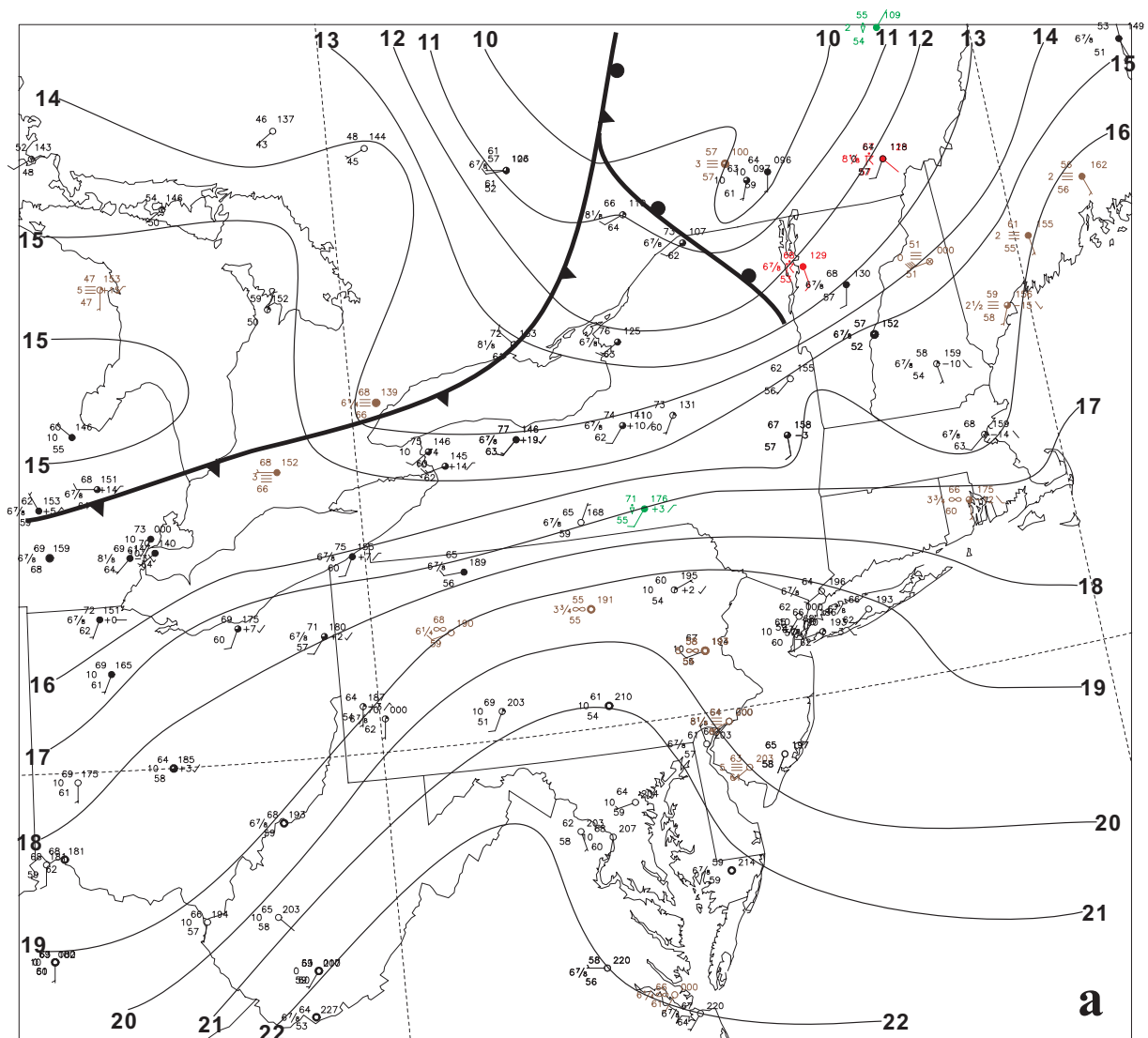


Figure 1 Standard surface weather analysis at a) 0900 UTC 19 September 1983, b) 1800 UTC 19 September 1983. Sea-level pressure contour interval is 1 hPa. One barb is  $5 \text{ m s}^{-1}$ . A color-coded station model is used for quick identification of current weather categories: Green symbols indicate reports of rain or showers, blue symbols represent frozen precipitation, red symbols denote thunderstorms, pink symbols indicate a thunderstorm nearby but not overhead, brown symbols represent obstructions to visibility (fog, haze) and black symbols indicate no significant weather.

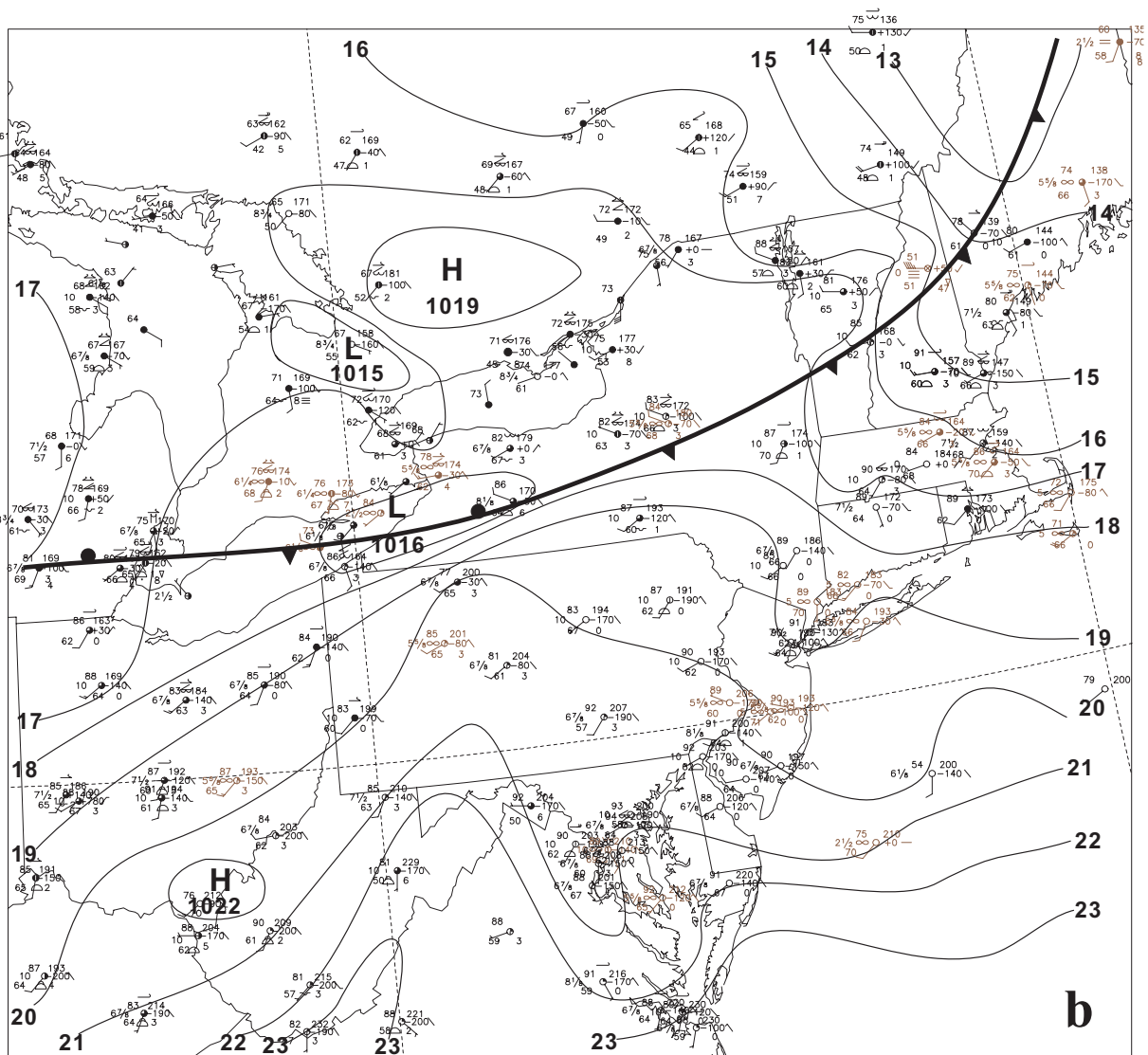


Figure 1 (Continued)

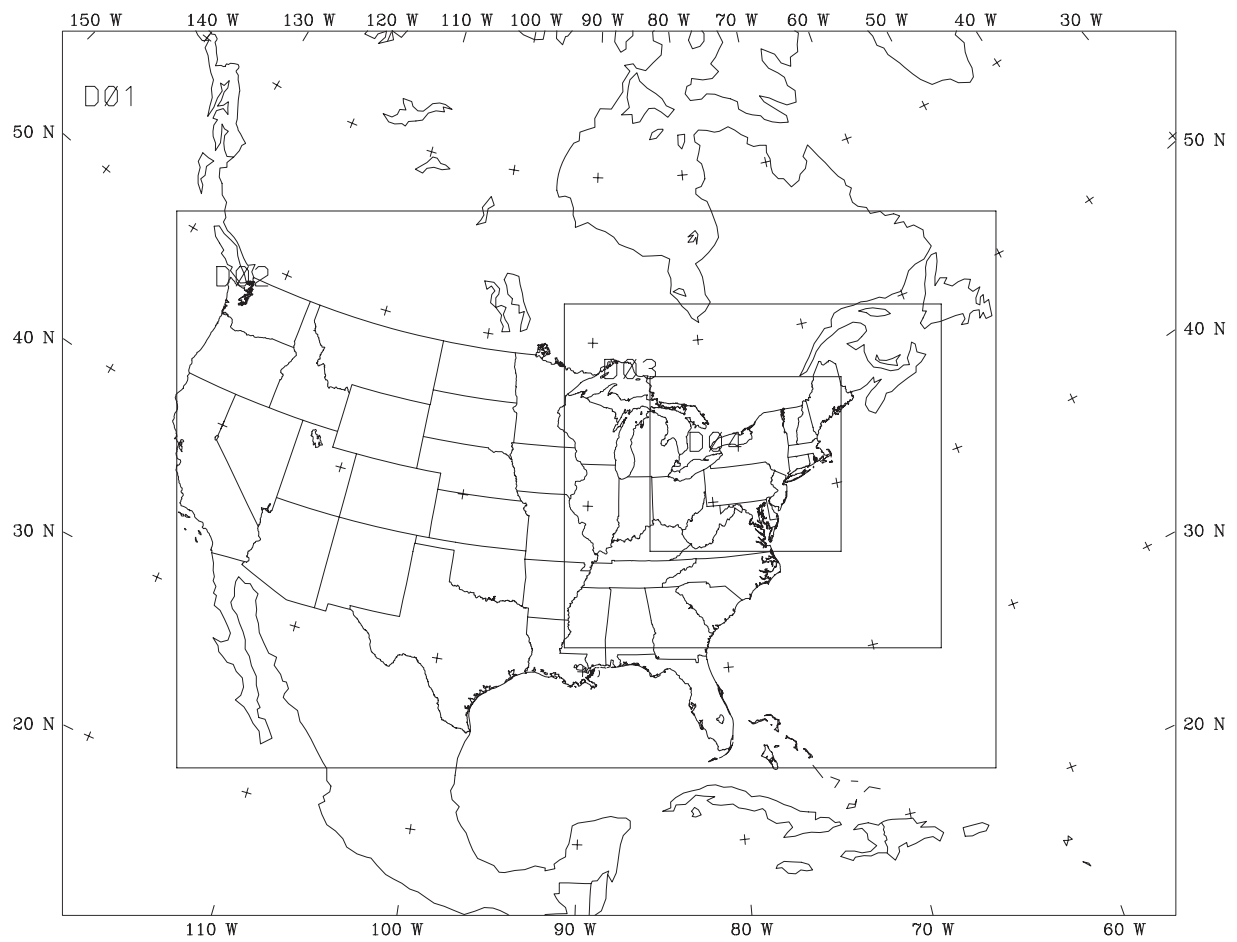


Figure 2 Location of 108-km, 36-km, 12-km and 4-km nested domains for MM5 and WRF experiments.

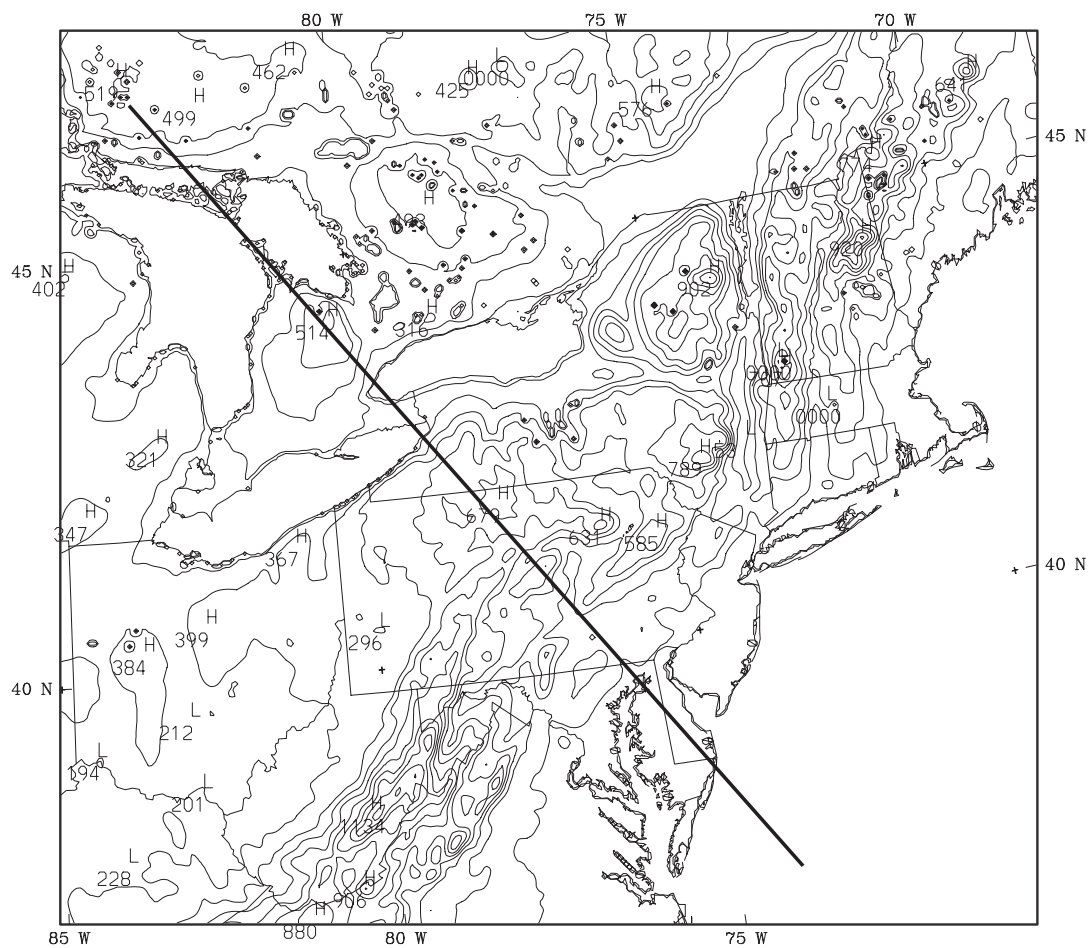
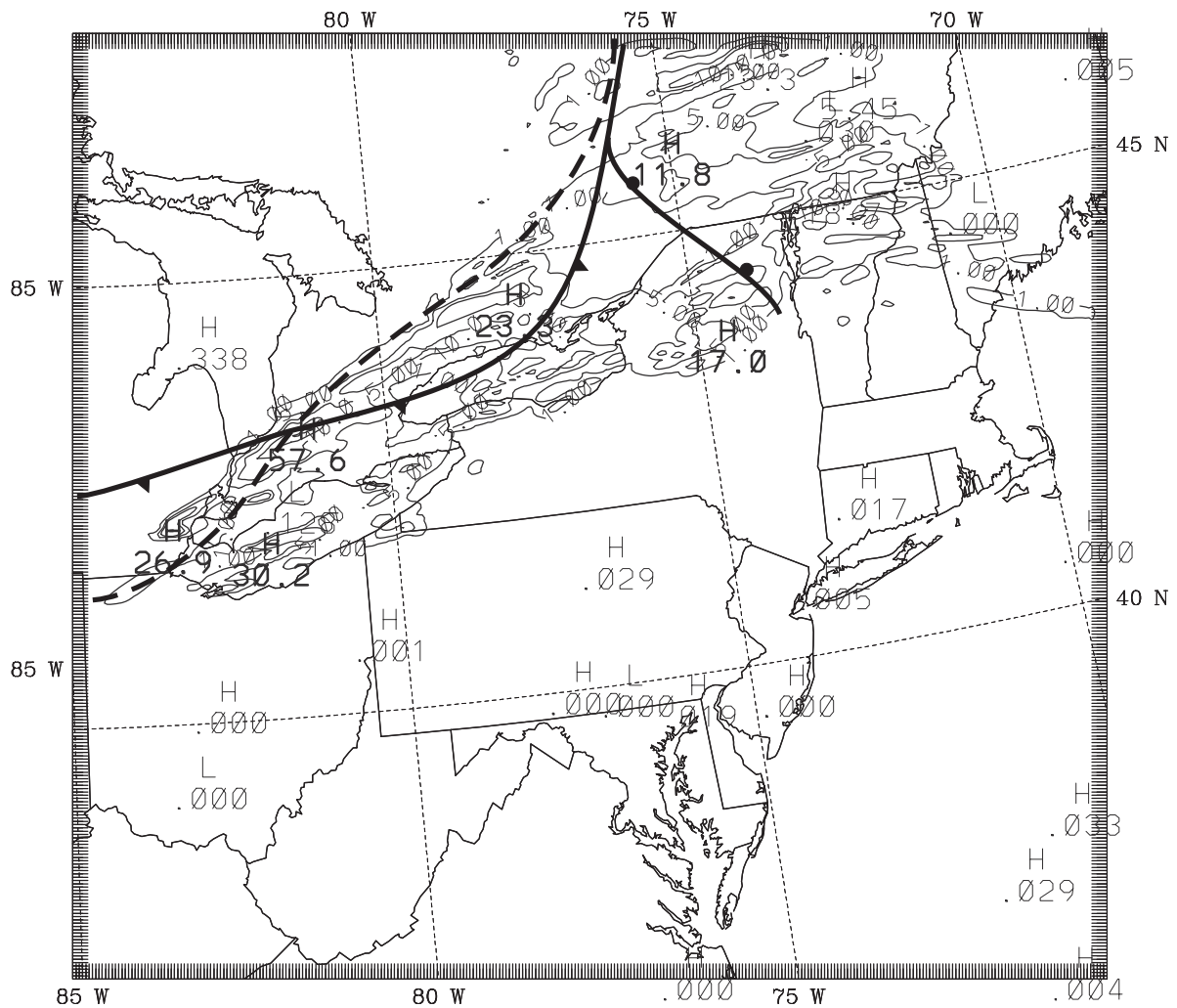


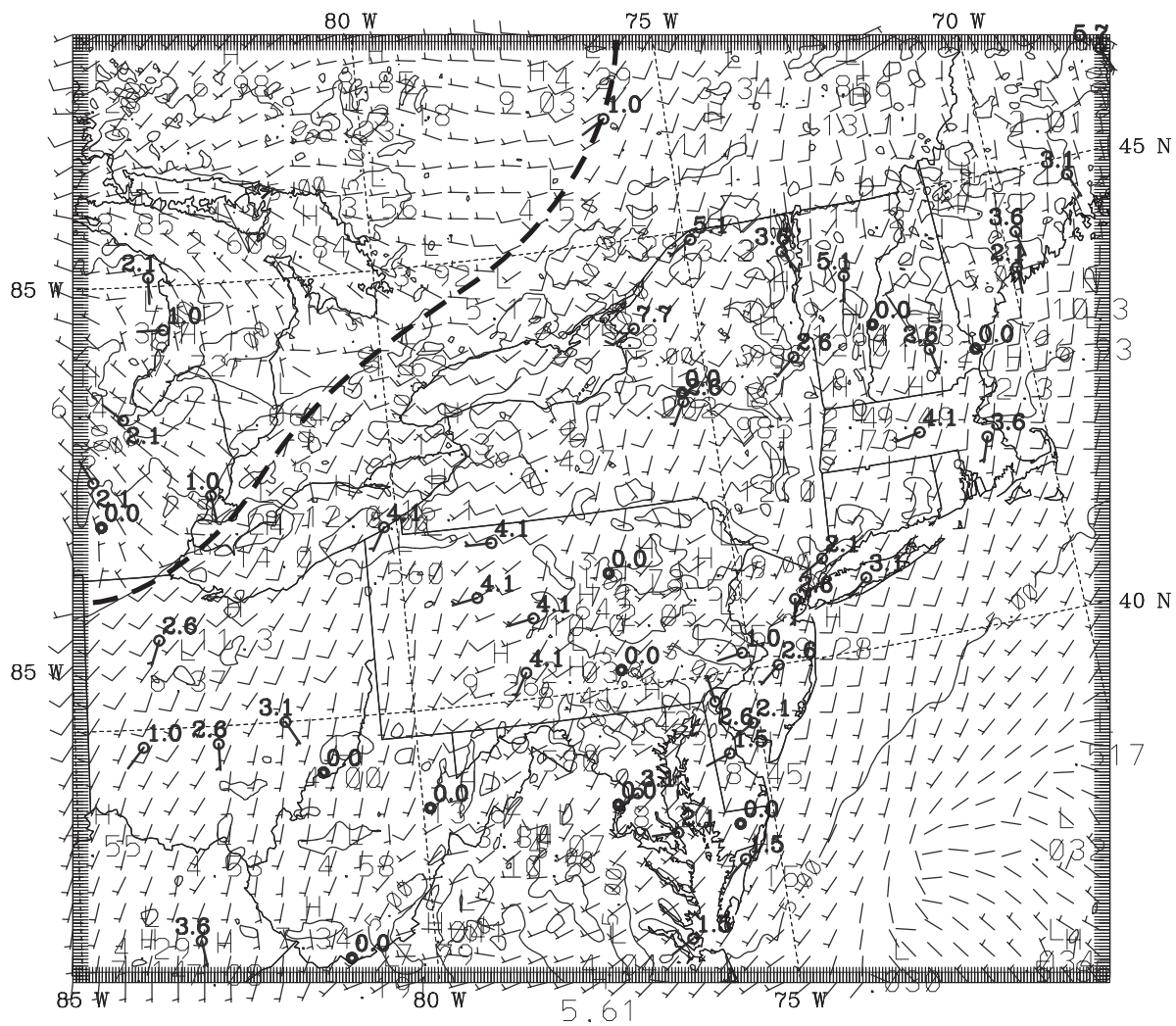
Figure 3      Terrain (m) for the MM5 and WRF 4-km domains. Contour interval is 100 m. The solid line marks the location of the cross section used in Figs. 14 and 25.



MM5V3-CAPTEX MS11, 4km, no CPS, No FDDA

a)

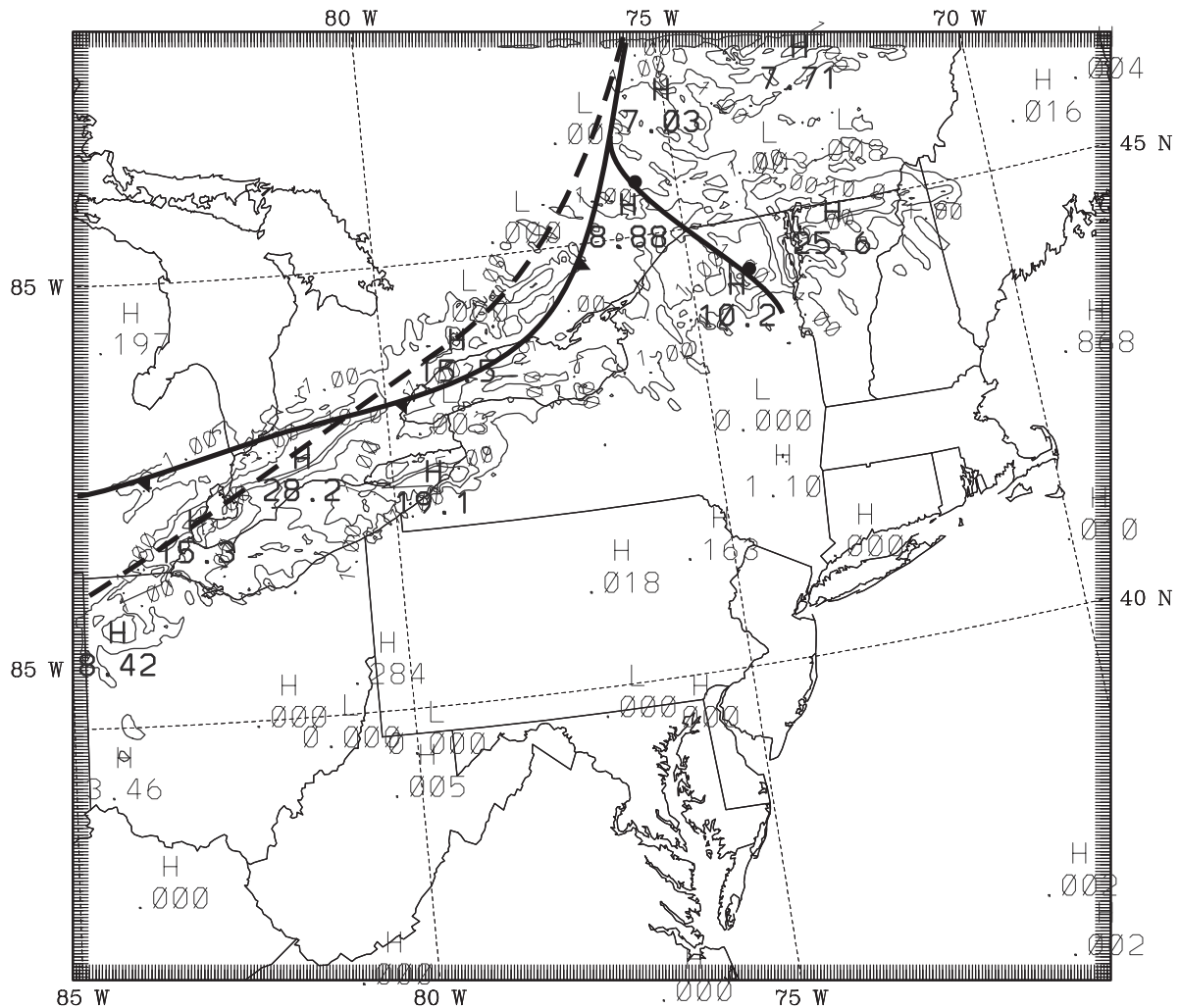
Figure 4 Model-simulated fields at 21 h (0900 UTC 19 September 1983) on the 4-km domain in Exp. MS11, (a) 3-h total precipitation (mm), (b) Surface-layer wind overlaid with observed surface winds ( $\text{ms}^{-1}$ ). Rain contours are 1, 5, 10 and 25 mm, speed contours are  $5 \text{ ms}^{-1}$  and one barb is  $10 \text{ ms}^{-1}$ . Observed surface front is depicted using traditional frontal symbols and model-simulated front is shown with heavy dashed line.



b)

Figure 4 (Continued)





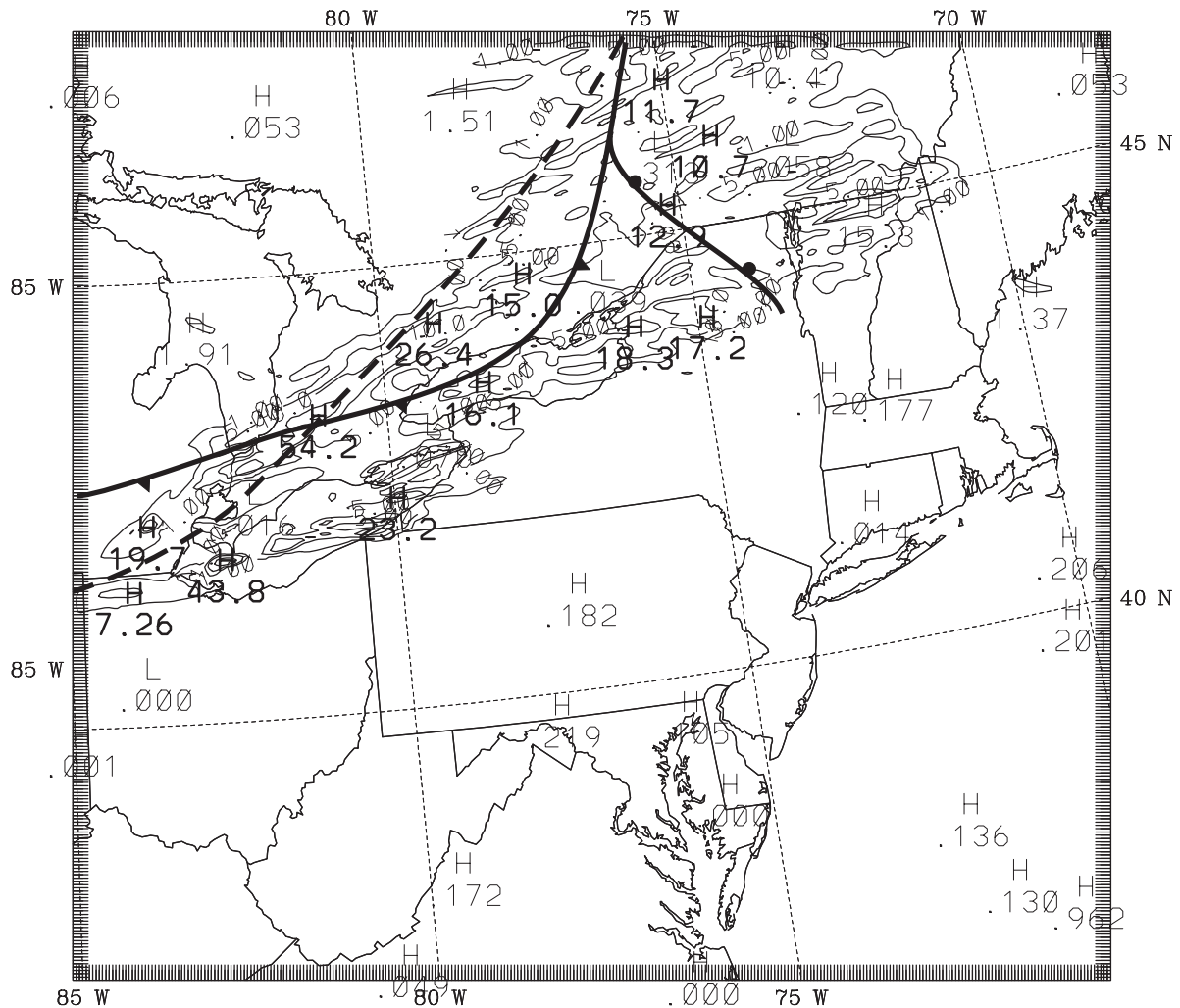
MM5V3-CAPTEX MS11KF, 4km, KF2, No FDDA

a)

Figure 5 Model-simulated fields at 21 h (0900 UTC 19 September 1983) on the 4-km domain in Exp. MS11KF, (a) 3-h total precipitation (mm), (b) Surface-layer wind overlaid with observed surface winds ( $\text{ms}^{-1}$ ). Rain contours are 1, 5, 10 and 25 mm, speed contours are  $5 \text{ ms}^{-1}$  and one barb is  $10 \text{ ms}^{-1}$ . Observed surface front is depicted using traditional frontal symbols and model-simulated front is shown with heavy dashed line.



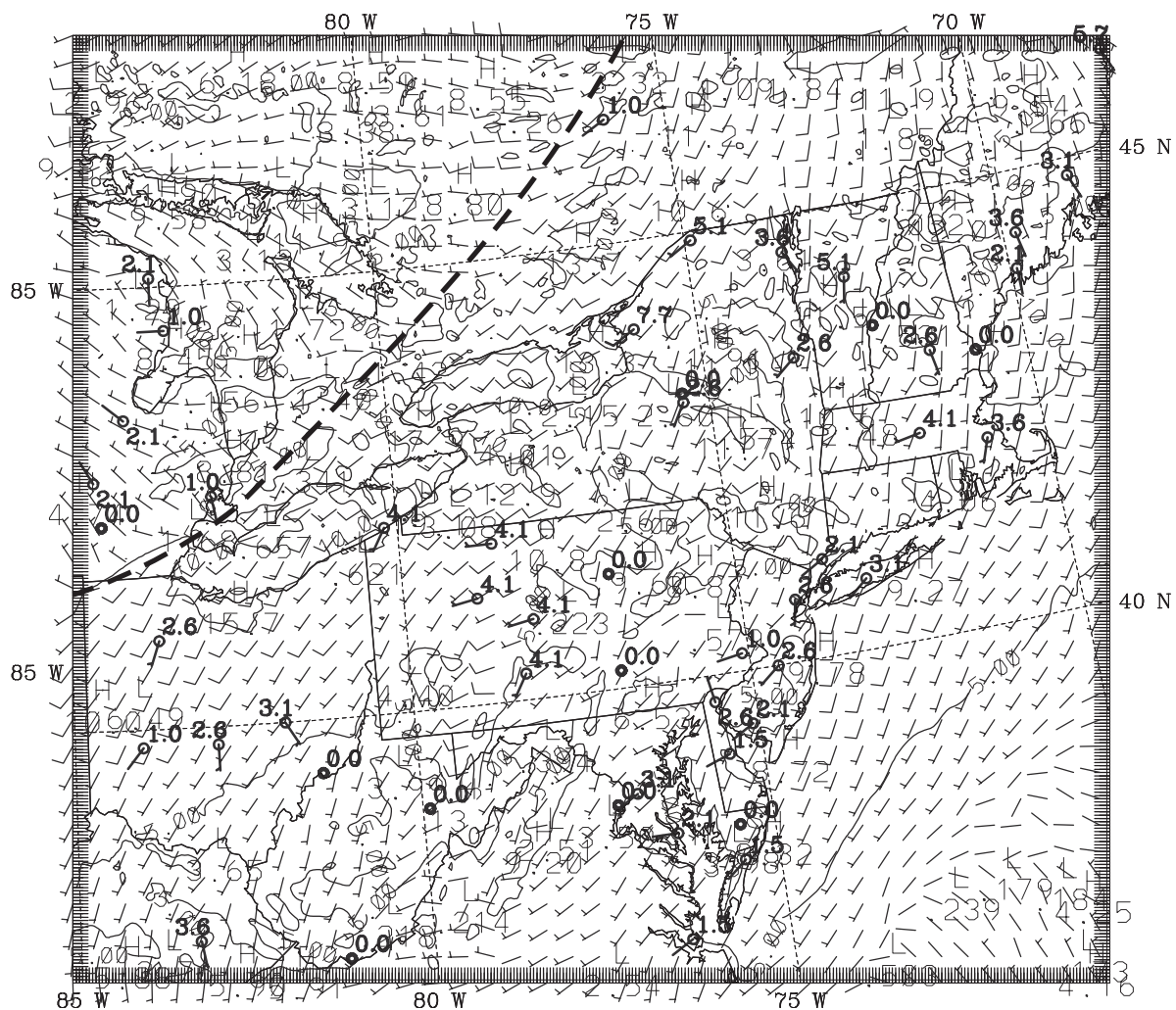




MM5V3-CAPTEX, ms12, 4km, Eta PBL

a)

Figure 6 Model-simulated fields at 21 h (0900 UTC 19 September 1983) on the 4-km domain in Exp. MS12, (a) 3-h total precipitation (mm), (b) Surface-layer wind overlaid with observed surface winds ( $\text{ms}^{-1}$ ). Rain contours are 1, 5, 10 and 25 mm, speed contours are  $5 \text{ ms}^{-1}$  and one barb is  $10 \text{ ms}^{-1}$ . Observed surface front is depicted using traditional frontal symbols and model-simulated front is shown with heavy dashed line.

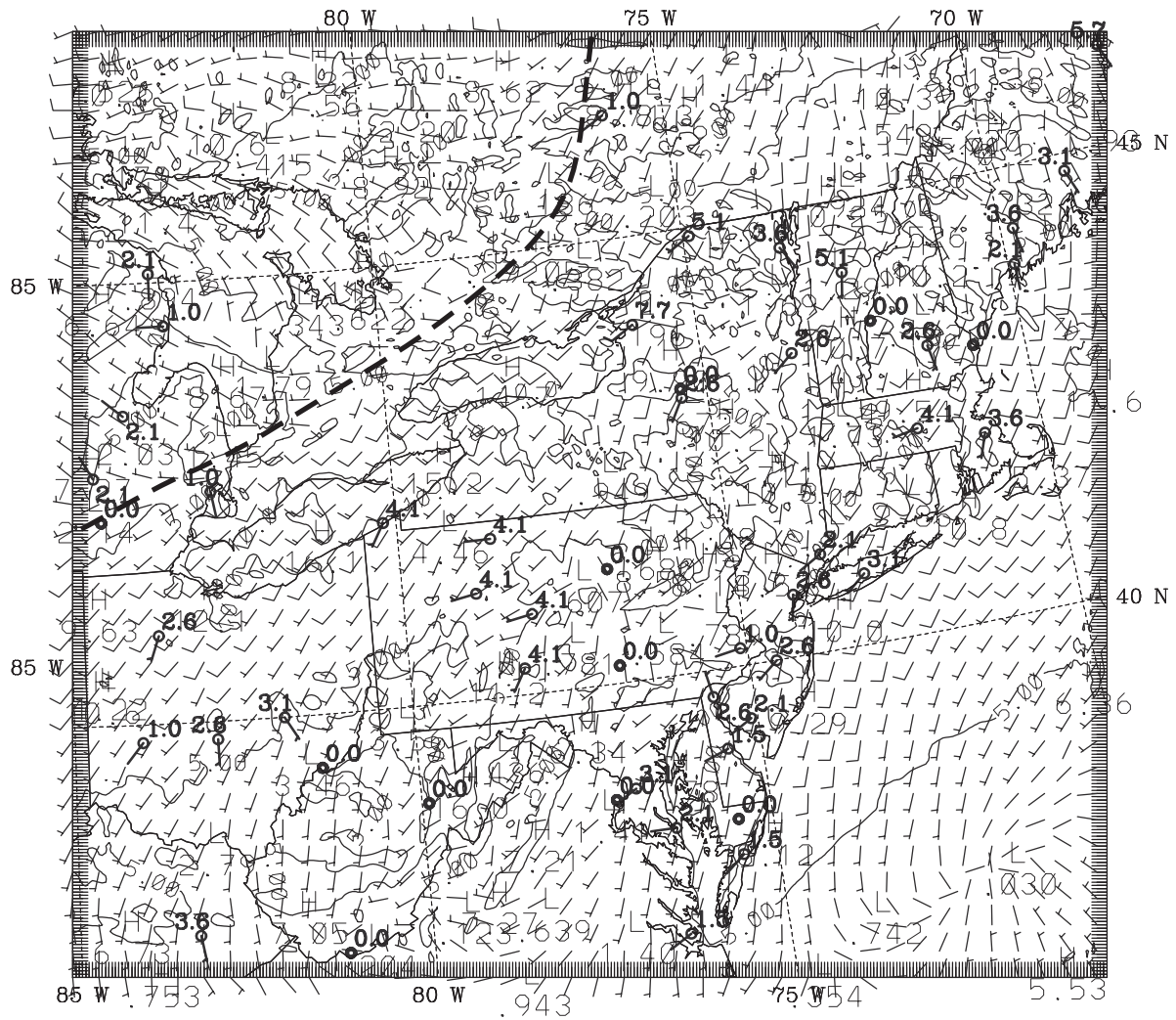


MM5V3-CAPTEX, ms12, 4km, Eta PBL

b)

Figure 6 (Continued).

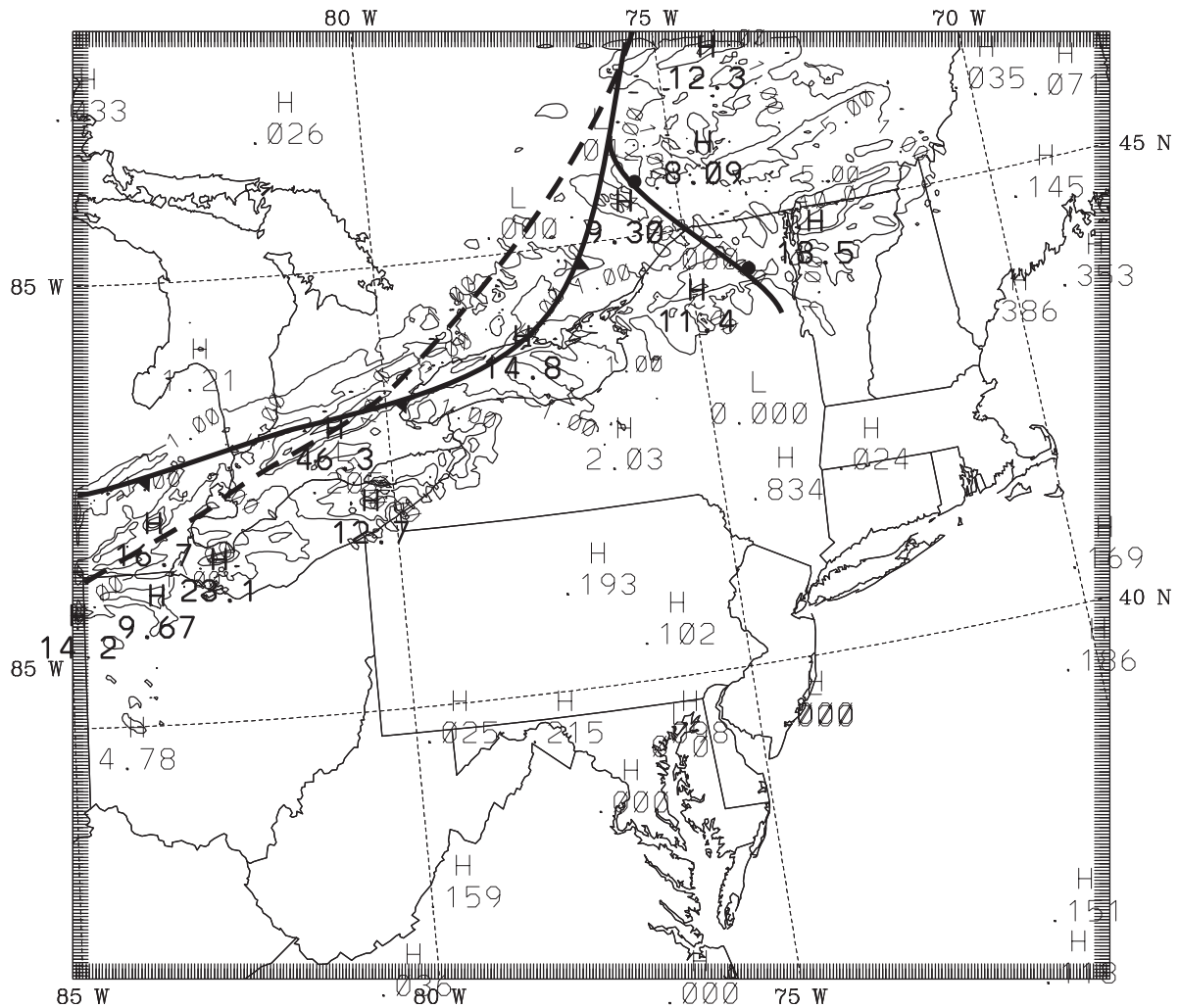




WRF-CAPTEX, WB2, 4km, no CPS, Eta PBL

b)

Figure 7 (Continued).



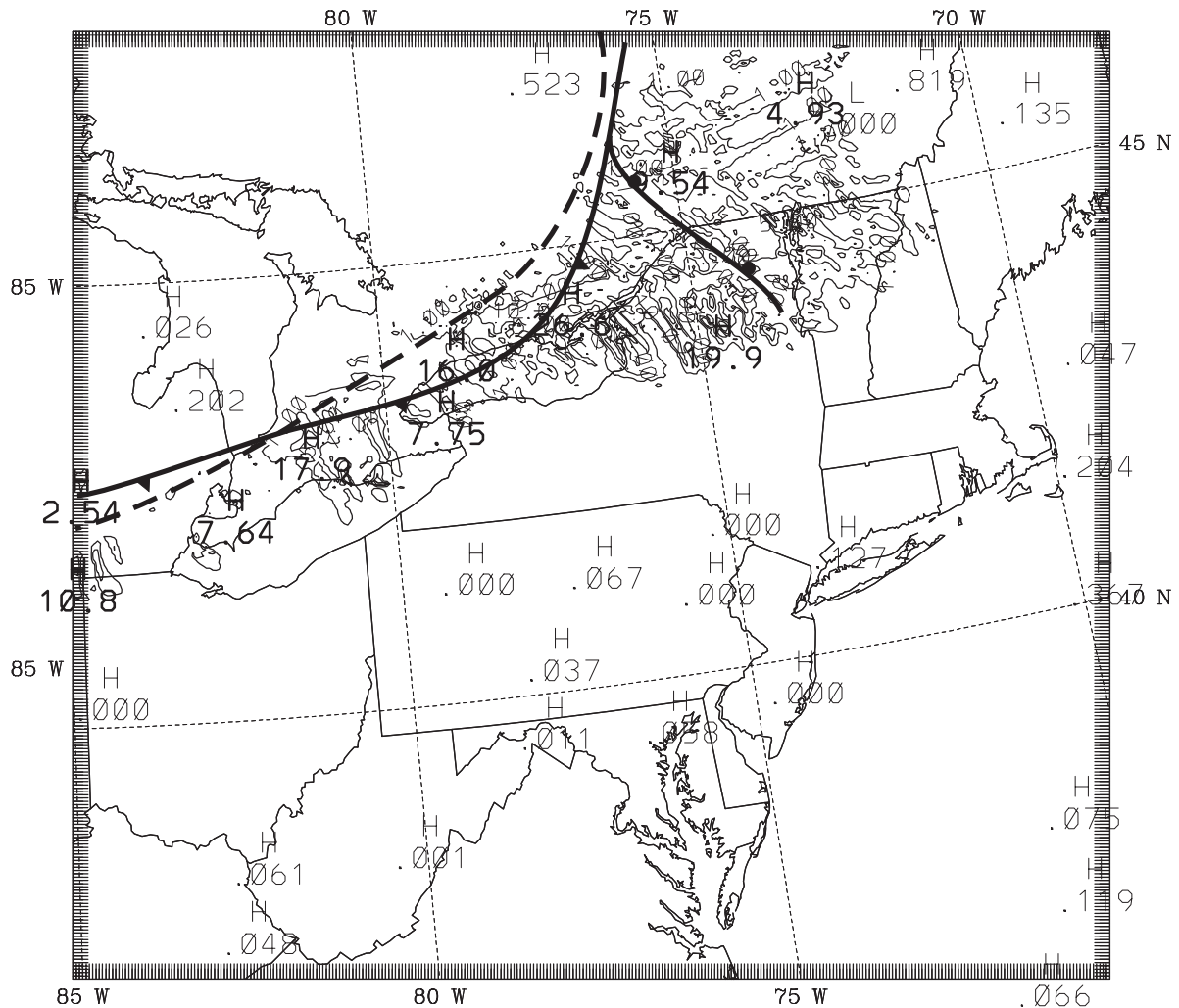
MM5V3-CAPTEX, MS12KF, 4km, KF2, Eta PBL, No FDDA

a)

Figure 8 Model-simulated fields at 21 h (0900 UTC 19 September 1983) on the 4-km domain in Exp. MS12KF, (a) 3-h total precipitation (mm), (b) Surface-layer wind overlaid with observed surface winds ( $\text{ms}^{-1}$ ). Rain contours are 1, 5, 10 and 25 mm, speed contours are  $5 \text{ ms}^{-1}$  and one barb is  $10 \text{ ms}^{-1}$ . Observed surface front is depicted using traditional frontal symbols and model-simulated front is shown with heavy dashed line.



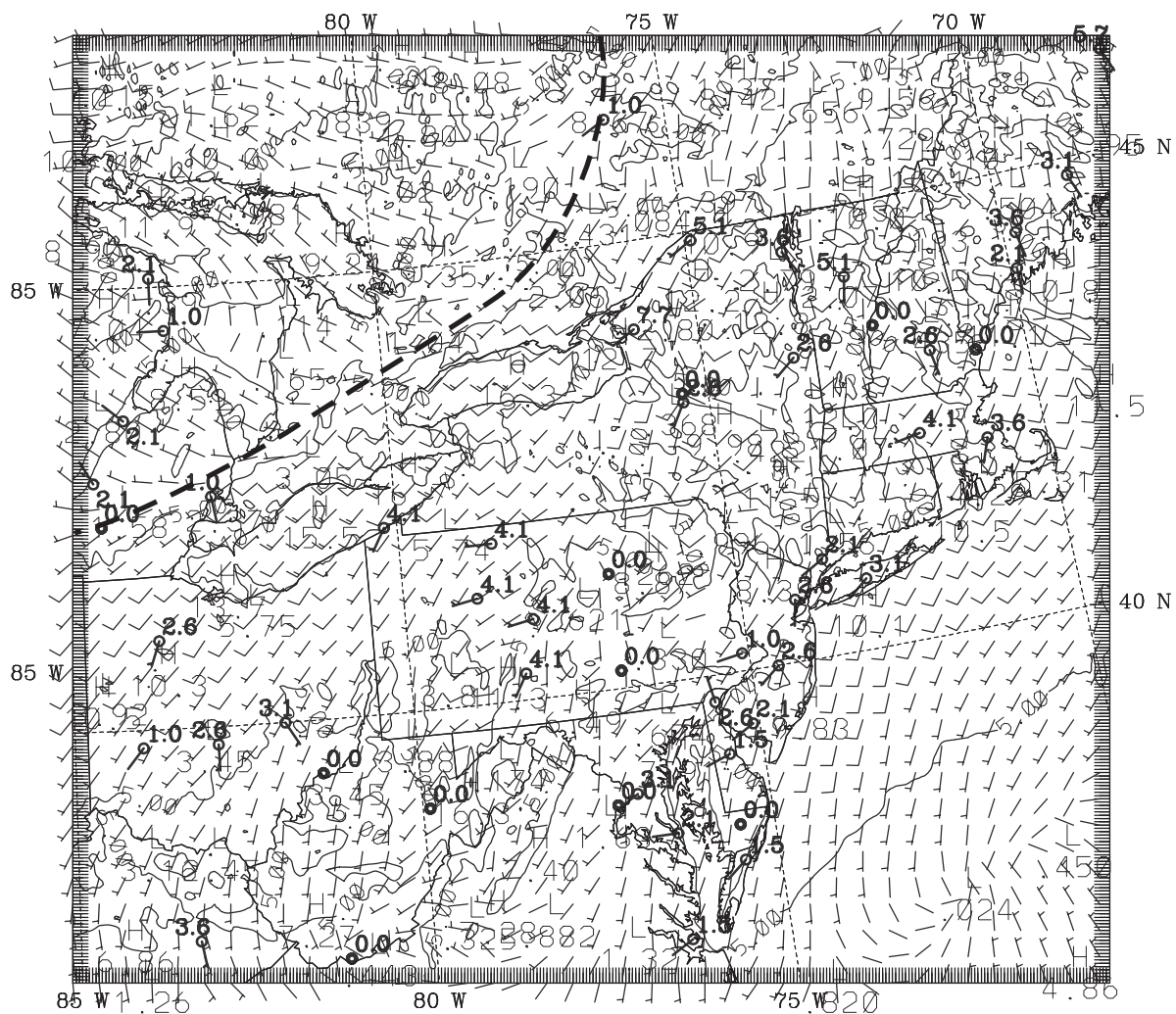




WRF-CAPTEX, WB2KF, 4km, KF2, Eta PBL

a)

Figure 9 Model-simulated fields at 21 h (0900 UTC 19 September 1983) on the 4-km domain in Exp. WB2KF, (a) 3-h total precipitation (mm), (b) Surface-layer wind overlaid with observed surface winds ( $\text{ms}^{-1}$ ). Rain contours are 1, 5, 10 and 25 mm, speed contours are  $5 \text{ ms}^{-1}$  and one barb is  $10 \text{ ms}^{-1}$ . Observed surface front is depicted using traditional frontal symbols and model-simulated front is shown with heavy dashed line.

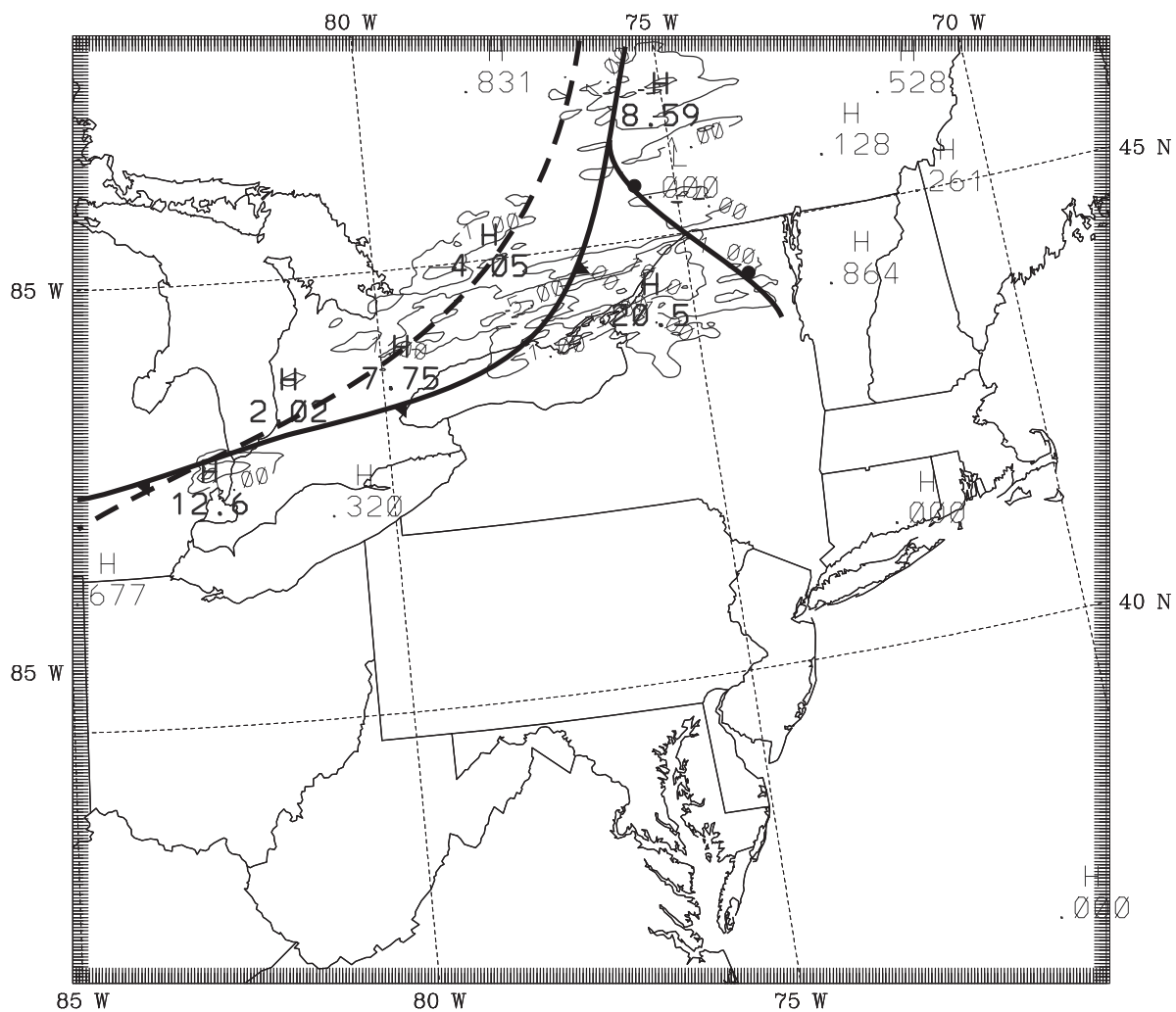


WRF-CAPTEX, WB2KF, 4km, KF2, Eta PBL

b)

Figure 9 (Continued).

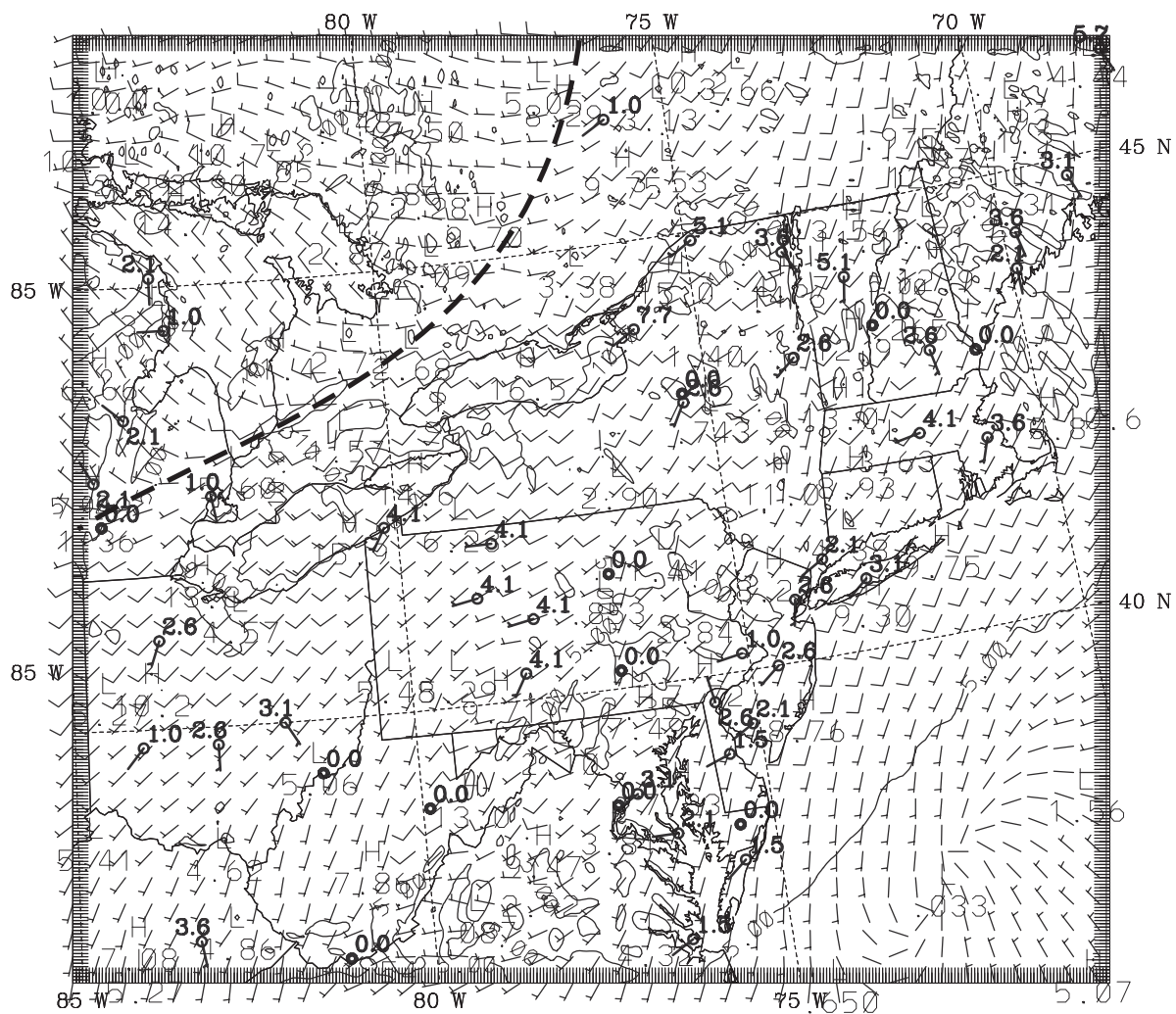




WRF-CAPTEX, WS2, 4km, YSU PBL

a)

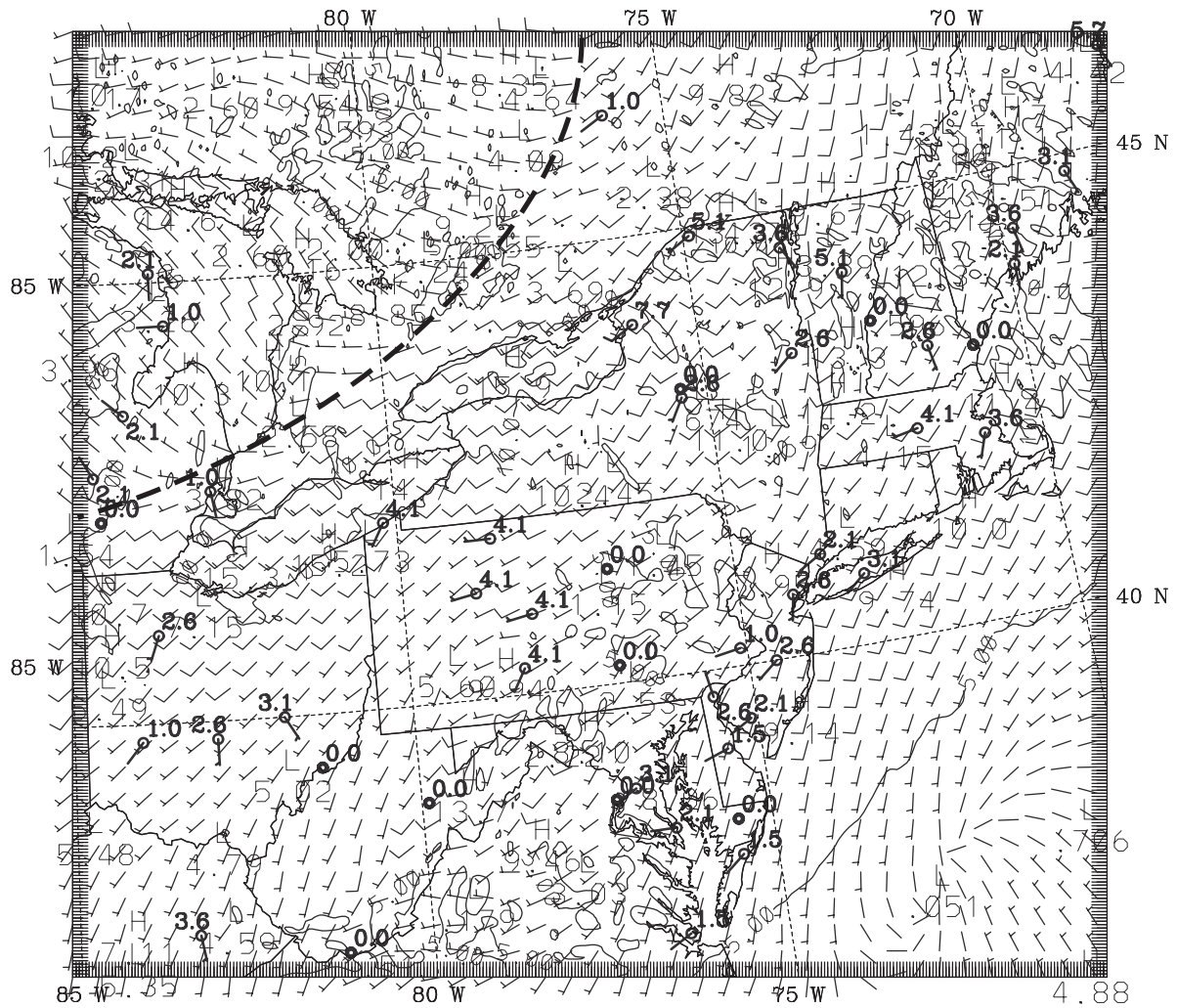
Figure 10 Model-simulated fields at 21 h (0900 UTC 19 September 1983) on the 4-km domain in Exp. WS2, (a) 3-h total precipitation (mm), (b) Surface-layer wind overlaid with observed surface winds ( $\text{ms}^{-1}$ ). Rain contours are 1, 5, 10 and 25 mm, speed contours are  $5 \text{ ms}^{-1}$  and one barb is  $10 \text{ ms}^{-1}$ . Observed surface front is depicted using traditional frontal symbols and model-simulated front is shown with heavy dashed line.



b)  
WRF-CAPTEX, WS2, 4km, YSU PBL

Figure 10 (Continued).

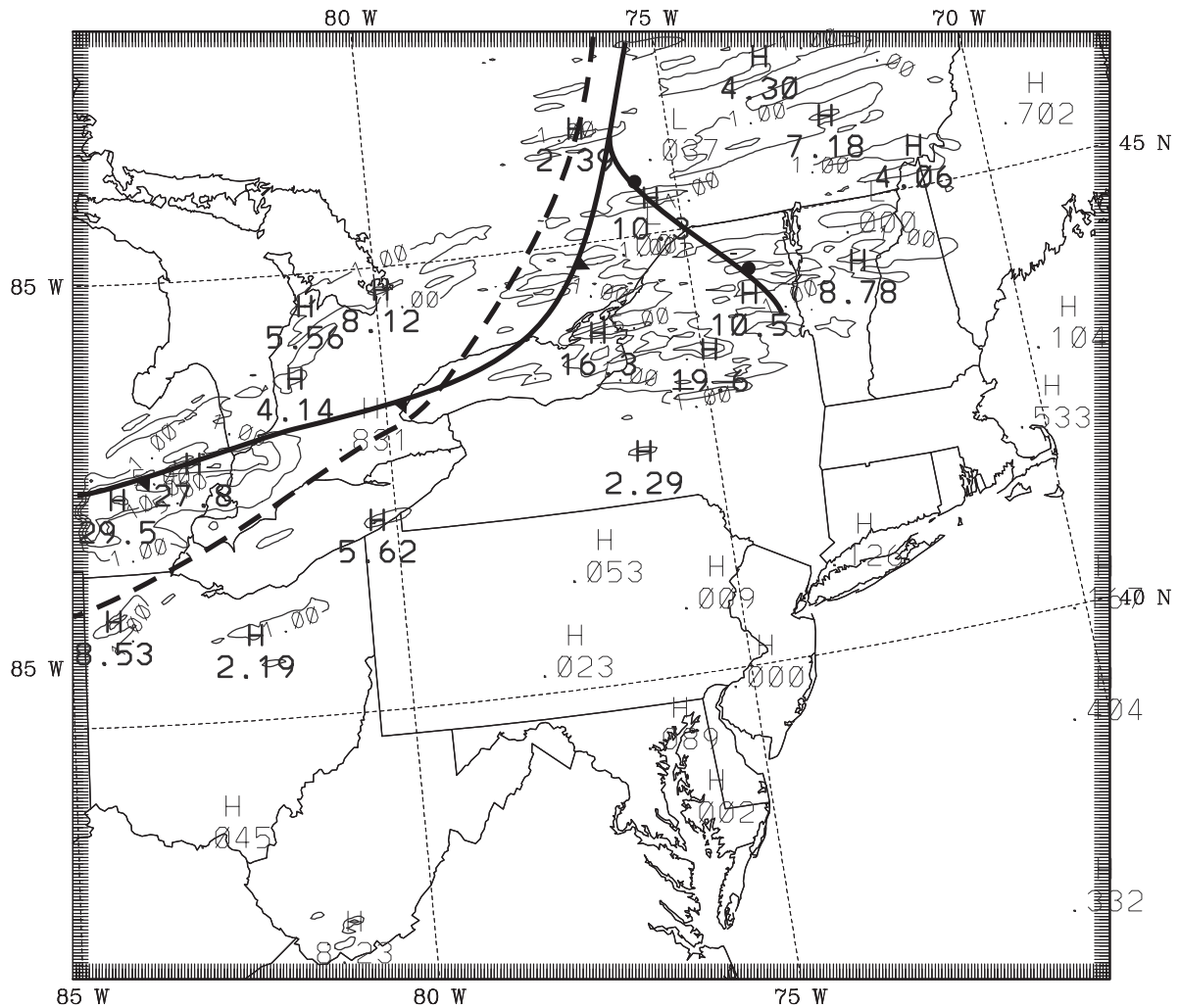




WRF-CAPTEX, WS2KF, 4km, YSU PBL, KF2

b)

Figure 11 (Continued).

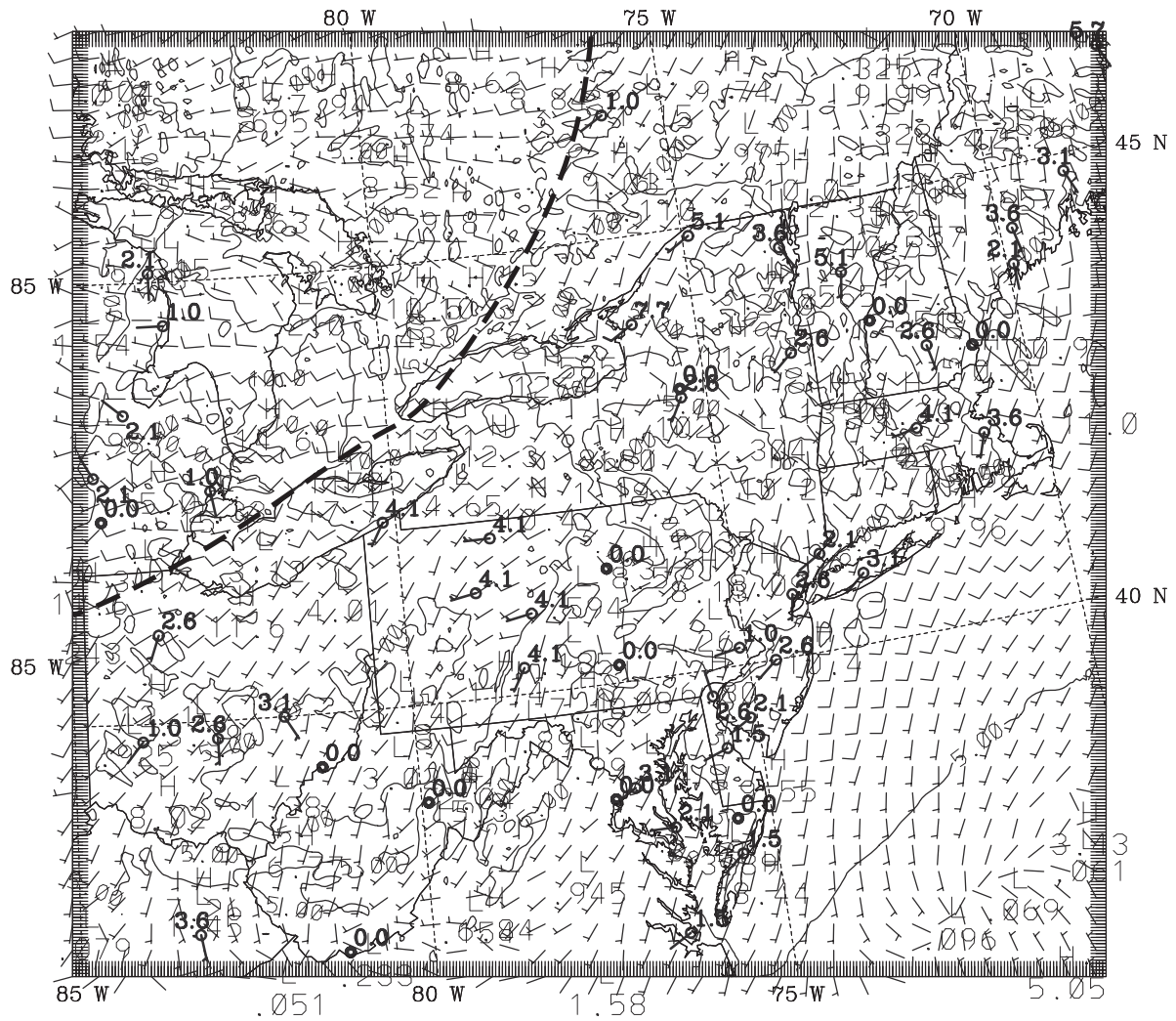


WRF-CAPTEX, WS3, 4km, Eta PBL, no CPS (Grell on upper meshes)

a)

Figure 12 Model-simulated fields at 21 h (0900 UTC 19 September 1983) on the 4-km domain in Exp. WS3, (a) 3-h total precipitation (mm), (b) Surface-layer wind overlaid with observed surface winds ( $\text{ms}^{-1}$ ). Rain contours are 1, 5, 10 and 25 mm, speed contours are  $5 \text{ ms}^{-1}$  and one barb is  $10 \text{ ms}^{-1}$ . Observed surface front is depicted using traditional frontal symbols and model-simulated front is shown with heavy dashed line.



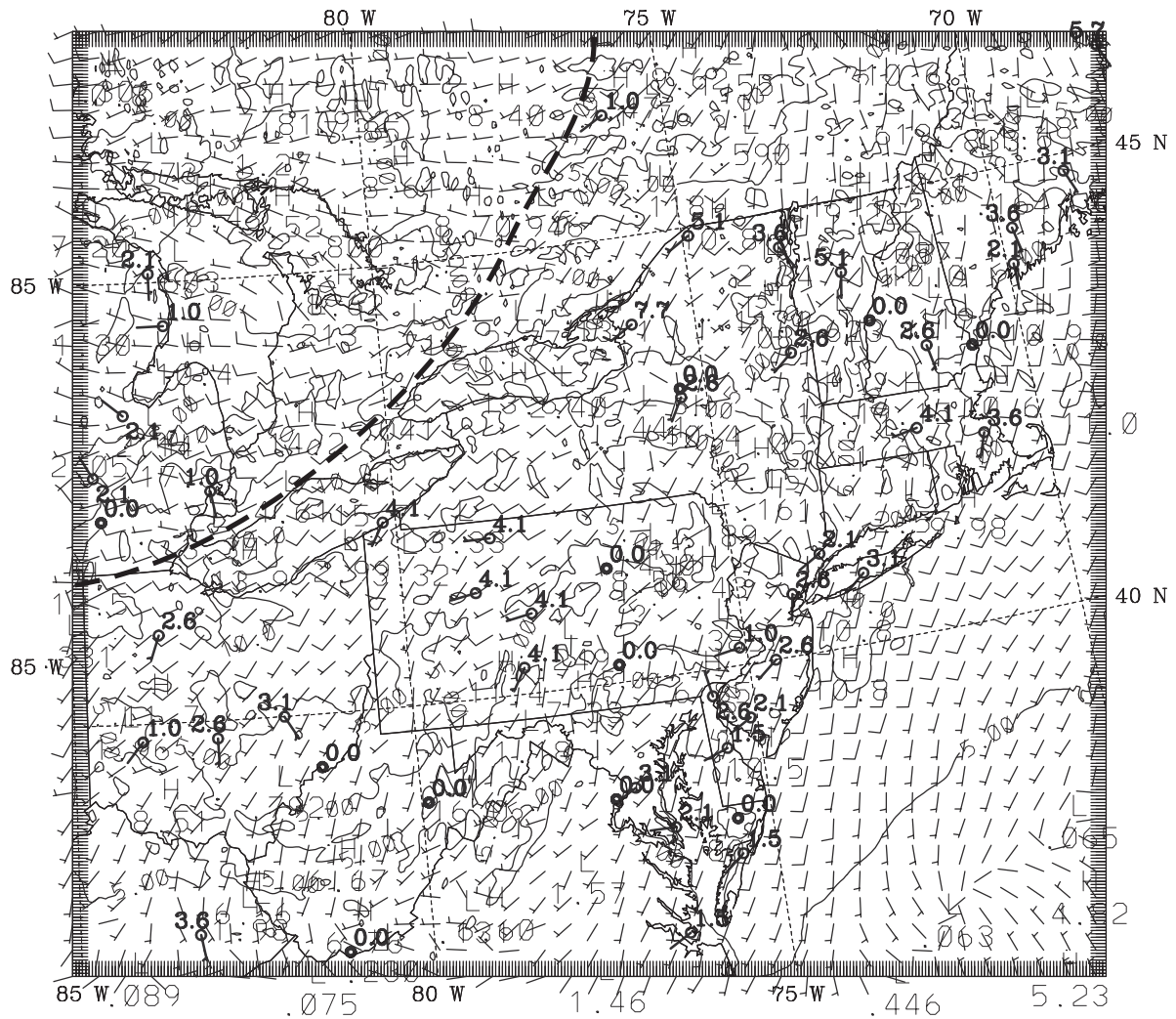


WRF-CAPTEX, WS3, 4km, Eta PBL, no CPS (Grell on upper meshes)

b)

Figure 12 (Continued).





WRF-CAPTEX, WS3GR, 4km, Eta PBL, Grell CPS

b)

Figure 13 (Continued).



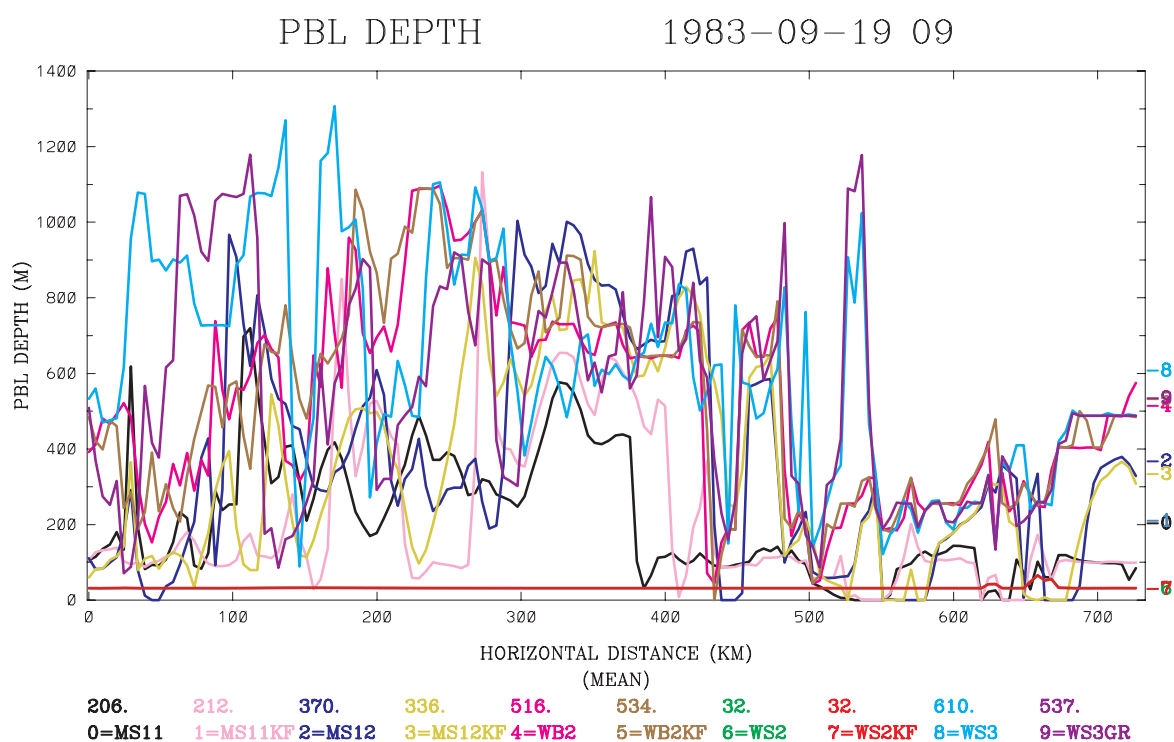
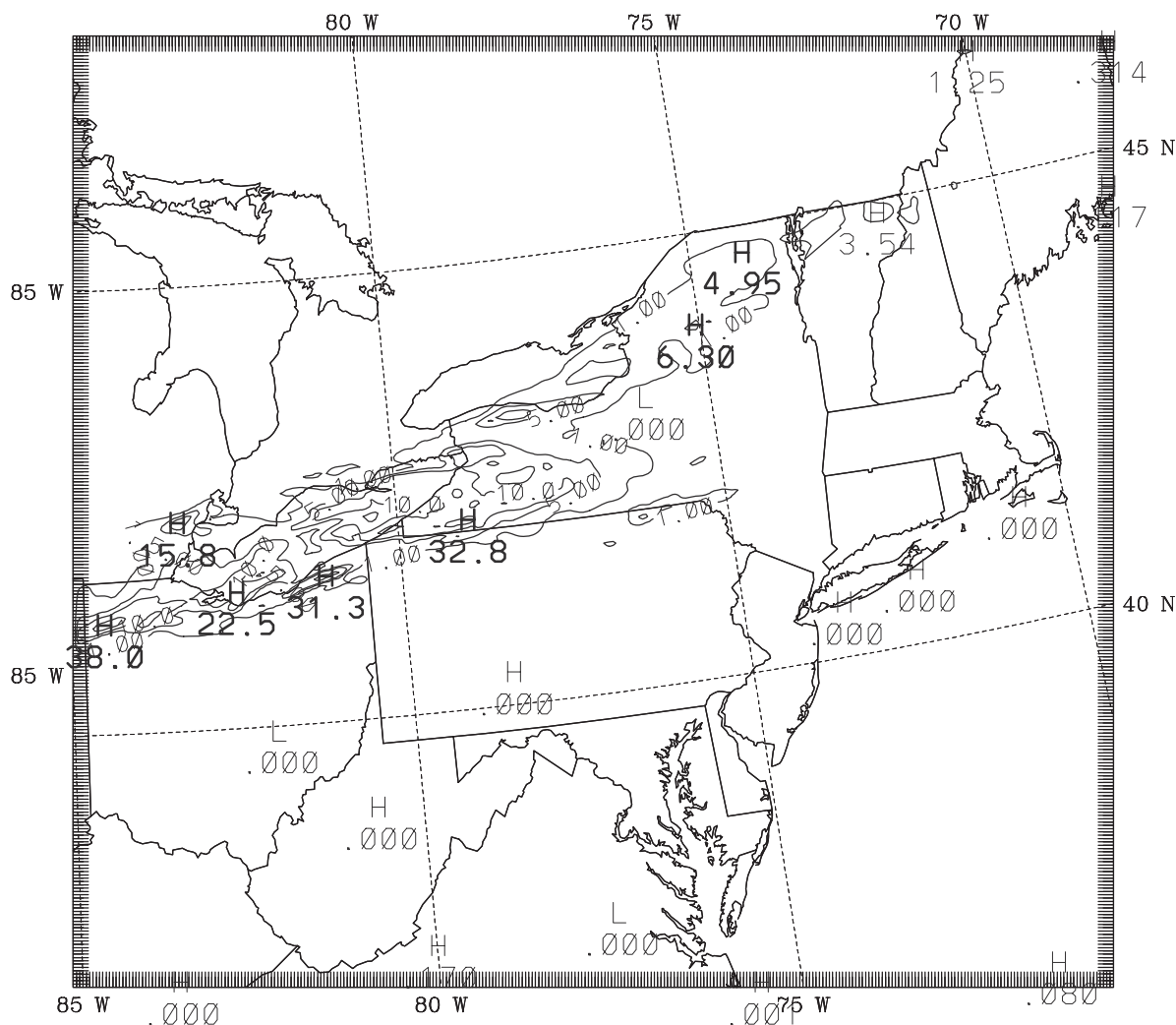


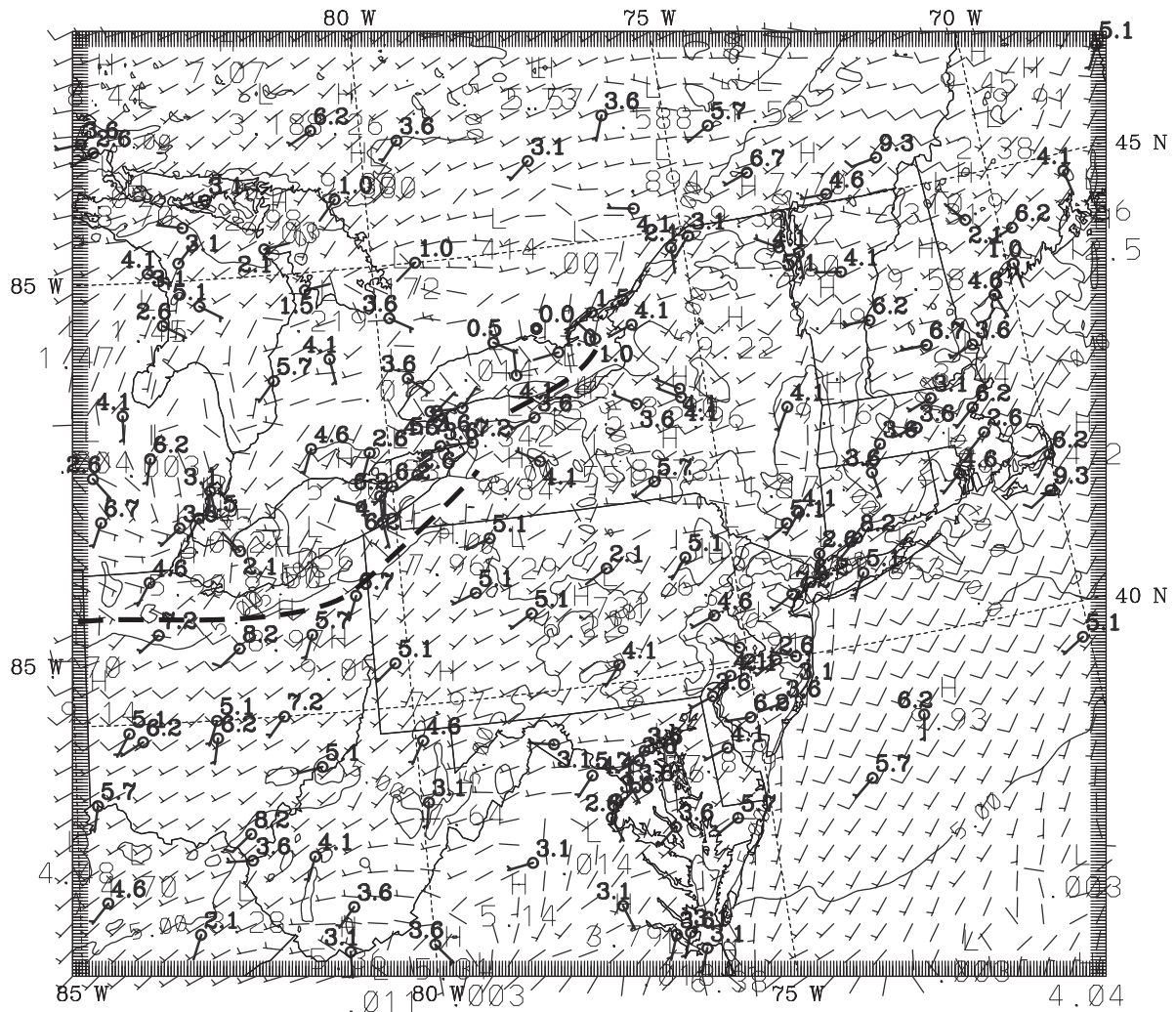
Figure 14 MM5- and WRF-simulated PBL height (m) along the northwest-southeast cross section shown in Fig. 3 for all experiments on the 4-km resolution domain at 21 h (0900 UTC 19 September 1983). The cross-section mean PBL height values are plotted on the right side of the chart with the digital values also included above the experiment key at the bottom of the figure.



MM5V3-CAPTEX MS11, 4km, no CPS, No FDDA  
 CONTOUR FROM 0.0000 TO 30.0000 CONTOUR INTERVAL OF 5.0000 PT(3,3)= 0.12558E-26

a)

**Figure 15** Model-simulated fields at 30 h (1800 UTC 19 September 1983) on the 4-km domain in Exp. MS11. (a) 3-h total precipitation (mm), (b) Surface-layer wind overlaid with observed surface winds ( $\text{ms}^{-1}$ ), and (c) Surface-layer temperature overlaid with observed surface temperature (C). Rain contours are 1, 5, 10 and 25 mm, speed contours are  $5 \text{ ms}^{-1}$  and one barb is  $10 \text{ ms}^{-1}$ , and temperature contours are 1 C. Heavy dashed lines are used to illustrate wind-shift lines likely associated with convective outflow boundaries and precipitation-induced cold pools. A red L and temperature value (C) is used to denote a surface cold pool (i.e., a surface-layer temperature minimum located within or near a model-precipitation region).

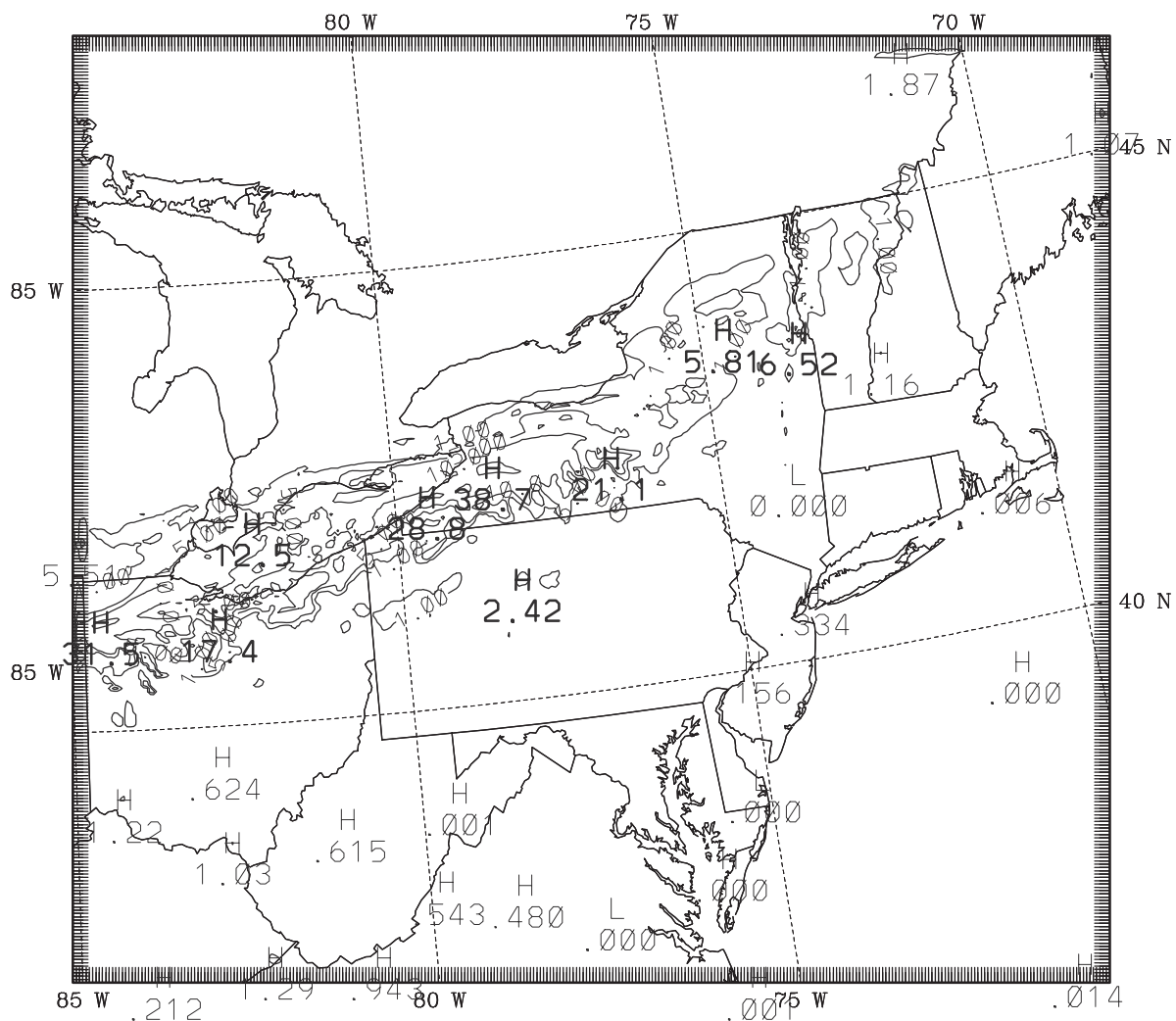


MM5V3-CAPTEX MS11, 4km, no CPS, No FDDA

b)

Figure 15 (Continued)



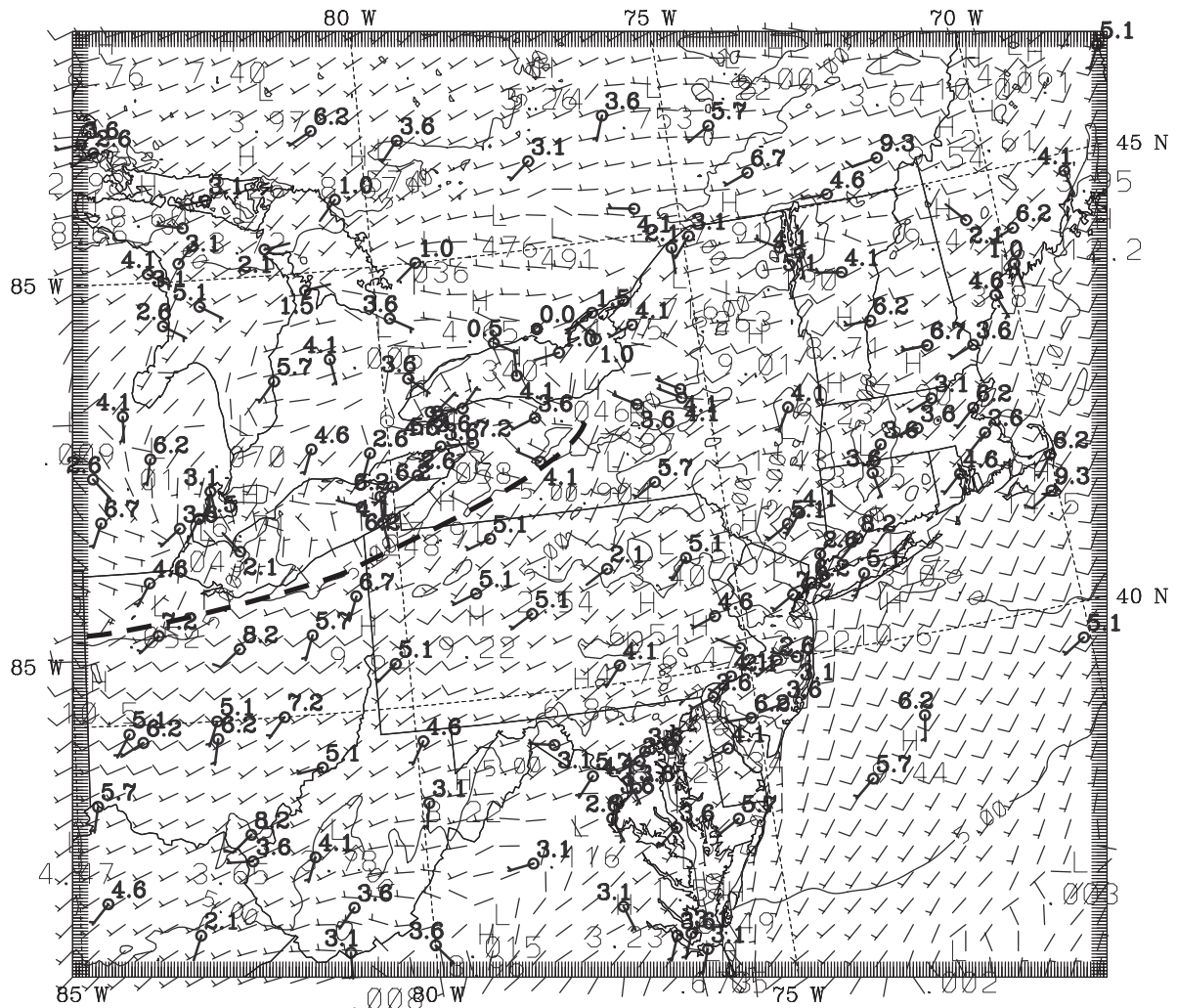


MM5V3-CAPTEX MS11KF, 4km, KF2, No FDDA

a)

Figure 16 Model-simulated fields at 30 h (1800 UTC 19 September 1983) on the 4-km domain in Exp. MS11KF. (a) 3-h total precipitation (mm), (b) Surface-layer wind overlaid with observed surface winds ( $\text{ms}^{-1}$ ), and (c) Surface-layer temperature overlaid with observed surface temperature ( $^{\circ}\text{C}$ ). Rain contours are 1, 5, 10 and 25 mm, speed contours are  $5 \text{ ms}^{-1}$  and one barb is  $10 \text{ ms}^{-1}$ , and temperature contours are  $1^{\circ}\text{C}$ . Heavy dashed lines are used to illustrate wind-shift lines likely associated with convective outflow boundaries and precipitation-induced cold pools. A red L and temperature value ( $^{\circ}\text{C}$ ) is used to denote a surface cold pool (i.e., a surface-layer temperature minimum located within or near a model-precipitation region).

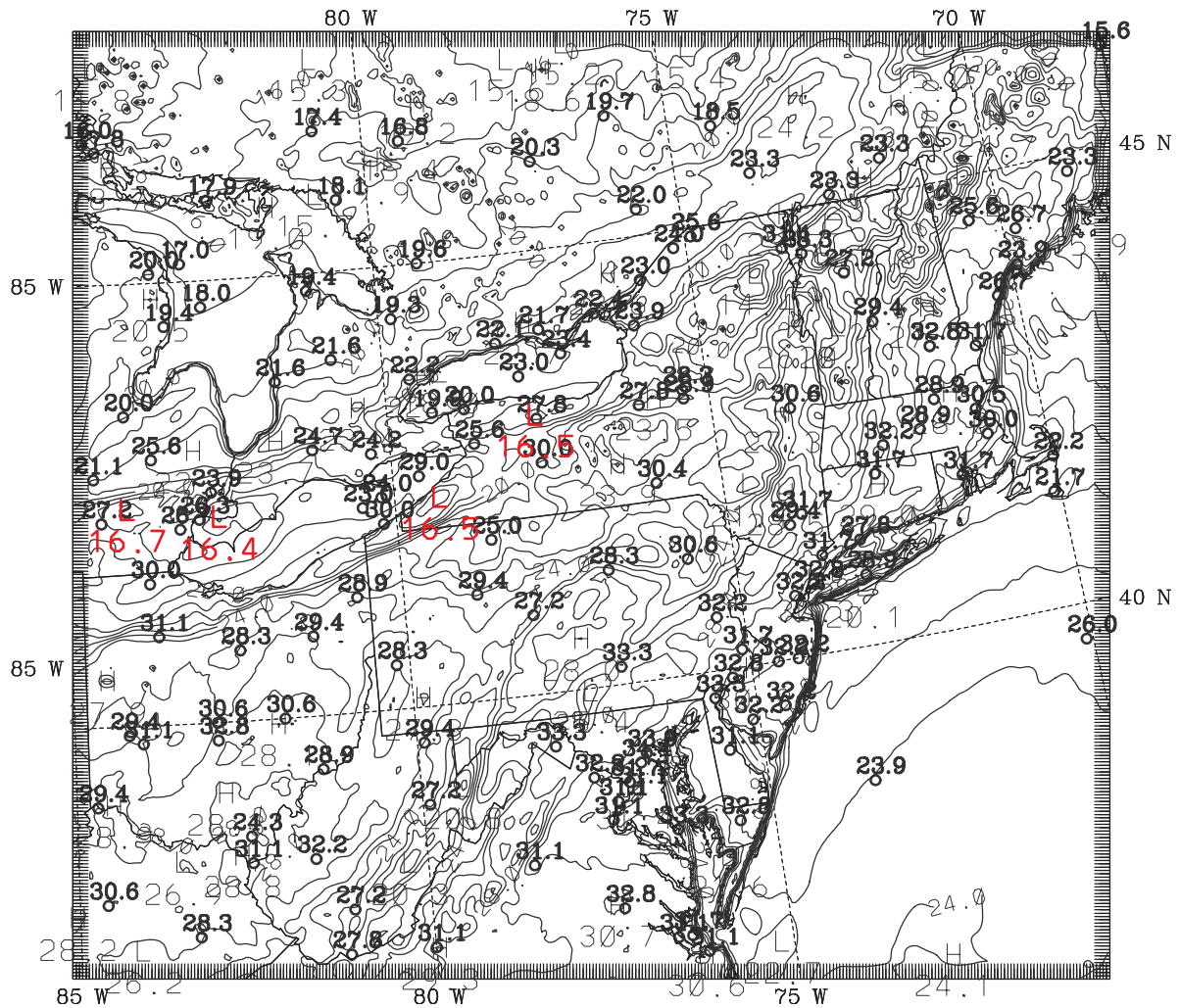




MM5V3-CAPTEX MS11KF, 4km, KF2, No FDDA

b)

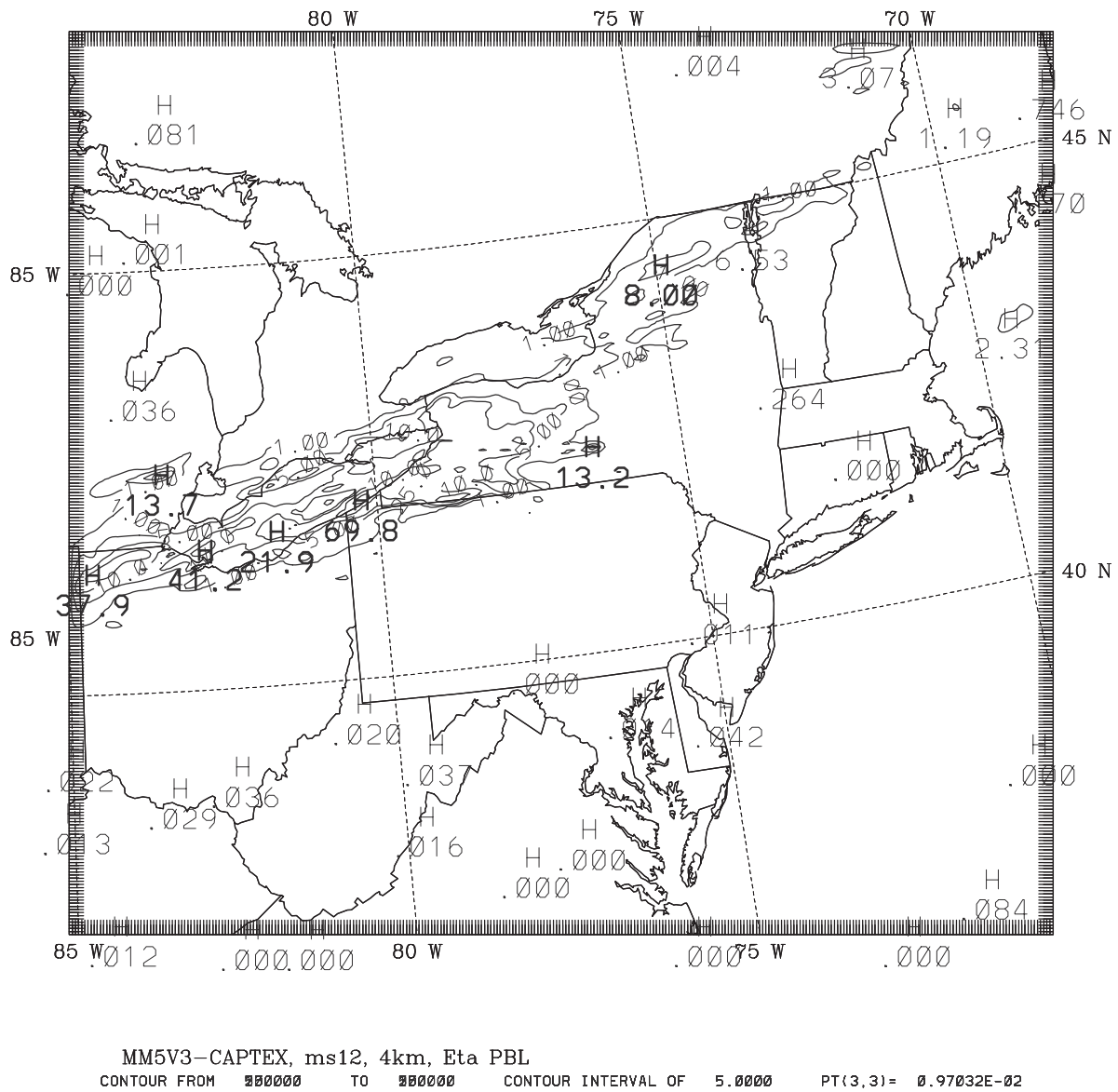
Figure 16 (Continued)



MM5V3-CAPTEX, MS11KF, 4km, KF2, no FDDA  
 CONTOUR FROM 11.000 TO 31.000 CONTOUR INTERVAL OF 1.0000 PT(3,3)= 27.529

c)

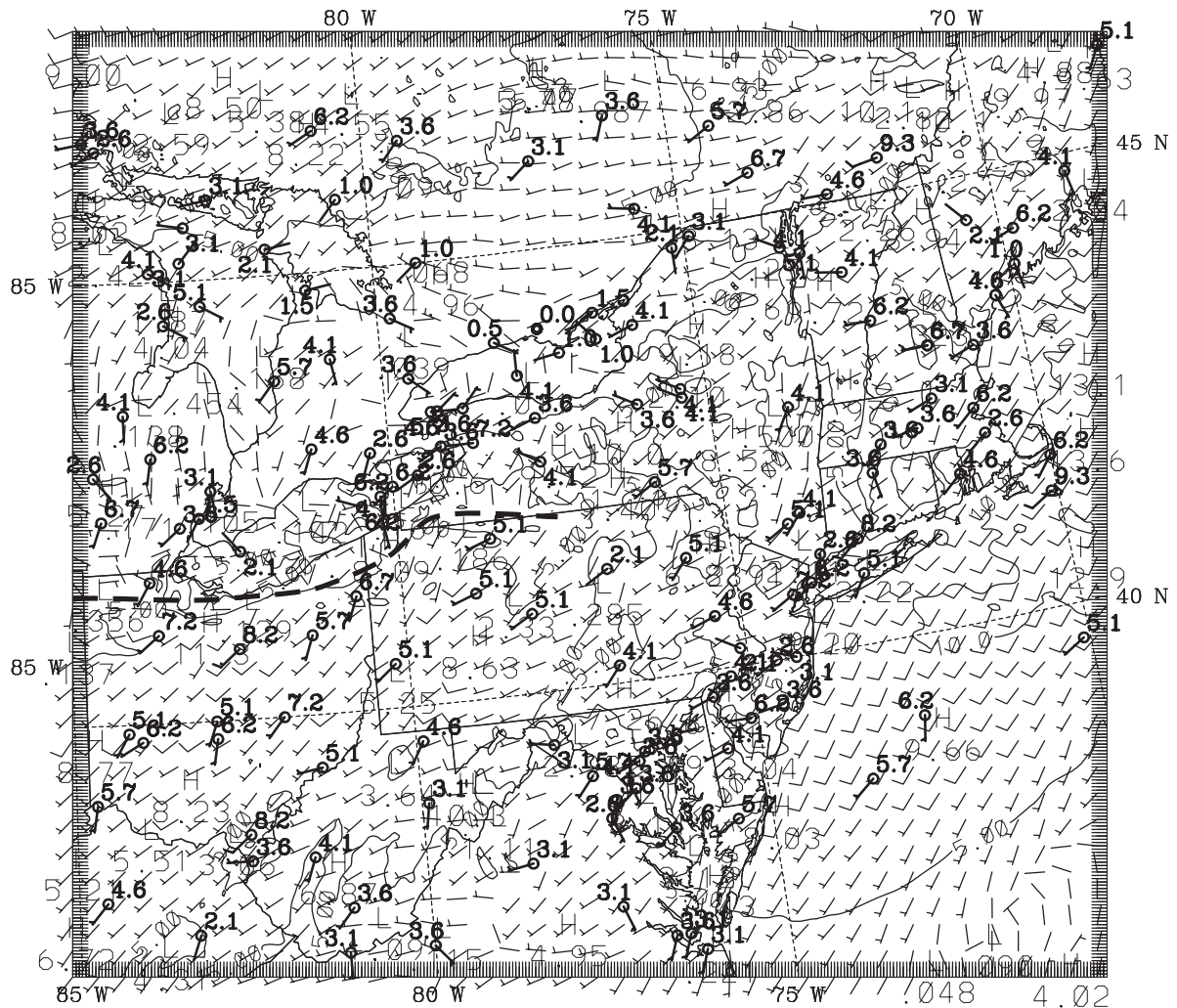
Figure 16 (Continued)



a)

Figure 17 Model-simulated fields at 30 h (1800 UTC 19 September 1983) on the 4-km domain in Exp. MS12. (a) 3-h total precipitation (mm), (b) Surface-layer wind overlaid with observed surface winds ( $\text{ms}^{-1}$ ), and (c) Surface-layer temperature overlaid with observed surface temperature ( $^{\circ}\text{C}$ ). Rain contours are 1, 5, 10 and 25 mm, speed contours are  $5 \text{ ms}^{-1}$  and one barb is  $10 \text{ ms}^{-1}$ , and temperature contours are  $1^{\circ}\text{C}$ . Heavy dashed lines are used to illustrate wind-shift lines likely associated with convective outflow boundaries and precipitation-induced cold pools. A red L and temperature value ( $^{\circ}\text{C}$ ) is used to denote a surface cold pool (i.e., a surface-layer temperature minimum located within or near a model-precipitation region).

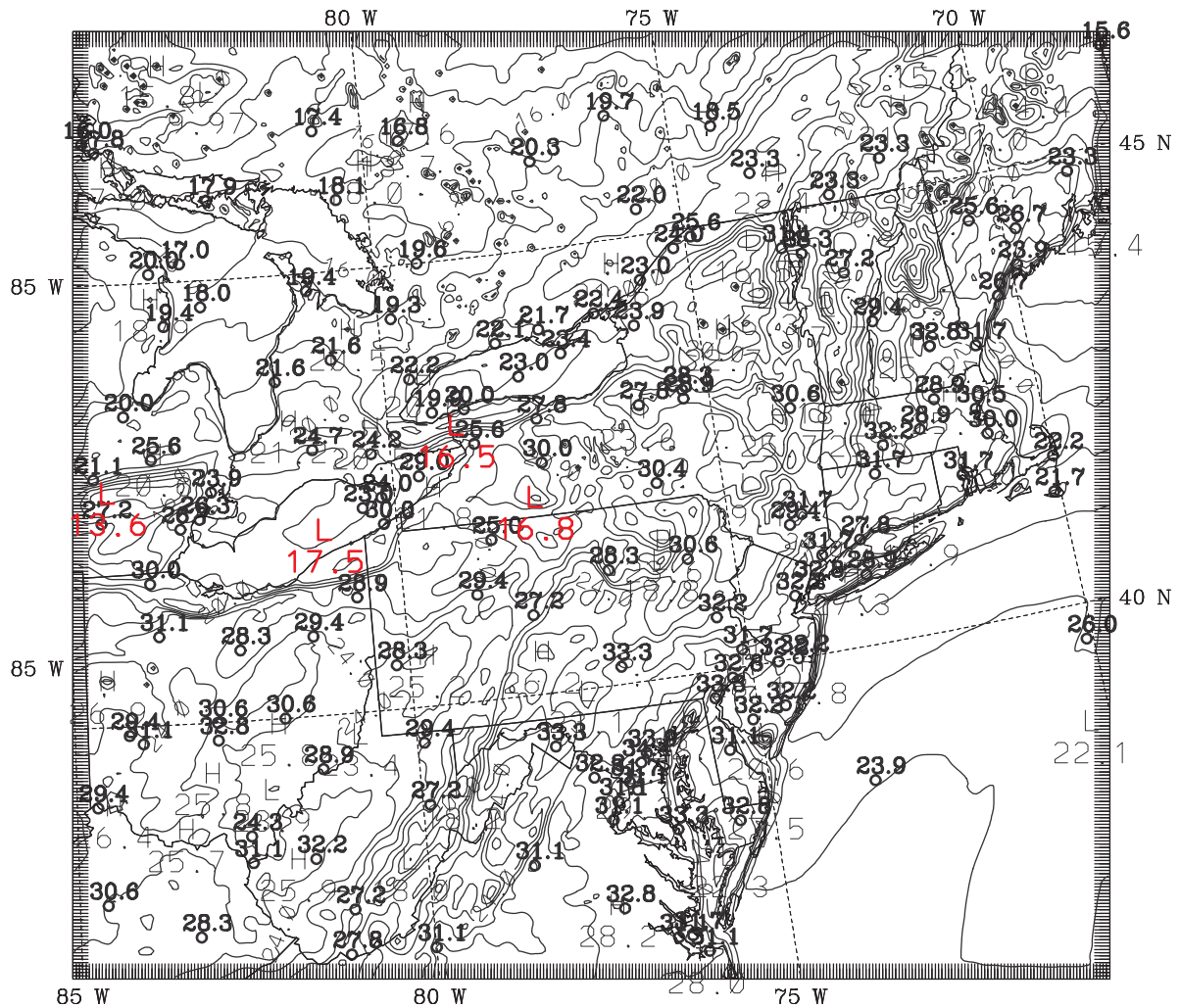




MM5V3-CAPTEX, ms12, 4km, Eta PBL

b)

Figure 17 (Continued)

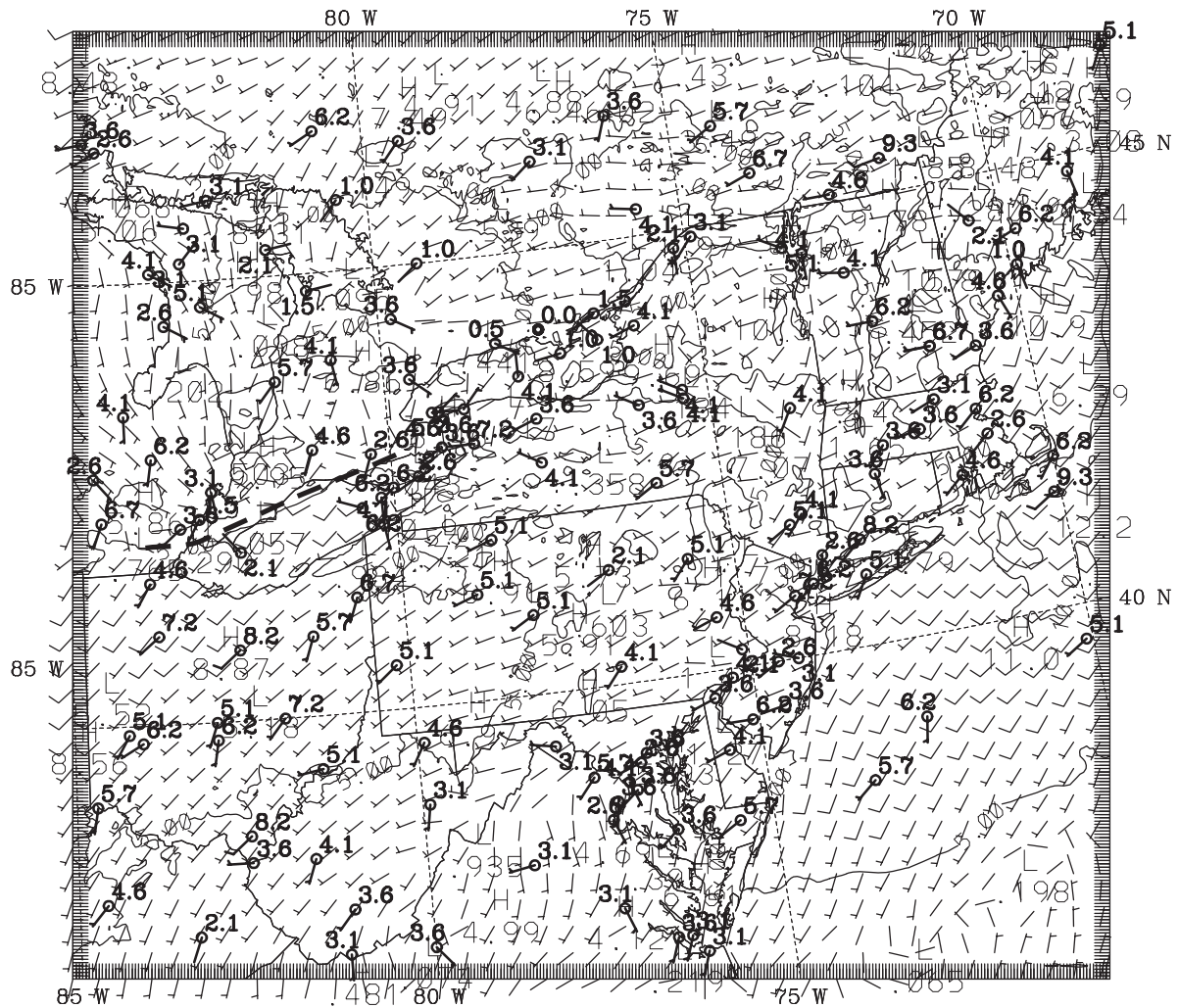


MM5V3-CAPTEX, MS12, 4km, Eta PBL  
 CONTOUR FROM 9.0000 TO 29.000 CONTOUR INTERVAL OF 1.0000 PT(3,3)= 24.774

c)

Figure 17 (Continued)



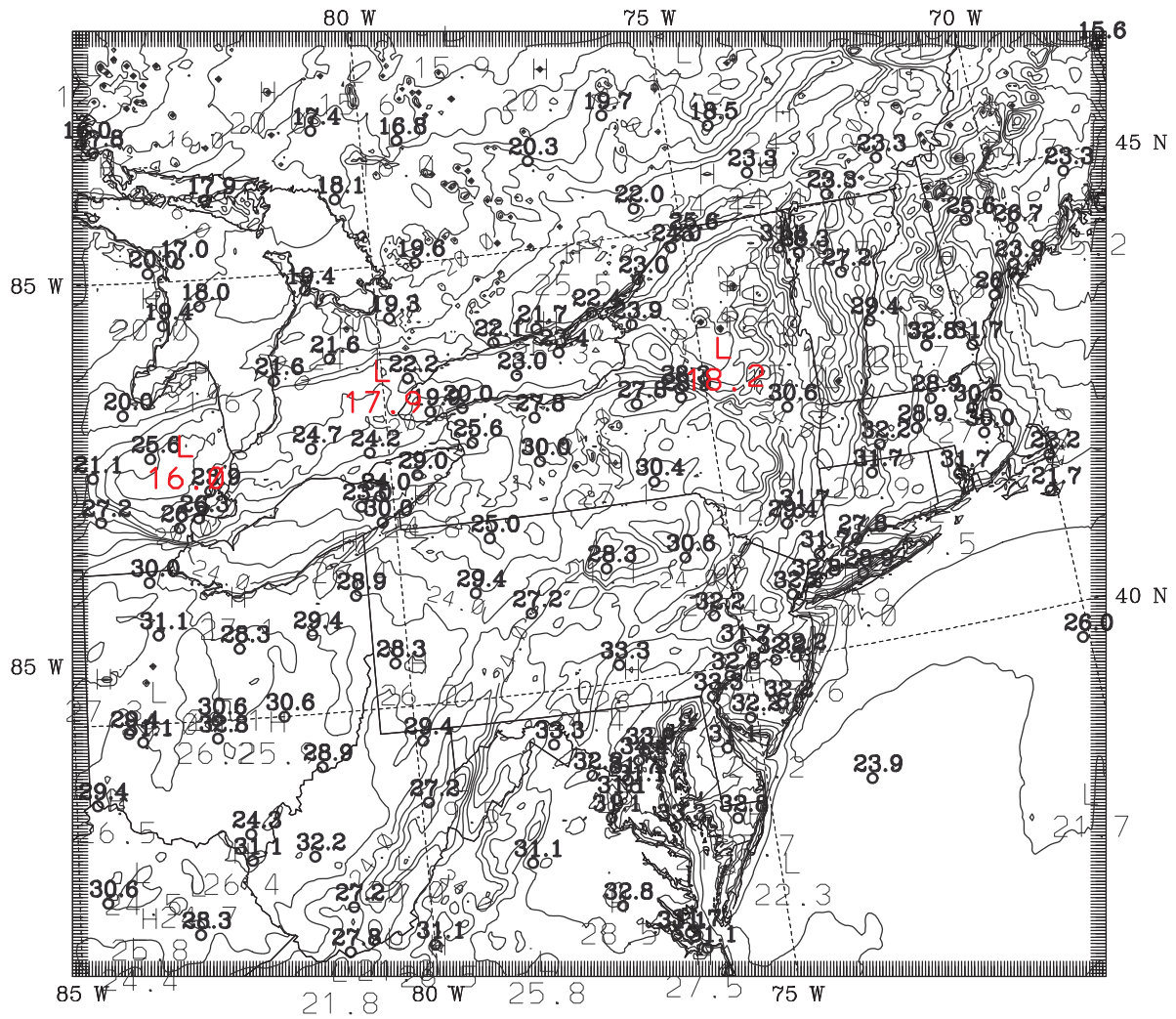


WRF-CAPTEX, WB2, 4km, no CPS, Eta PBL

b)

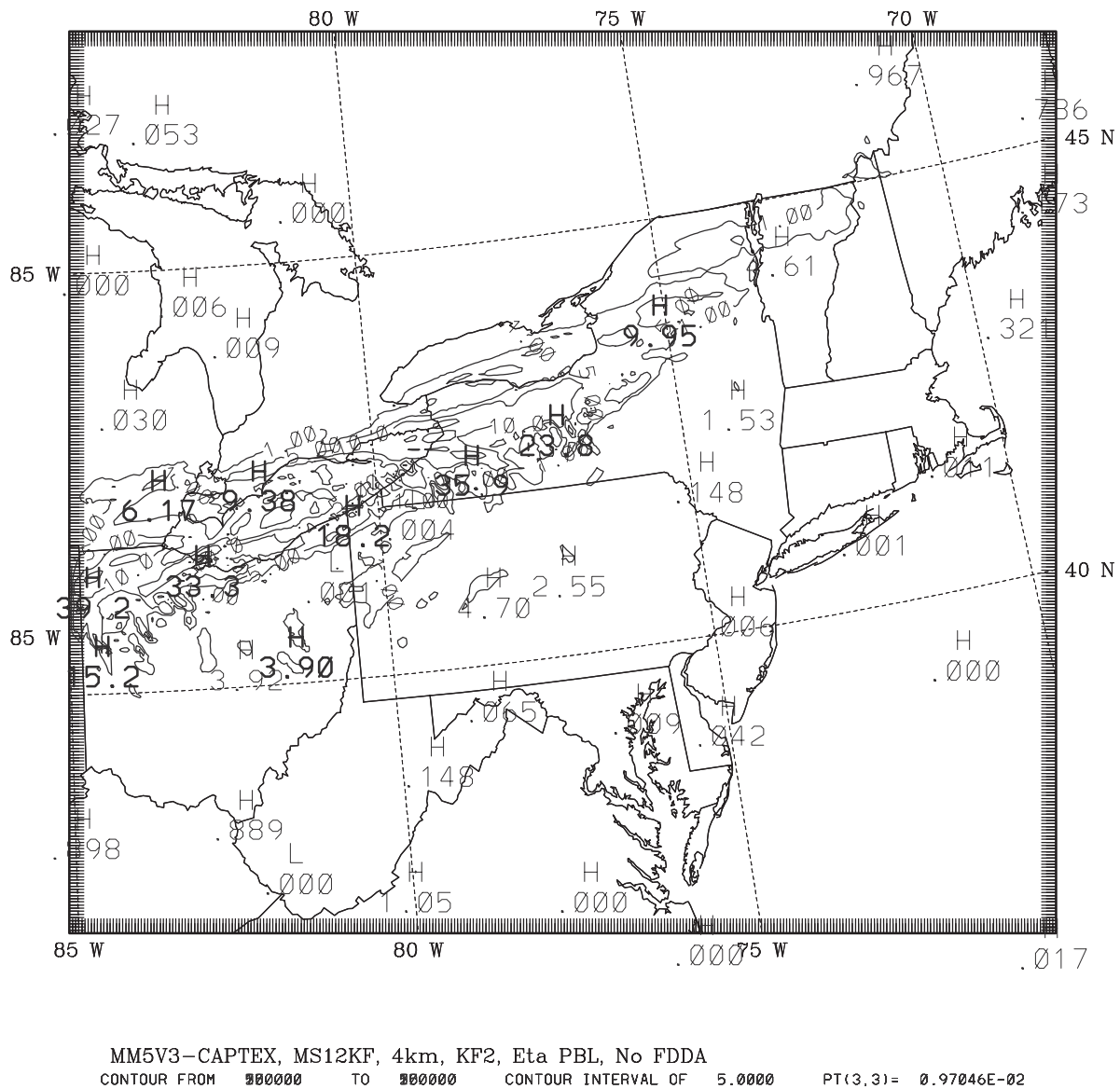
Figure 18 (Continued)





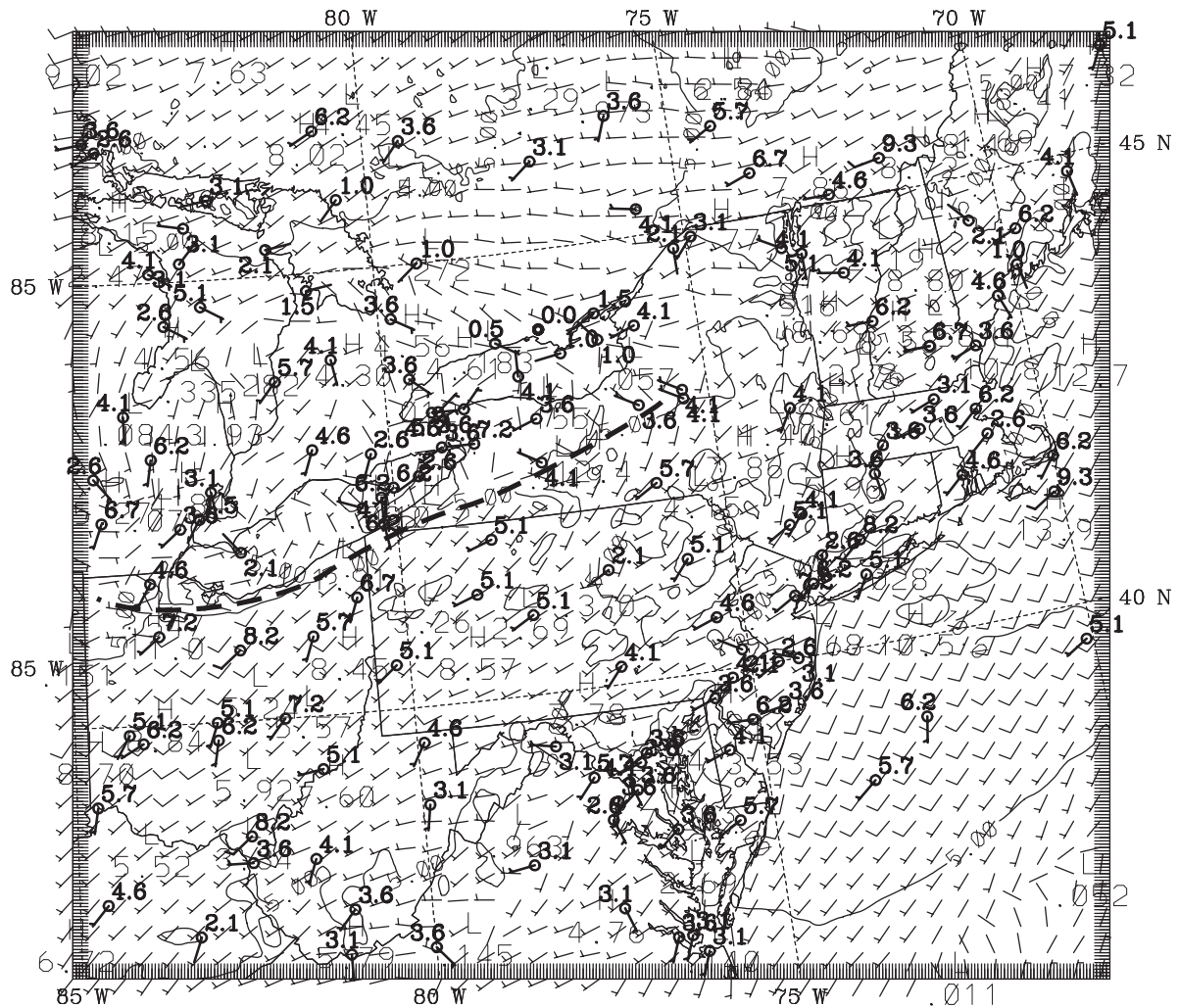
c)

Figure 18 (Continued)



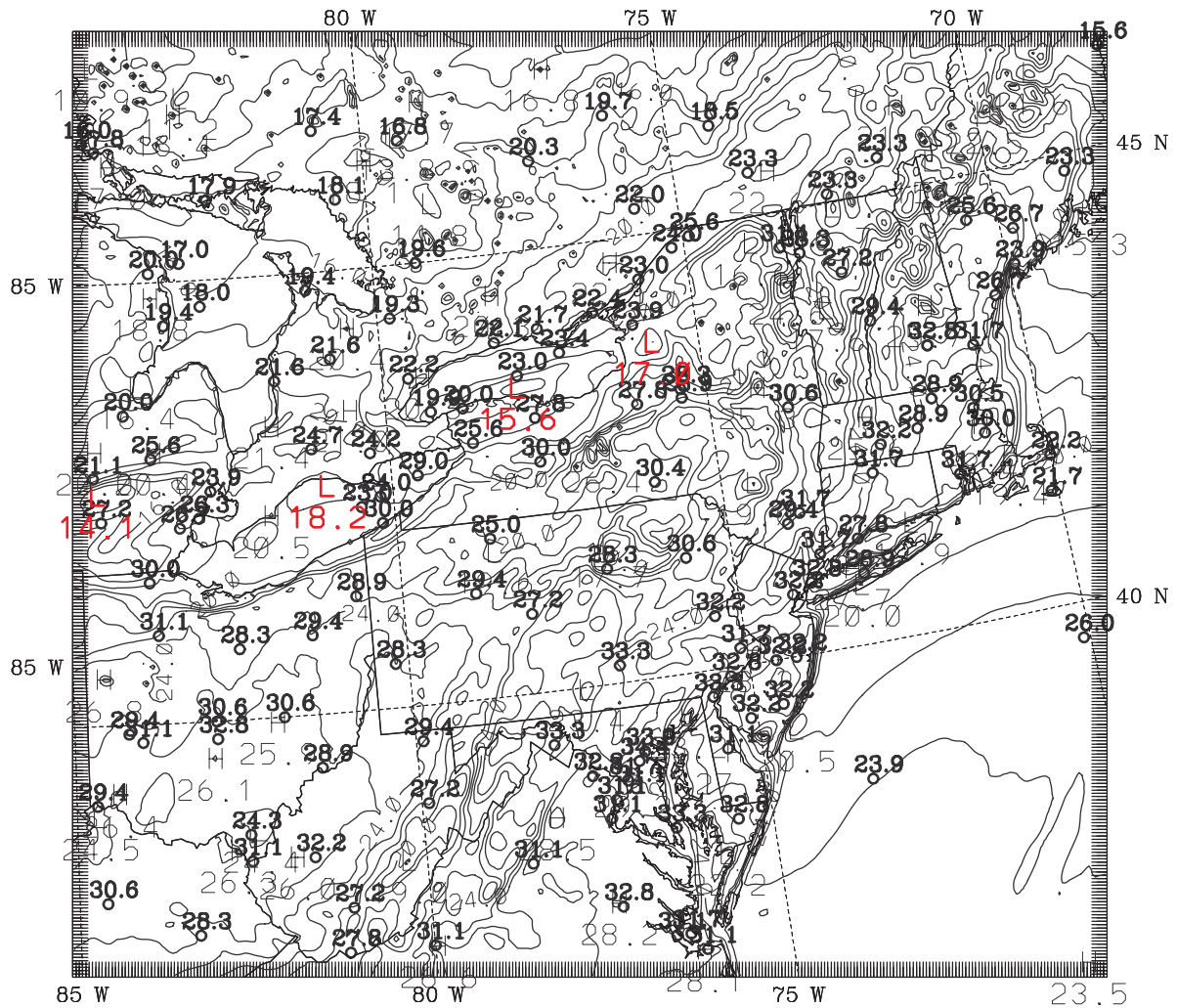
a)

Figure 19 Model-simulated fields at 30 h (1800 UTC 19 September 1983) on the 4-km domain in Exp. MS12KF. (a) 3-h total precipitation (mm), (b) Surface-layer wind overlaid with observed surface winds ( $\text{ms}^{-1}$ ), and (c) Surface-layer temperature overlaid with observed surface temperature ( $^{\circ}\text{C}$ ). Rain contours are 1, 5, 10 and 25 mm, speed contours are  $5 \text{ ms}^{-1}$  and one barb is  $10 \text{ ms}^{-1}$ , and temperature contours are  $1^{\circ}\text{C}$ . Heavy dashed lines are used to illustrate wind-shift lines likely associated with convective outflow boundaries and precipitation-induced cold pools. A red L and temperature value ( $^{\circ}\text{C}$ ) is used to denote a surface cold pool (i.e., a surface-layer temperature minimum located within or near a model-precipitation region).



b)  
MM5V3-CAPTEX, MS12KF, 4km, KF2, Eta PBL, No FDFA

Figure 19 (Continued)

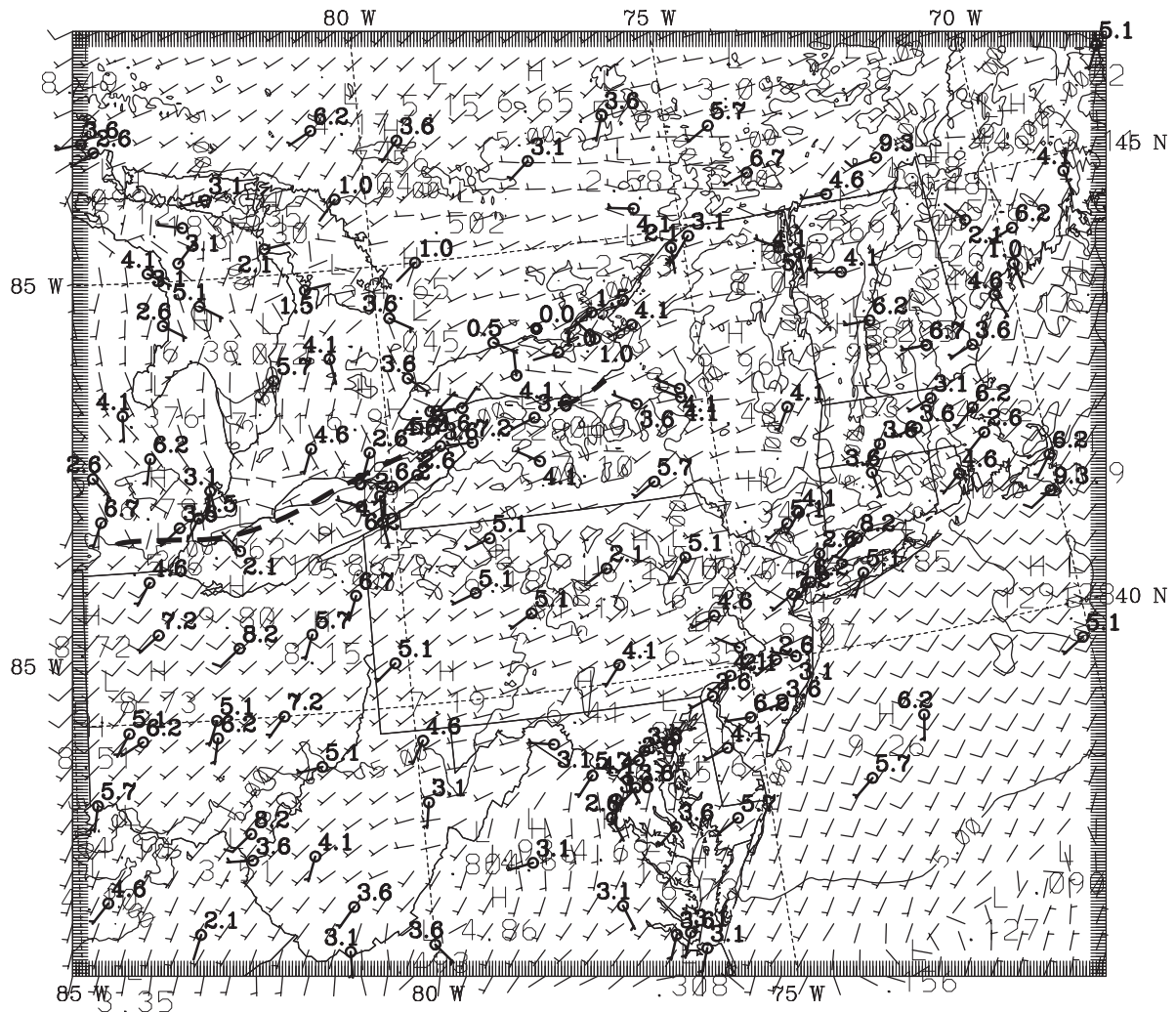


c)

Figure 19 (Continued)



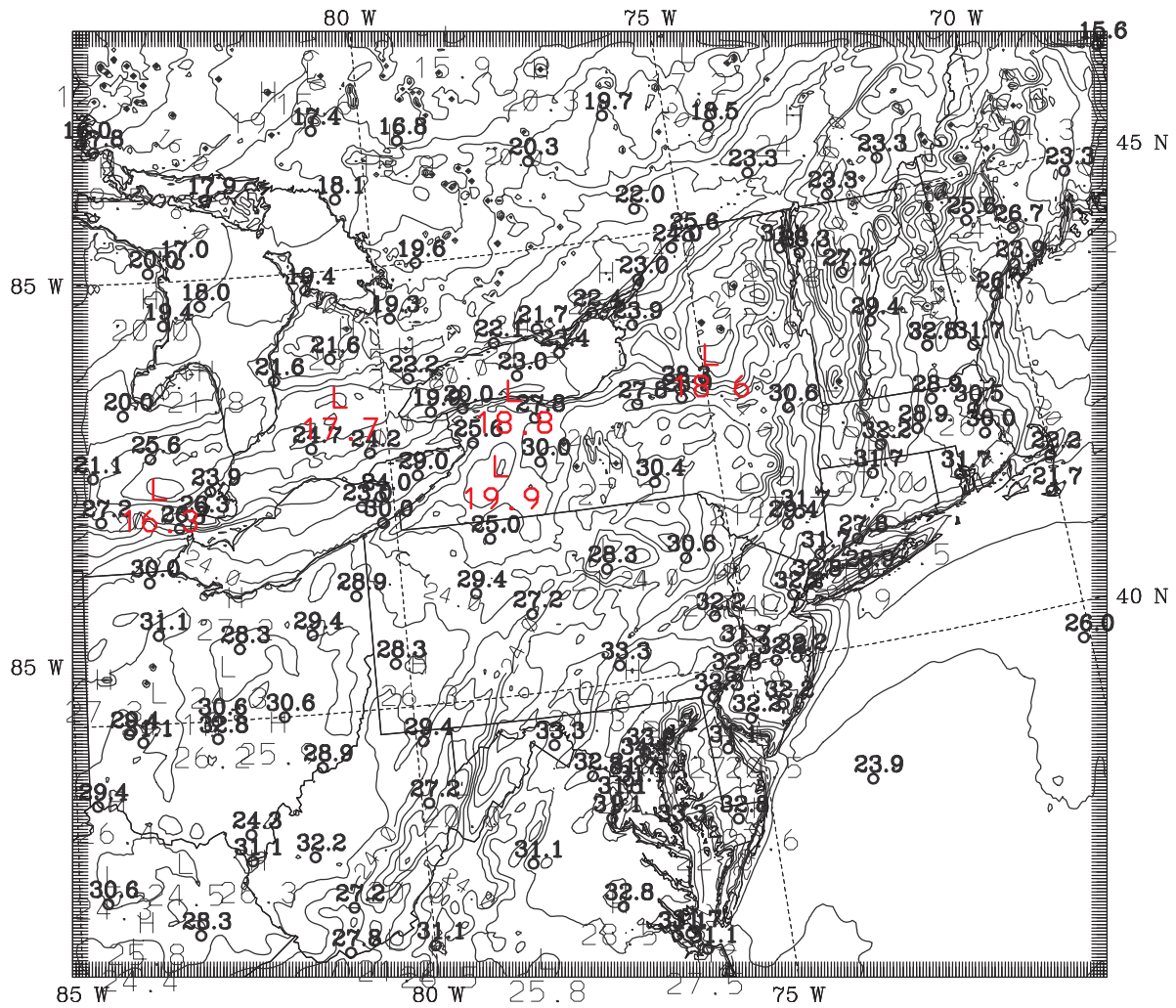




WRF-CAPTEX, WB2KF, 4km, KF2, Eta PBL

b)

Figure 20 (Continued)



WRF-CAPTEX, WB2KF, 4km, KF2, Eta PBL  
 CONTOUR FROM 12.000 TO 28.000 CONTOUR INTERVAL OF 1.0000 PT(3,3)= 25.036

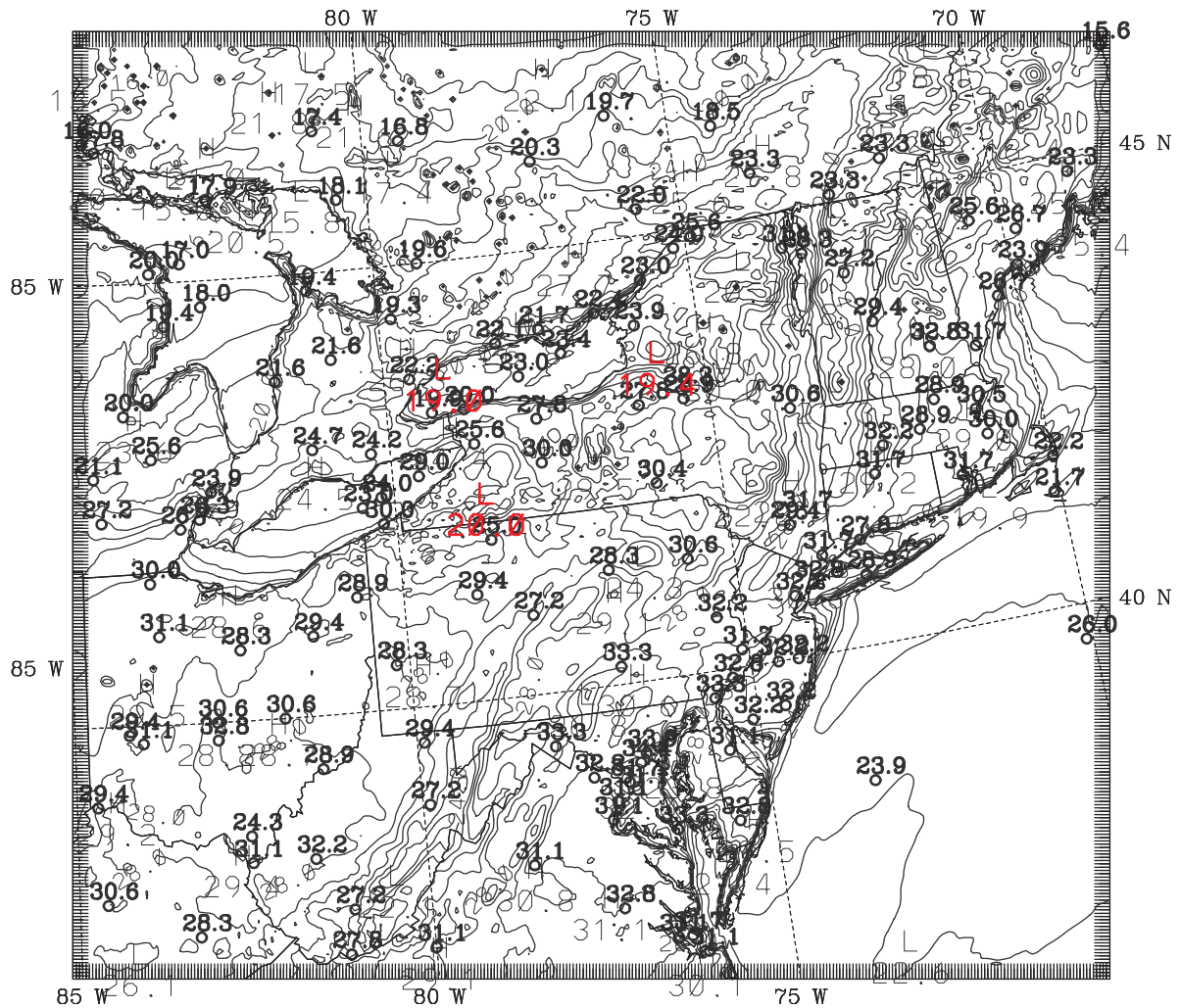
c)

Figure 20 (Continued)





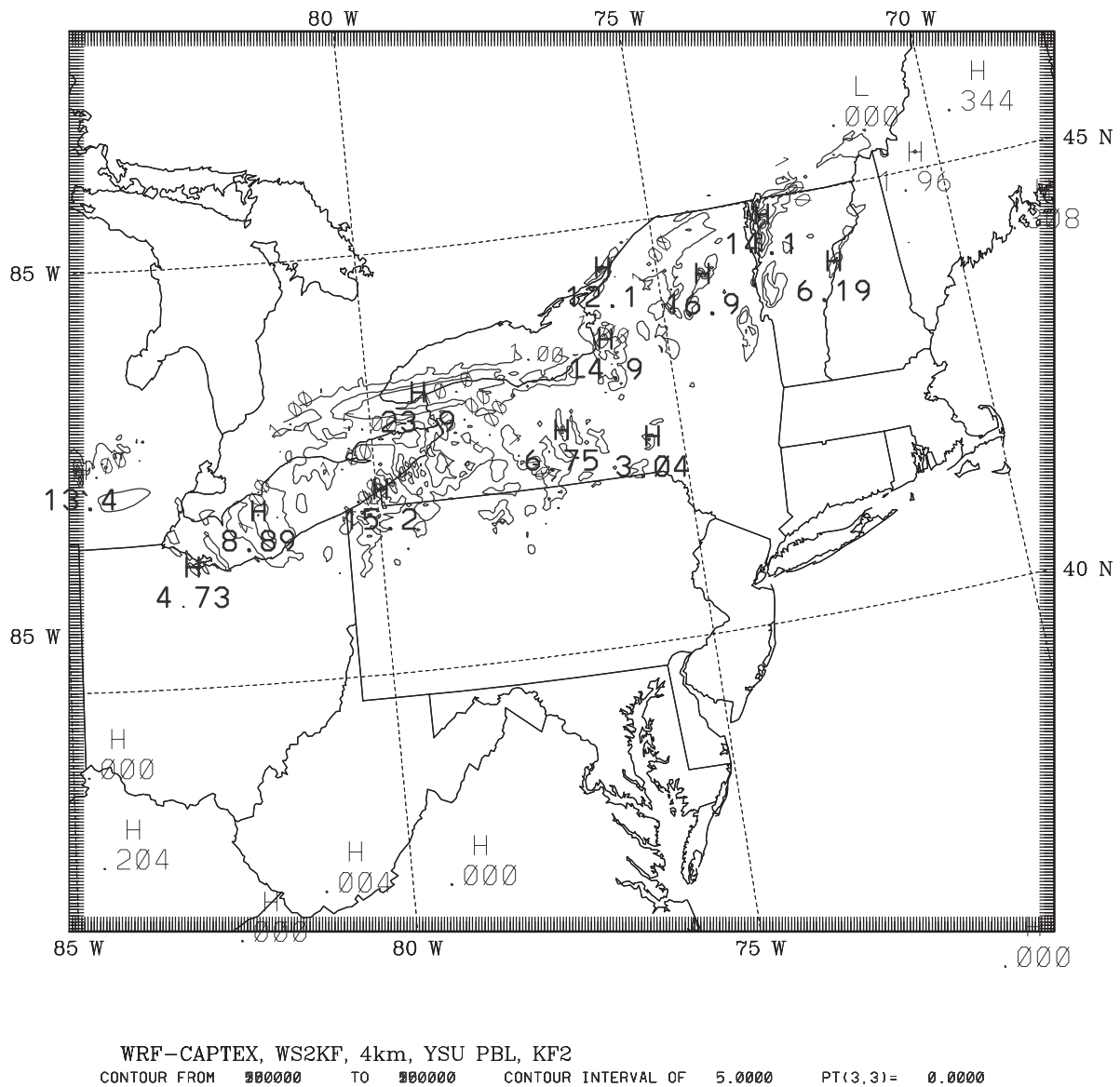




WRF-CAPTEX, WS2, 4km, YSU PBL, no CPS  
 CONTOUR FROM 13.000 TO 31.000 CONTOUR INTERVAL OF 1.0000 PT(3,3)= 27.454

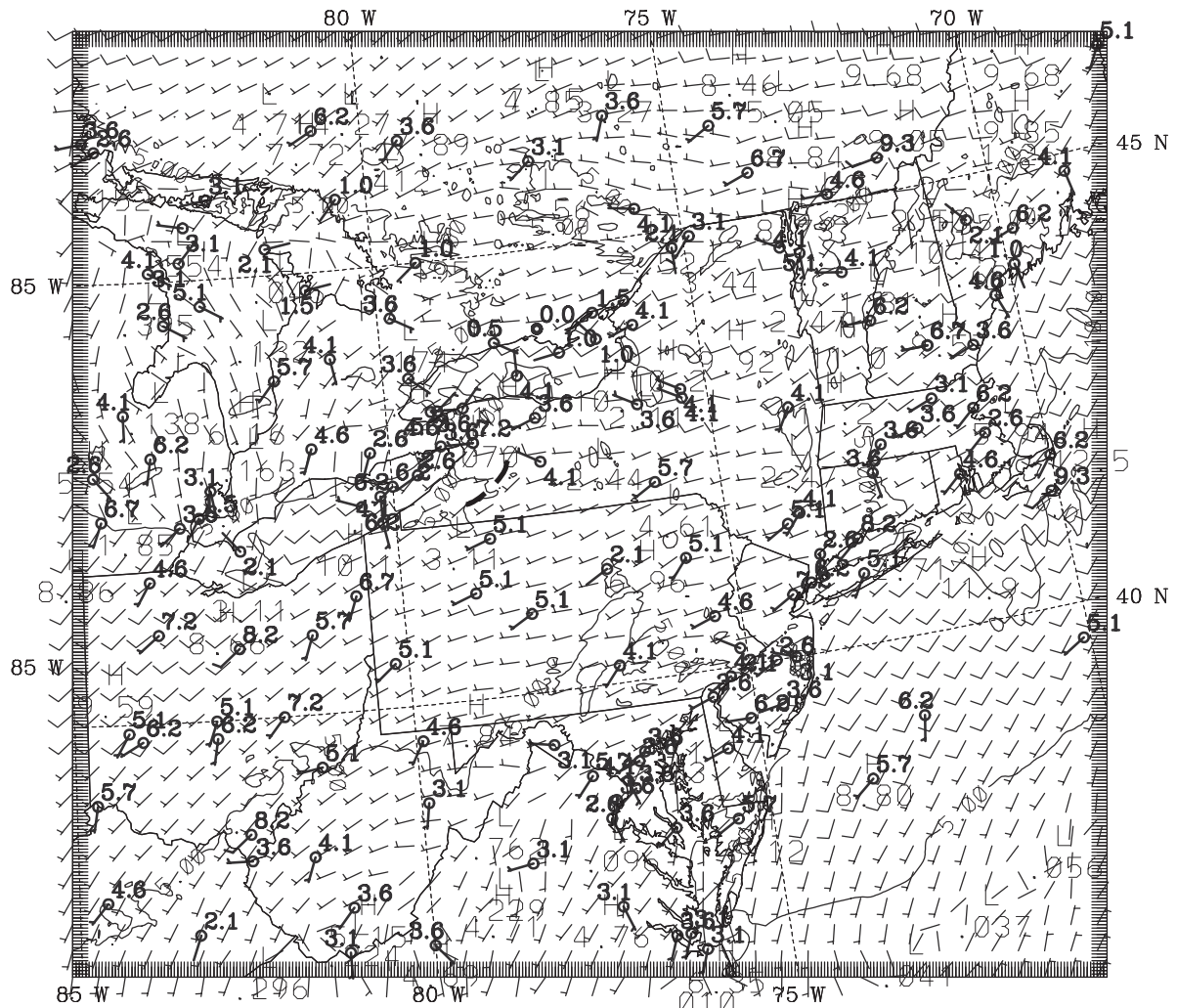
c)

Figure 21 (Continued)



a)

Figure 22 Model-simulated fields at 30 h (1800 UTC 19 September 1983) on the 4-km domain in Exp. WS2KF. (a) 3-h total precipitation (mm), (b) Surface-layer wind overlaid with observed surface winds ( $\text{ms}^{-1}$ ), and (c) Surface-layer temperature overlaid with observed surface temperature ( $^{\circ}\text{C}$ ). Rain contours are 1, 5, 10 and 25 mm, speed contours are  $5 \text{ ms}^{-1}$  and one barb is  $10 \text{ ms}^{-1}$ , and temperature contours are  $1^{\circ}\text{C}$ . Heavy dashed lines are used to illustrate wind-shift lines likely associated with convective outflow boundaries and precipitation-induced cold pools. A red L and temperature value ( $^{\circ}\text{C}$ ) is used to denote a surface cold pool (i.e., a surface-layer temperature minimum located within or near a model-precipitation region).

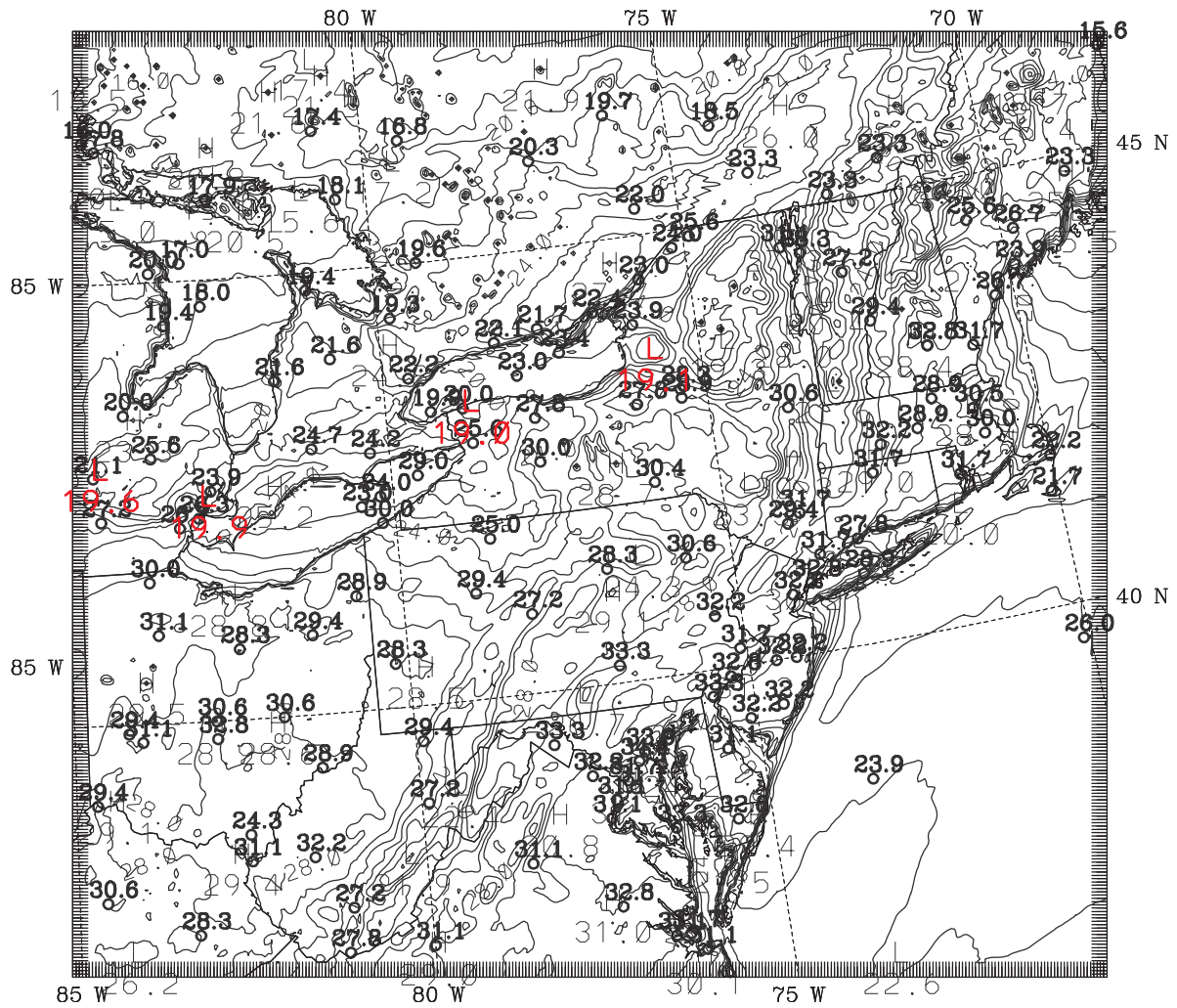


WRF-CAPTEX, WS2KF, 4km, YSU PBL, KF2

b)

Figure 22 (Continued)





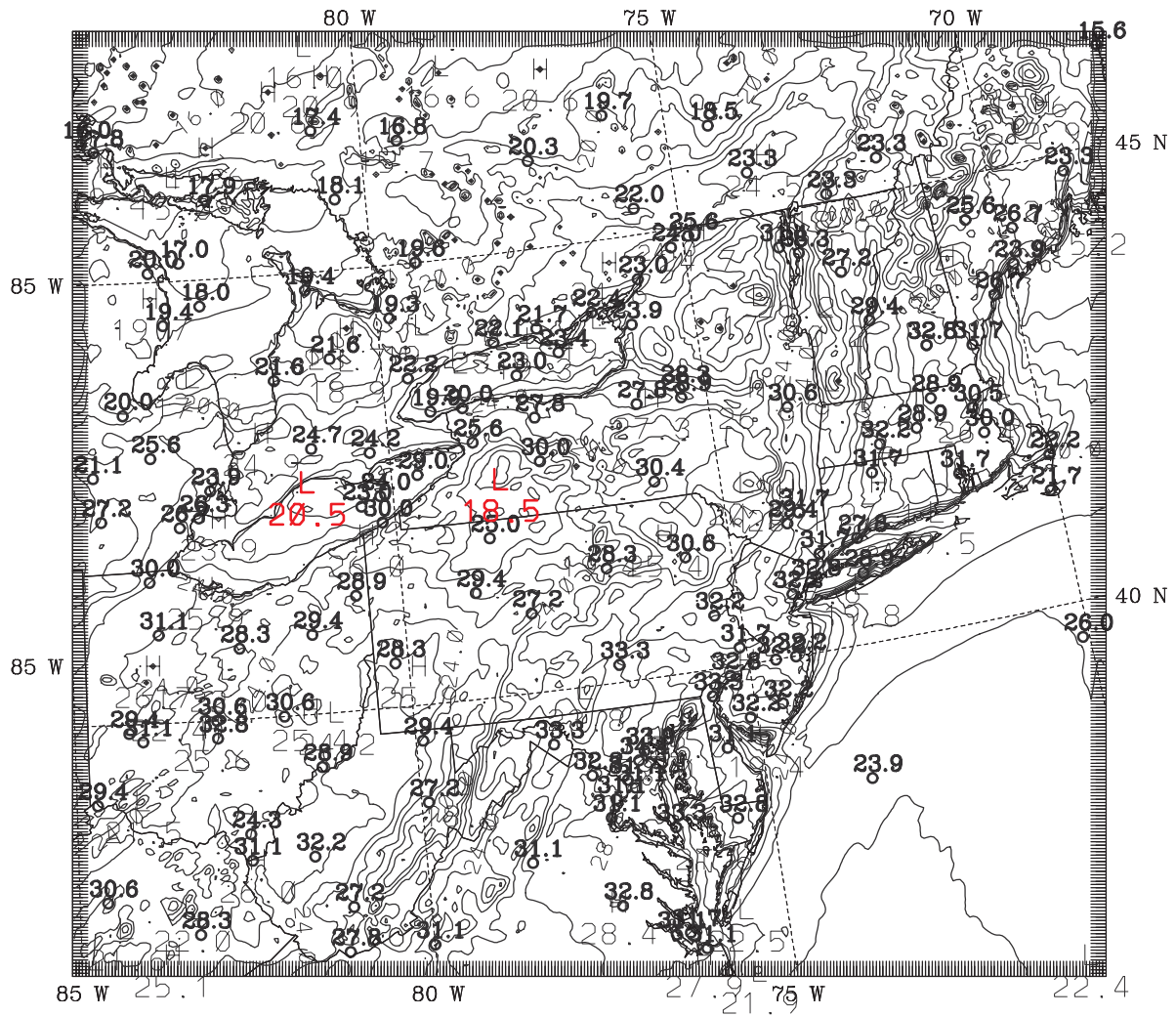
WRF-CAPTEX, WS2KF, 4km, YSU PBL, KF2  
 CONTOUR FROM 13.000 TO 31.000 CONTOUR INTERVAL OF 1.0000 PT(3,3)= 27.453

c)

Figure 22 (Continued)





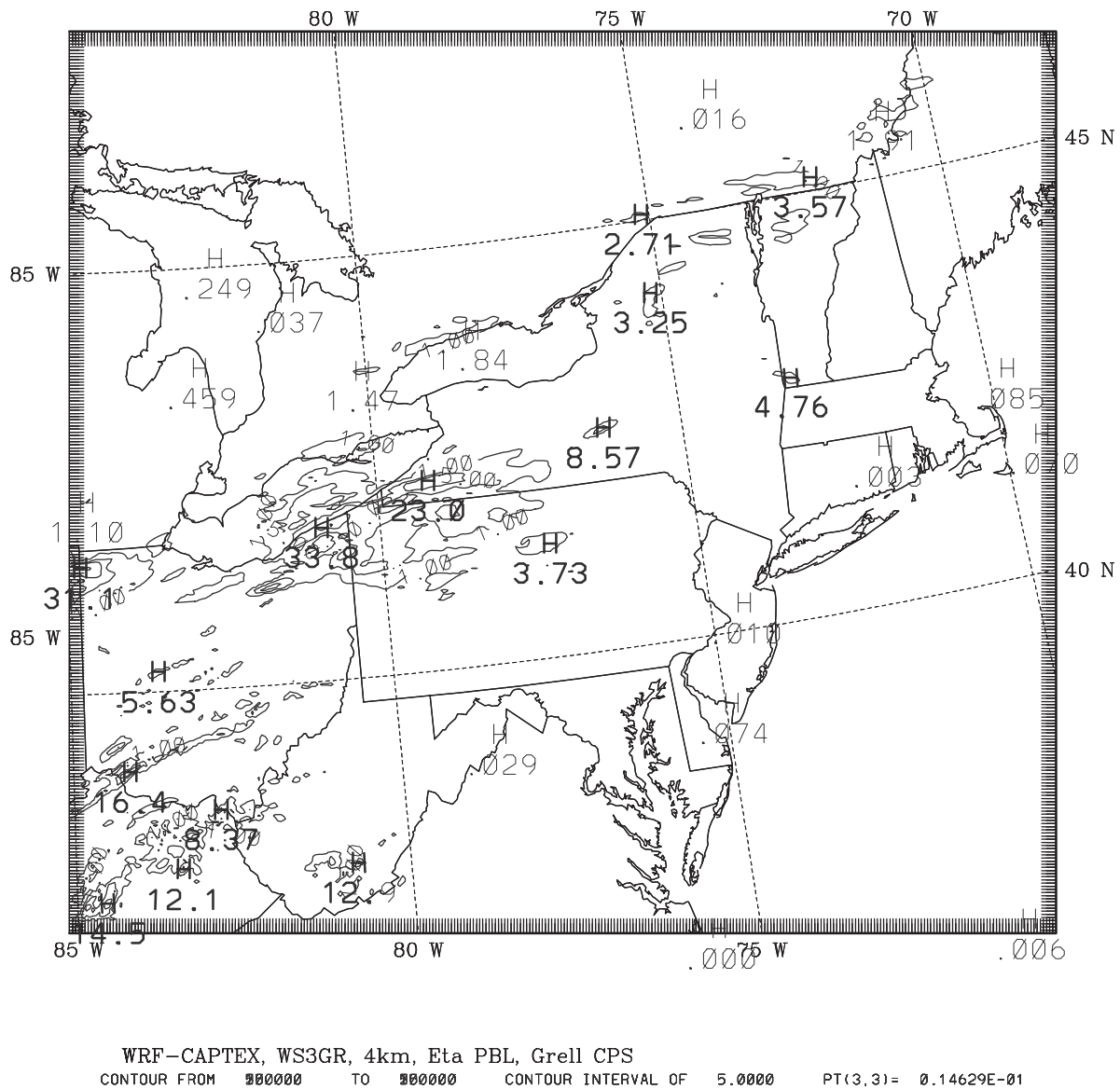


WRF-CAPTEX, WS3, 4km, Eta PBL, no CPS (Grell on upper meshes)  
 CONTOUR FROM 12.000 TO 29.000 CONTOUR INTERVAL OF 1.0000 PT(3,3)= 24.187

c)

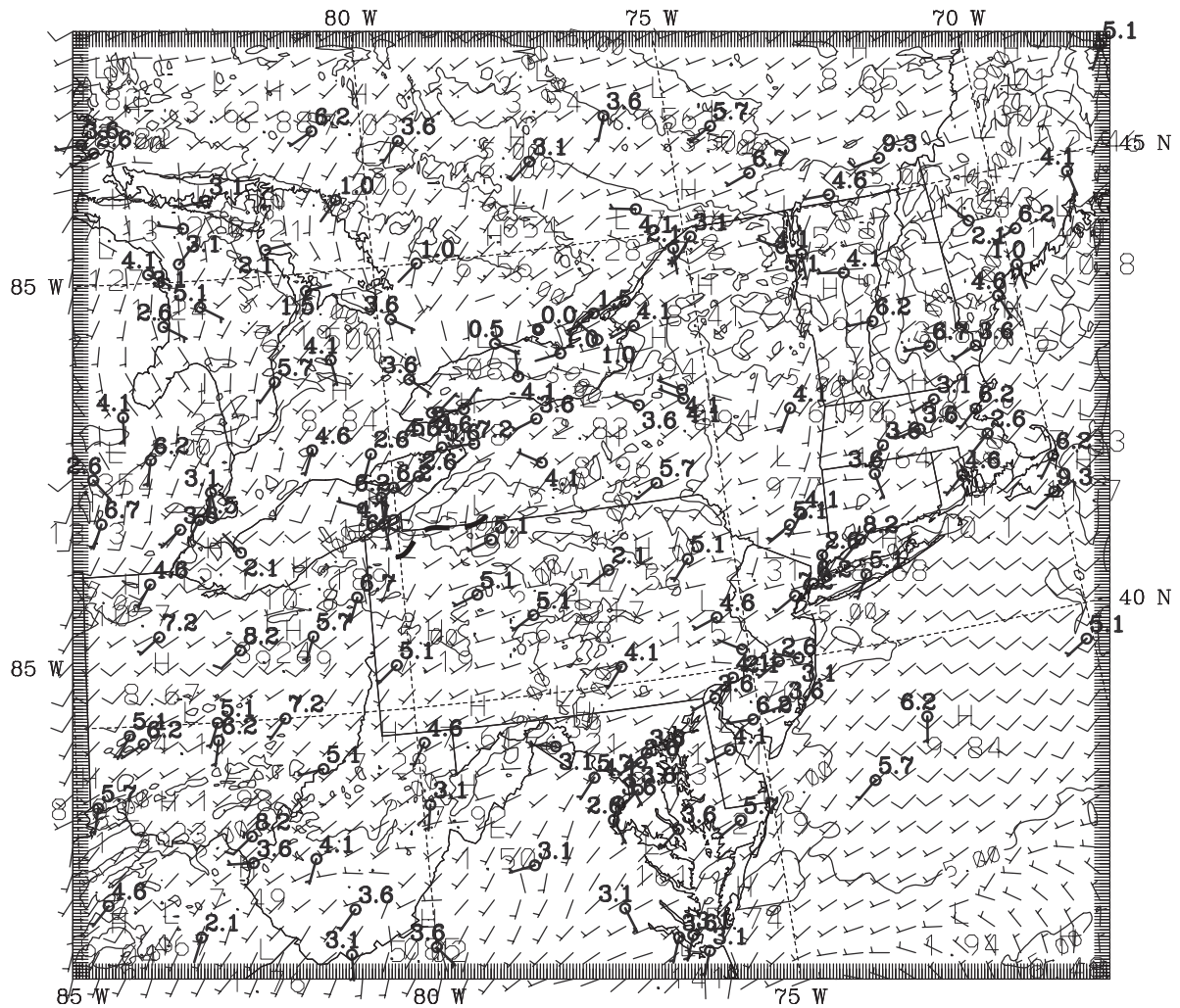
Figure 23 (Continued)





a)

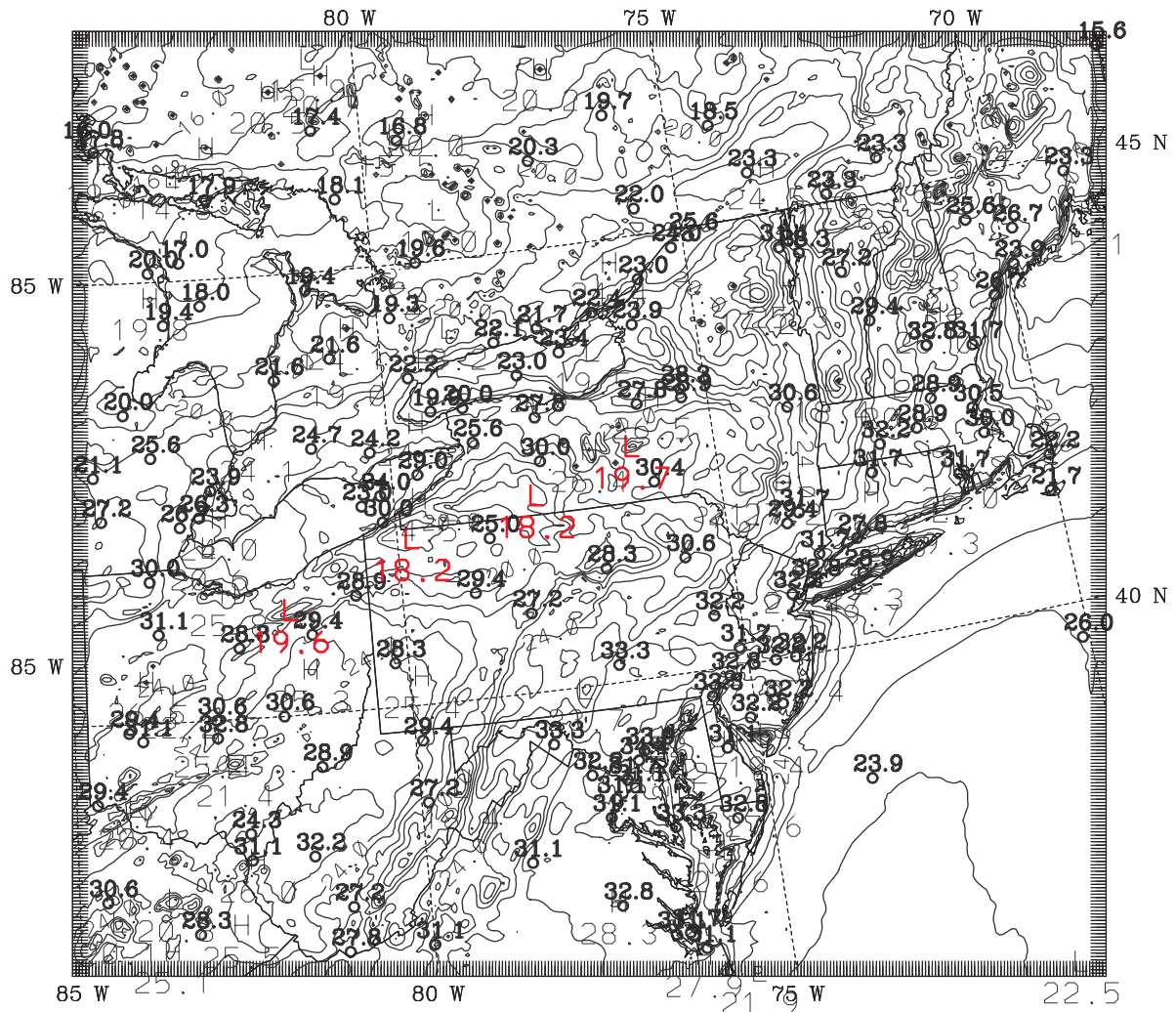
Figure 24 Model-simulated fields at 30 h (1800 UTC 19 September 1983) on the 4-km domain in Exp. WS3GR. (a) 3-h total precipitation (mm), (b) Surface-layer wind overlaid with observed surface winds ( $\text{ms}^{-1}$ ), and (c) Surface-layer temperature overlaid with observed surface temperature ( $^{\circ}\text{C}$ ). Rain contours are 1, 5, 10 and 25 mm, speed contours are  $5 \text{ ms}^{-1}$  and one barb is  $10 \text{ ms}^{-1}$ , and temperature contours are  $1^{\circ}\text{C}$ . Heavy dashed lines are used to illustrate wind-shift lines likely associated with convective outflow boundaries and precipitation-induced cold pools. A red L and temperature value ( $^{\circ}\text{C}$ ) is used to denote a surface cold pool (i.e., a surface-layer temperature minimum located within or near a model-precipitation region).



WRF-CAPTEX, WS3GR, 4km, Eta PBL, Grell CPS

b)

Figure 24 (Continued)



c)

Figure 24 (Continued)

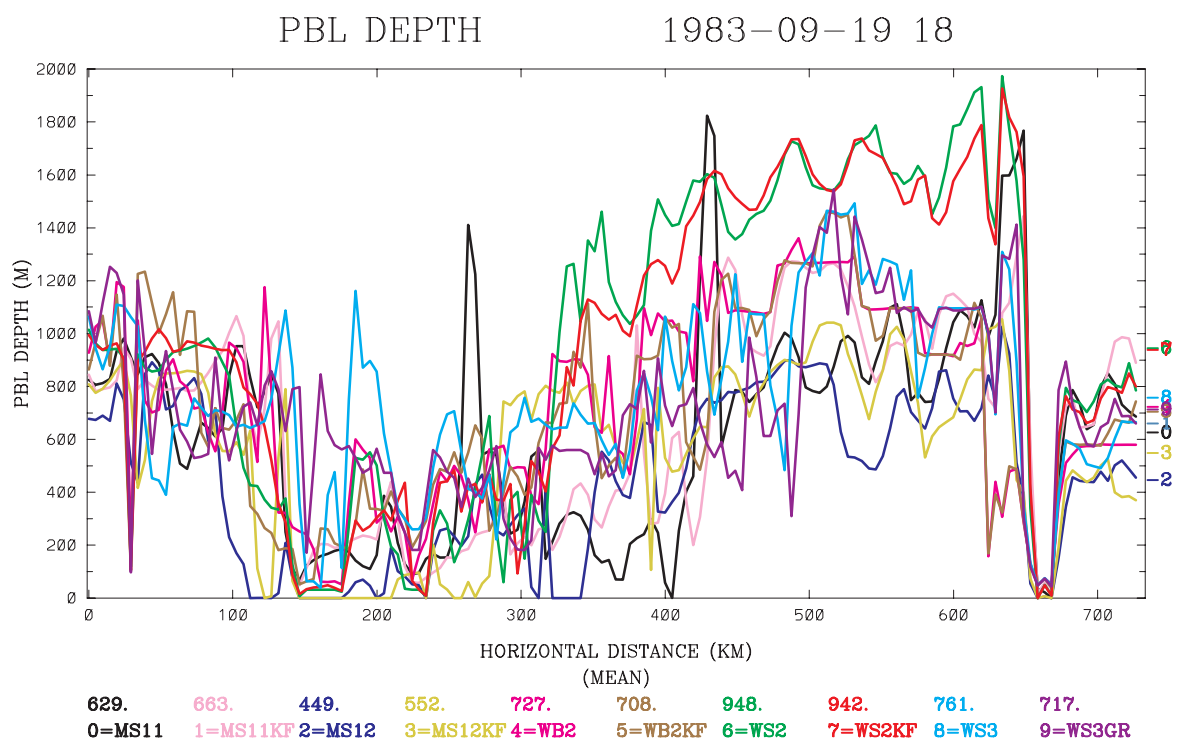


Figure 25 MM5- and WRF-simulated PBL height (m) along the northwest-southeast cross section shown in Fig. 3 for all experiments on the 4-km resolution domain at 30 h (1800 UTC 19 September 1983). The cross-section mean PBL height values are plotted on the right side of the chart with the digital values also included above the experiment key at the bottom of the figure.



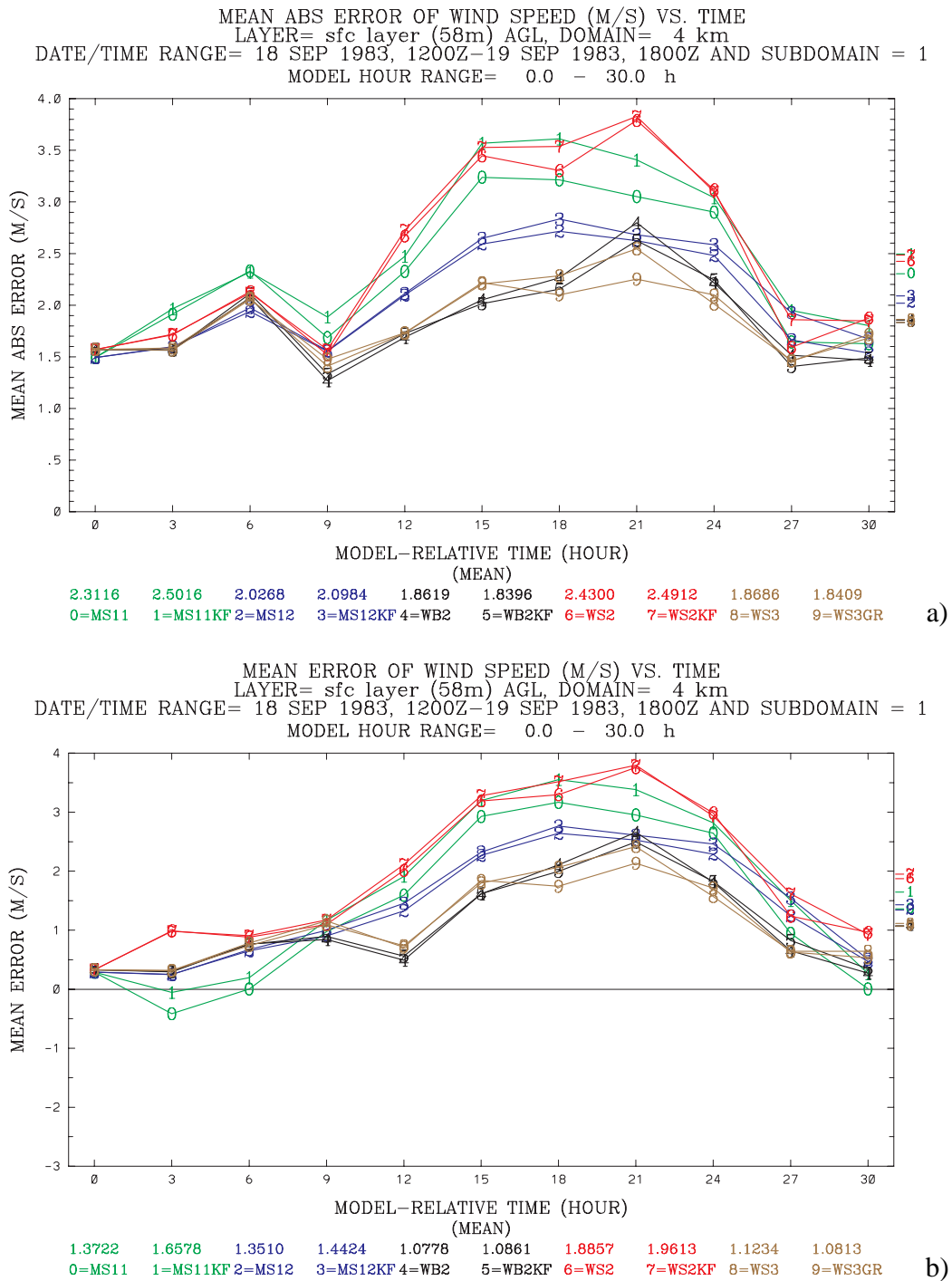
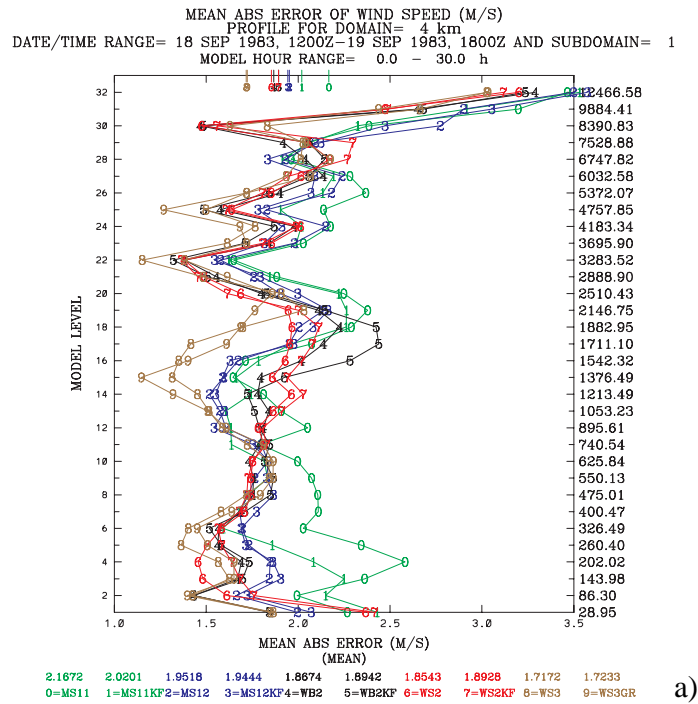
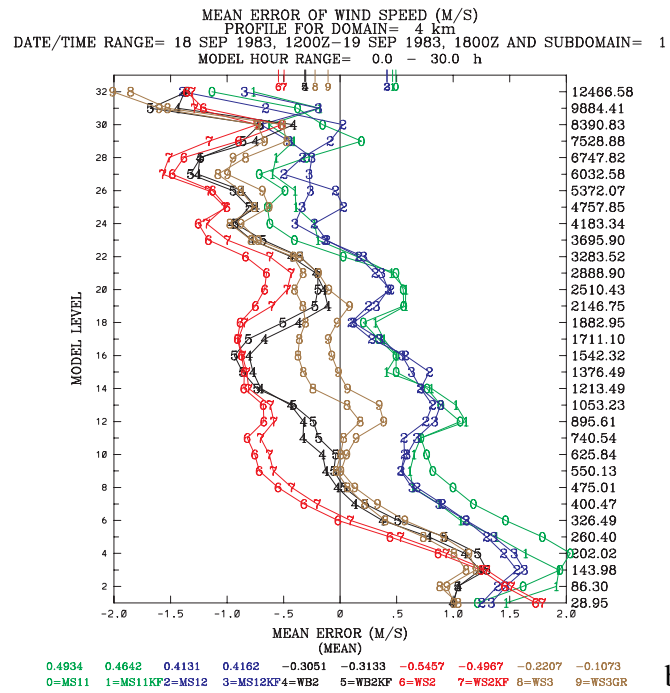


Figure 26 Model-simulated surface-layer wind speed statistics ( $\text{ms}^{-1}$ ) on the 4-km domain from 1200 UTC 18 September – 1800 UTC 19 September 1983 for all experiments. a) mean absolute error (MAE), and b) mean error (ME) . The 30-hour mean statistics are plotted on the right side of the chart with the digital values also included above the experiment key at the bottom of the figure.



a)



b)

Figure 27 Model-simulated vertical profile wind speed statistics ( $\text{ms}^{-1}$ ) on the 4-km domain from 1200 UTC 18 September – 1800 UTC 19 September 1983 for all experiments. a) mean absolute error (MAE), and b) mean error (ME). The 32-layer mean statistics are plotted on the top of the chart with the digital values also included above the experiment key at the bottom of the figure.

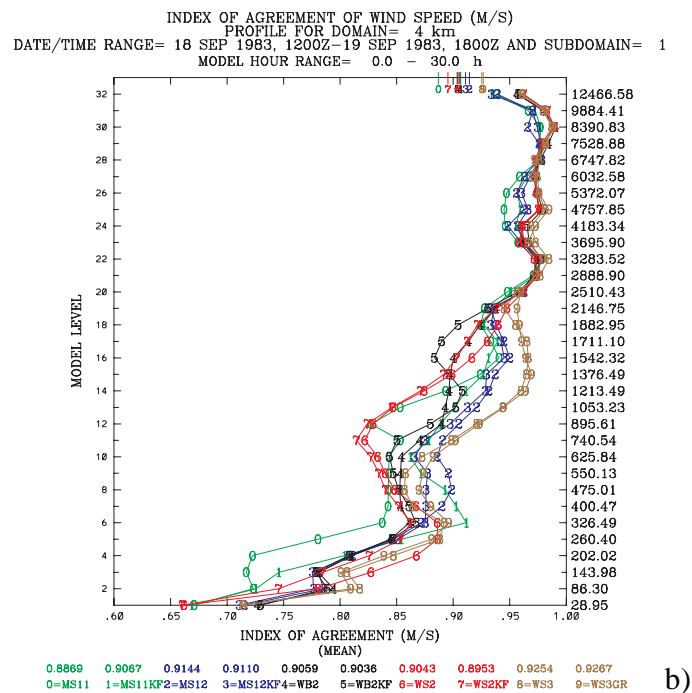
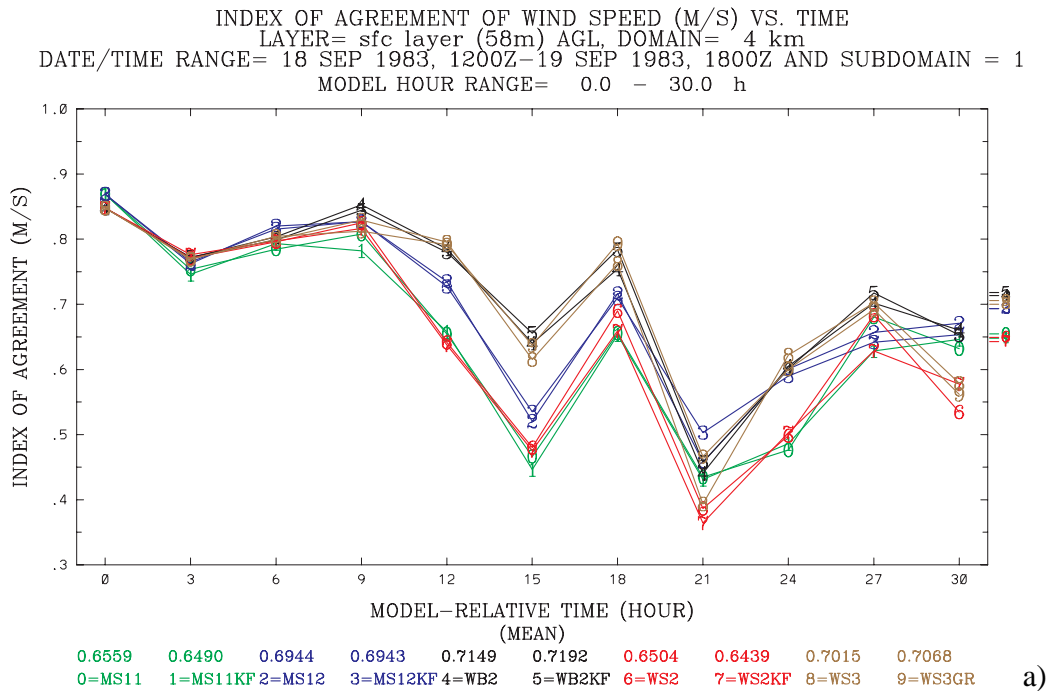
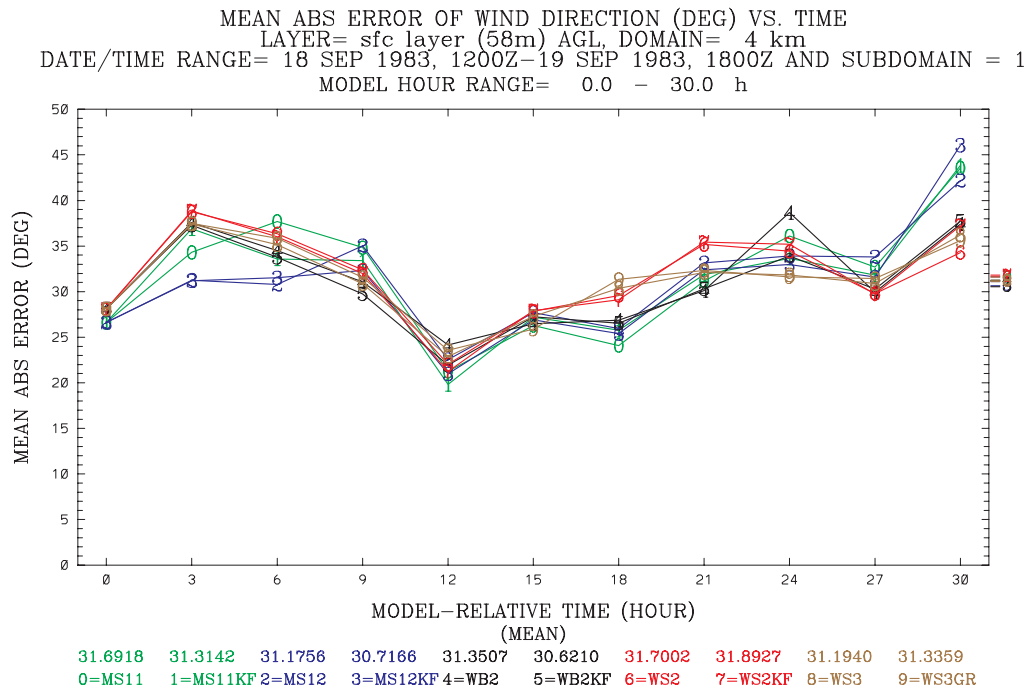
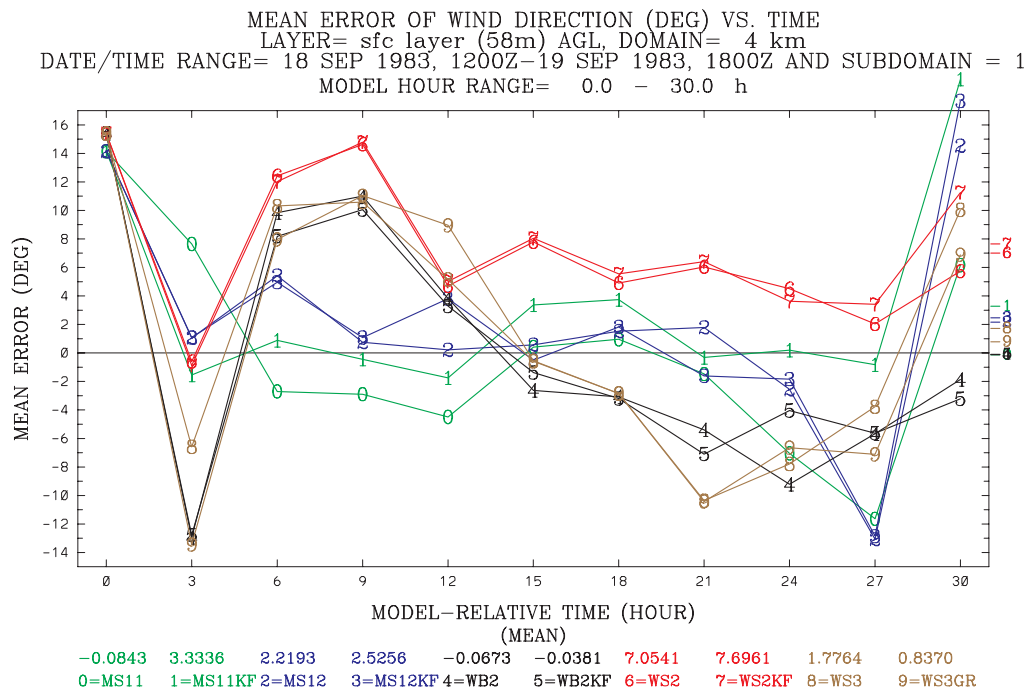


Figure 28 Model-simulated index of agreement (fraction) on the 4-km domain for wind speed for all experiments, a) Surface-layer value from 1200 UTC 18 September – 1800 UTC 19 September 1983 for all experiments, b) vertical profile of the 30-h averaged value. The mean statistics are plotted at the top of the chart with the digital values also included above the experiment key at the bottom of the figure.



a)



b)

Figure 29

Model-simulated surface-layer wind direction statistics (deg) on the 4-km domain from 1200 UTC 18 September – 1800 UTC 19 September 1983 for all experiments. a) mean absolute error (MAE), and b) mean error (ME) . The 30-hour mean statistics are plotted on the right side of the chart with the digital values also included above the experiment key at the bottom of the figure.

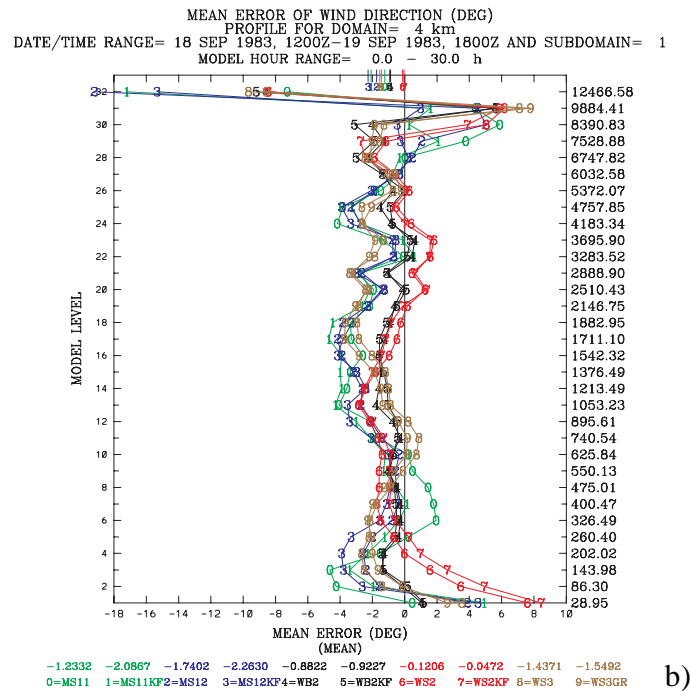
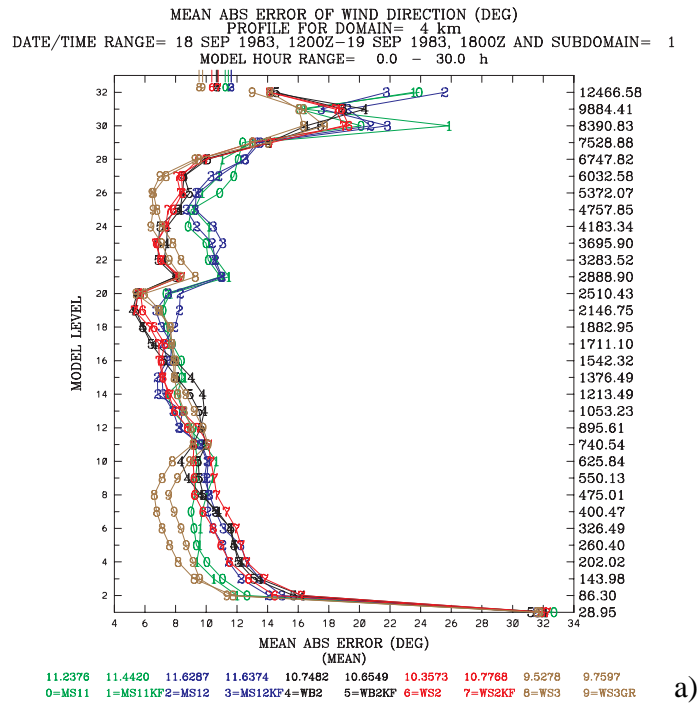


Figure 30 Model-simulated vertical profile wind direction statistics (deg) on the 4-km domain from 1200 UTC 18 September – 1800 UTC 19 September 1983 for all experiments. a) mean absolute error (MAE), and b) mean error (ME). The 32-layer mean statistics are plotted on the top of the chart with the digital values also included above the experiment key at the bottom of the figure.

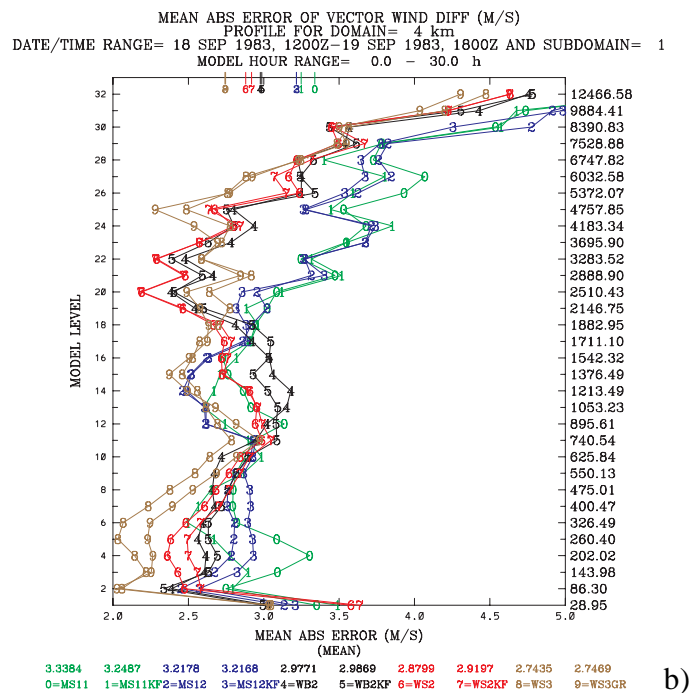
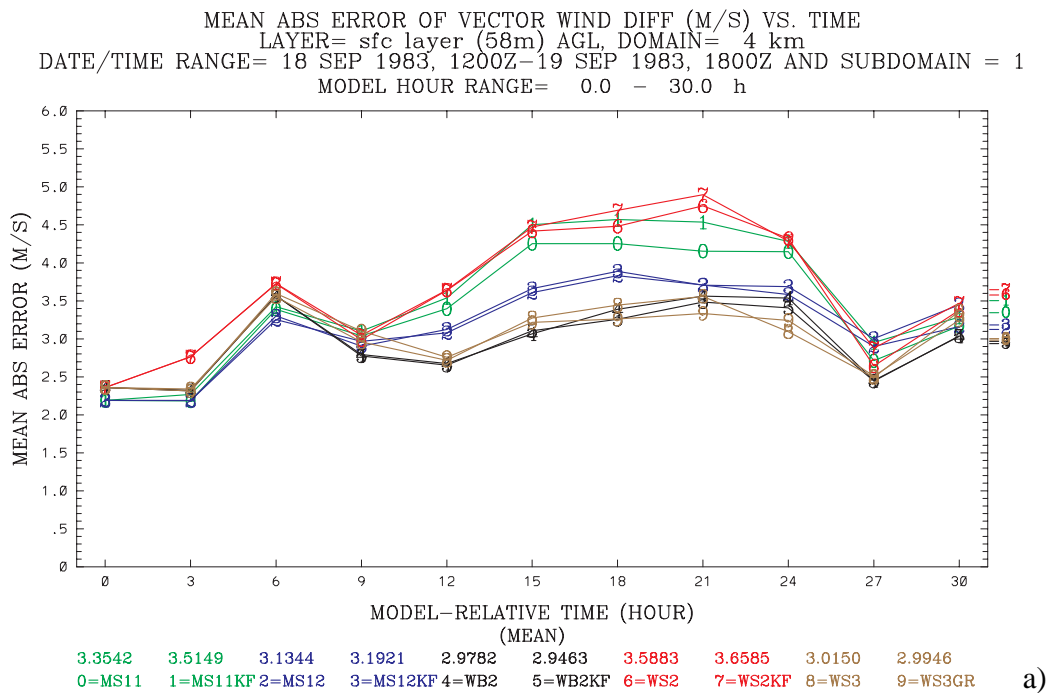
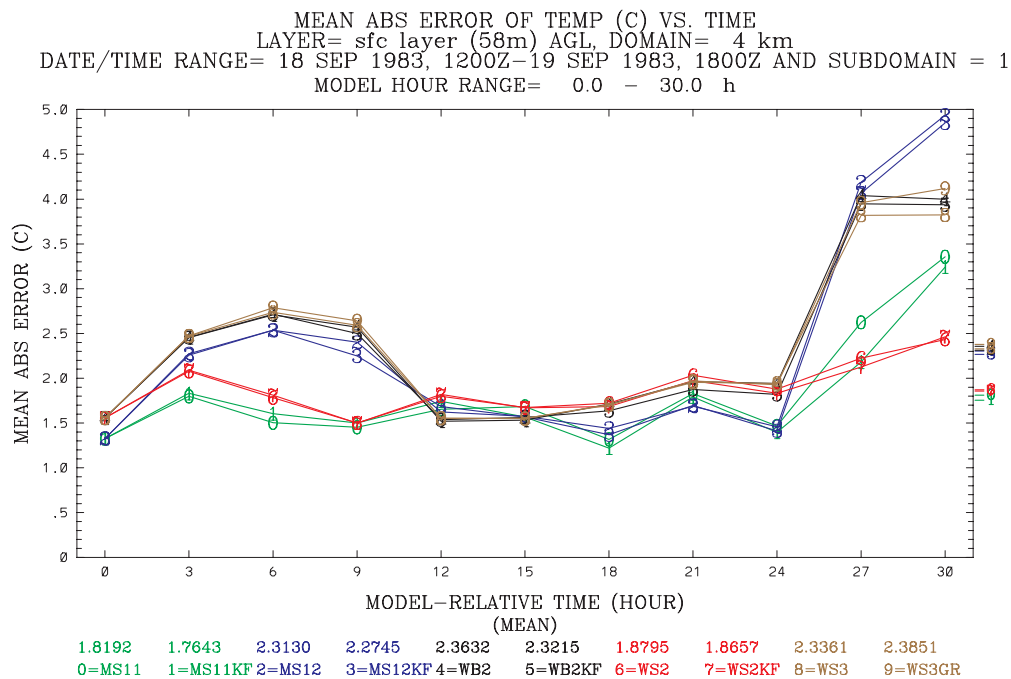
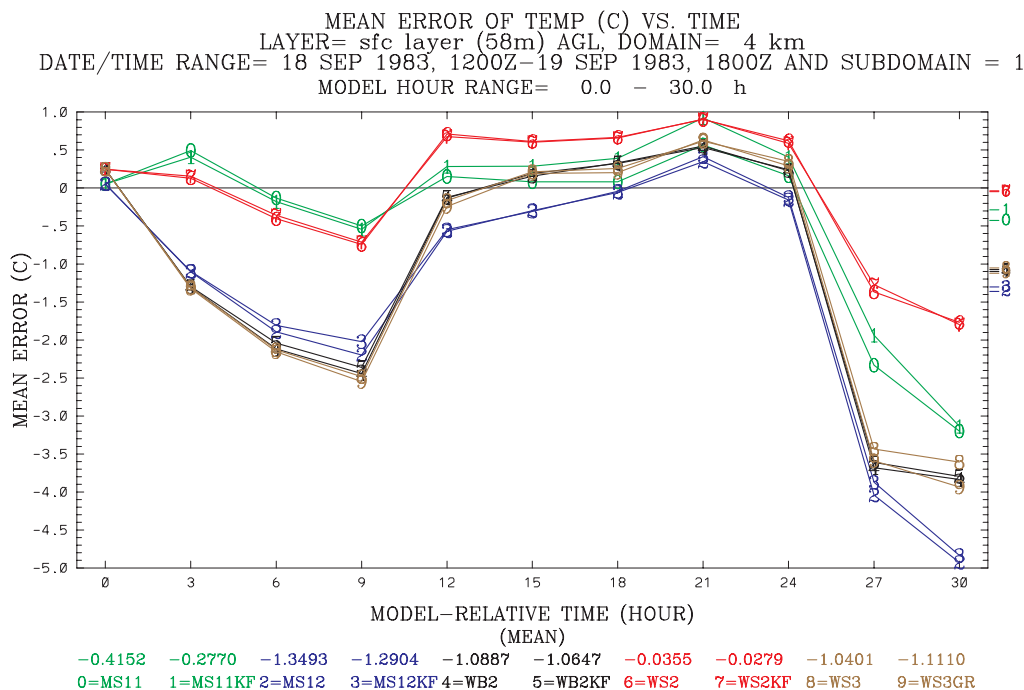


Figure 31 Model-simulated vector wind difference ( $\text{ms}^{-1}$ ) on the 4-km domain for all experiments, a) Surface-layer value from 1200 UTC 18 September – 1800 UTC 19 September 1983 for all experiments, b) vertical profile of the 30-h averaged value. The mean statistics are plotted at the top of the chart with the digital values also included above the experiment key at the bottom of the figure.

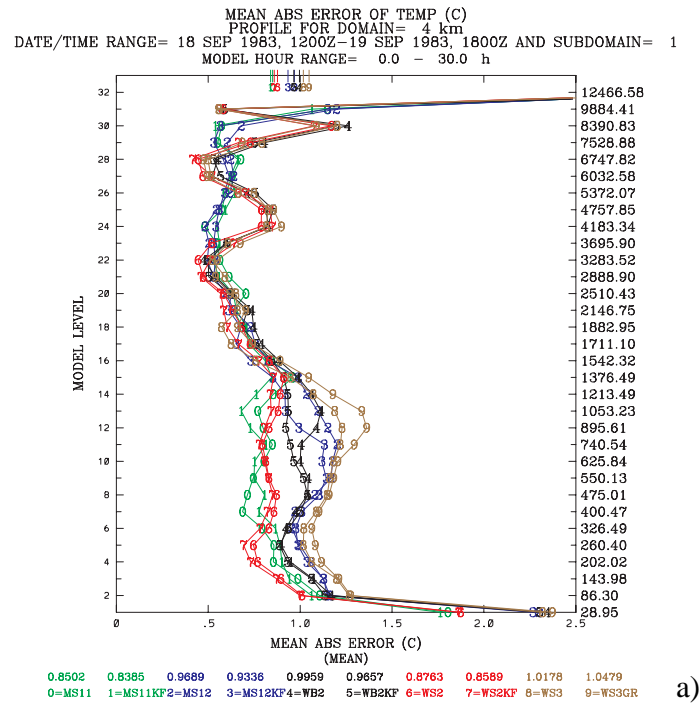


a)

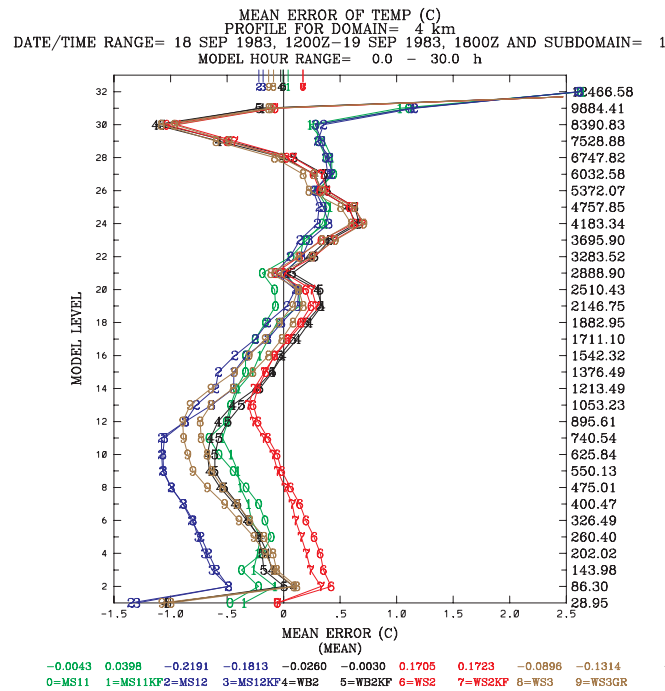


b)

Figure 32 Model-simulated surface-layer temperature statistics (C) on the 4-km domain from 1200 UTC 18 September – 1800 UTC 19 September 1983 for all experiments. a) mean absolute error (MAE), and b) mean error (ME) . The 30-hour mean statistics are plotted on the right side of the chart with the digital values also included above the experiment key at the bottom of the figure.



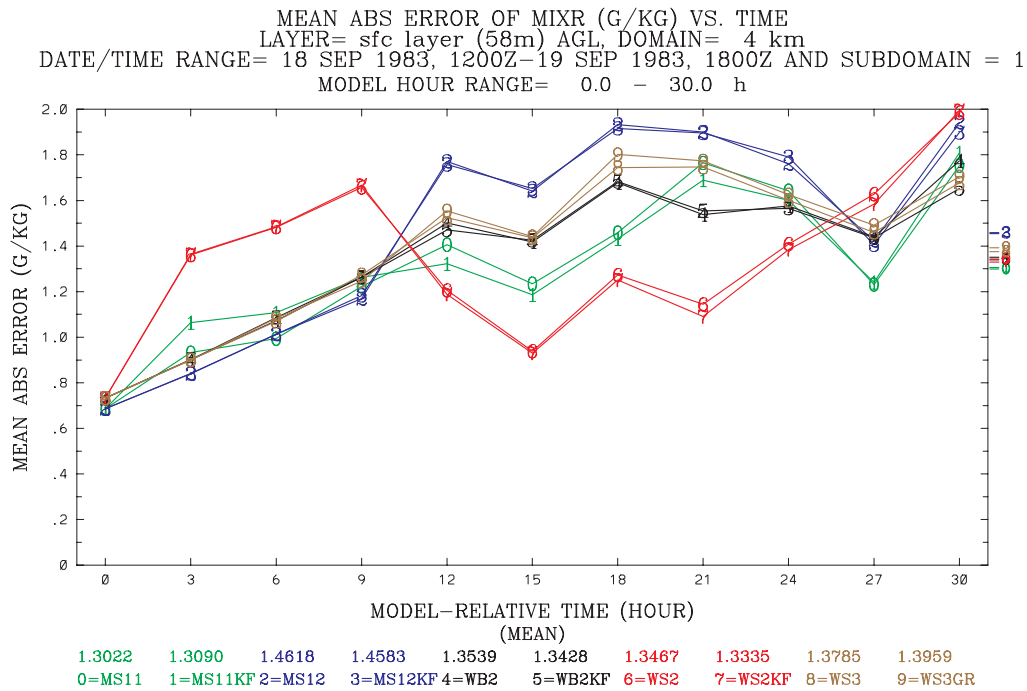
a)



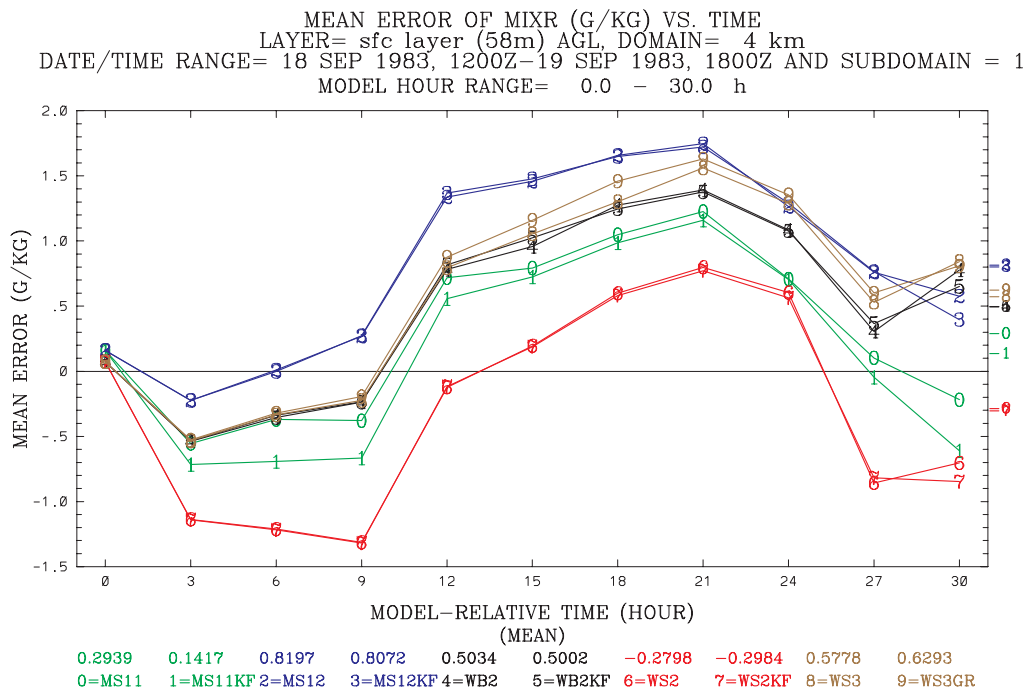
b)

Figure 33 Model-simulated vertical profile temperature statistics (C) on the 4-km domain from 1200 UTC 18 September – 1800 UTC 19 September 1983 for all experiments. a) mean absolute error (MAE), and b) mean error (ME). The 32-layer mean statistics are plotted on the top of the chart with the digital values also included above the experiment key at the bottom of the figure.





a)



b)

Figure 34

Model-simulated surface-layer vapor mixing ratio statistics ( $\text{g kg}^{-1}$ ) on the 4-km domain from 1200 UTC 18 September – 1800 UTC 19 September 1983 for all experiments. a) mean absolute error (MAE), and b) mean error (ME). The 30-hour mean statistics are plotted on the right side of the chart with the digital values also included above the experiment key at the bottom of the figure.

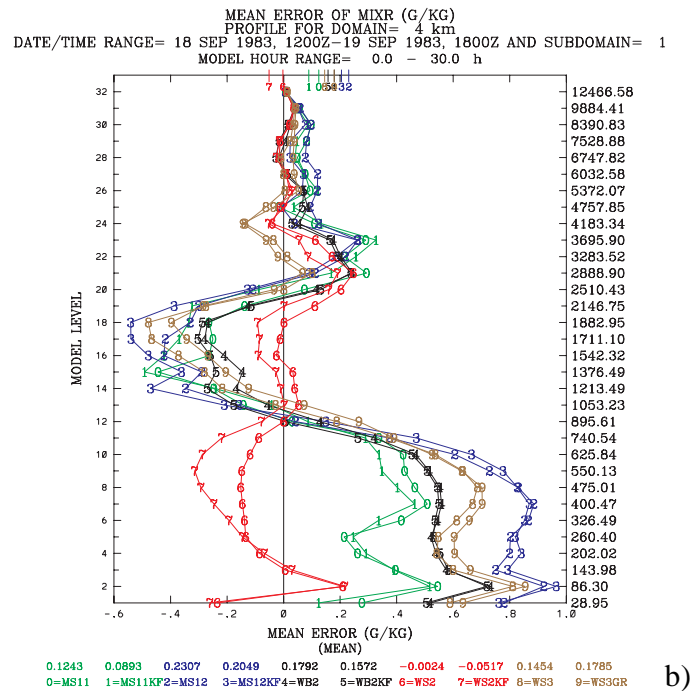
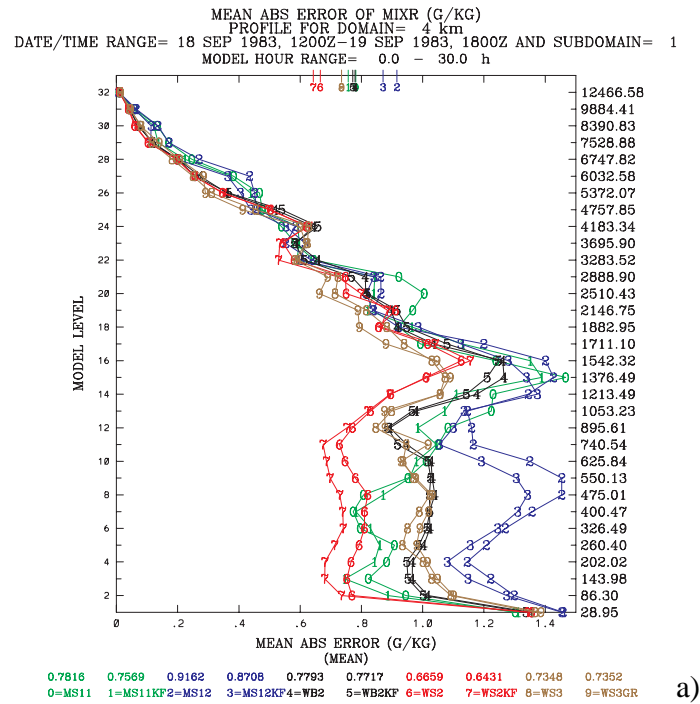
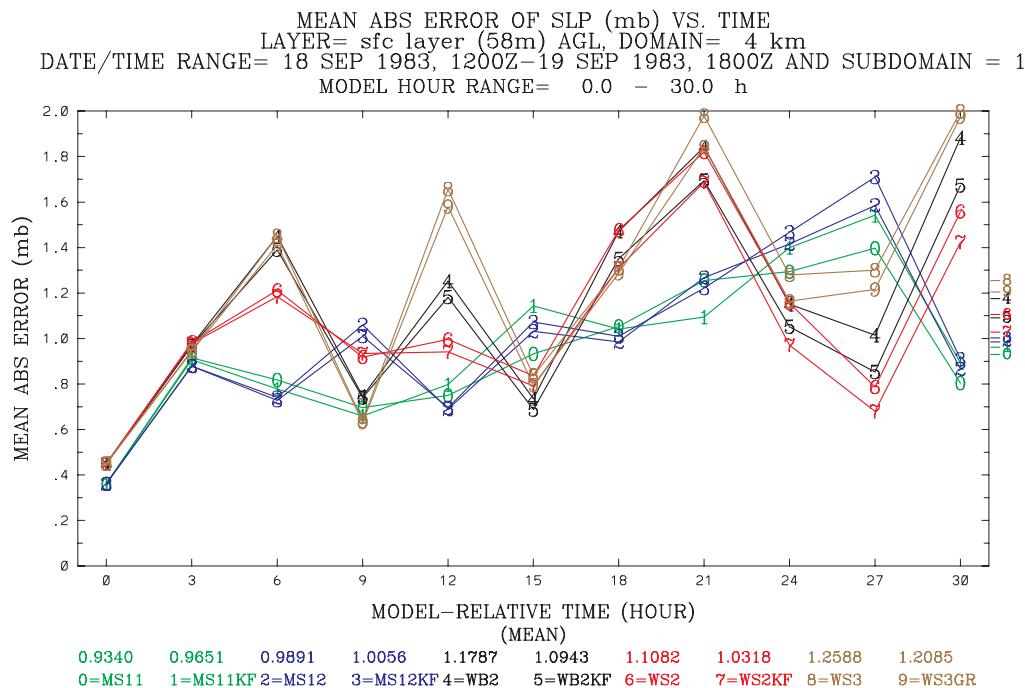
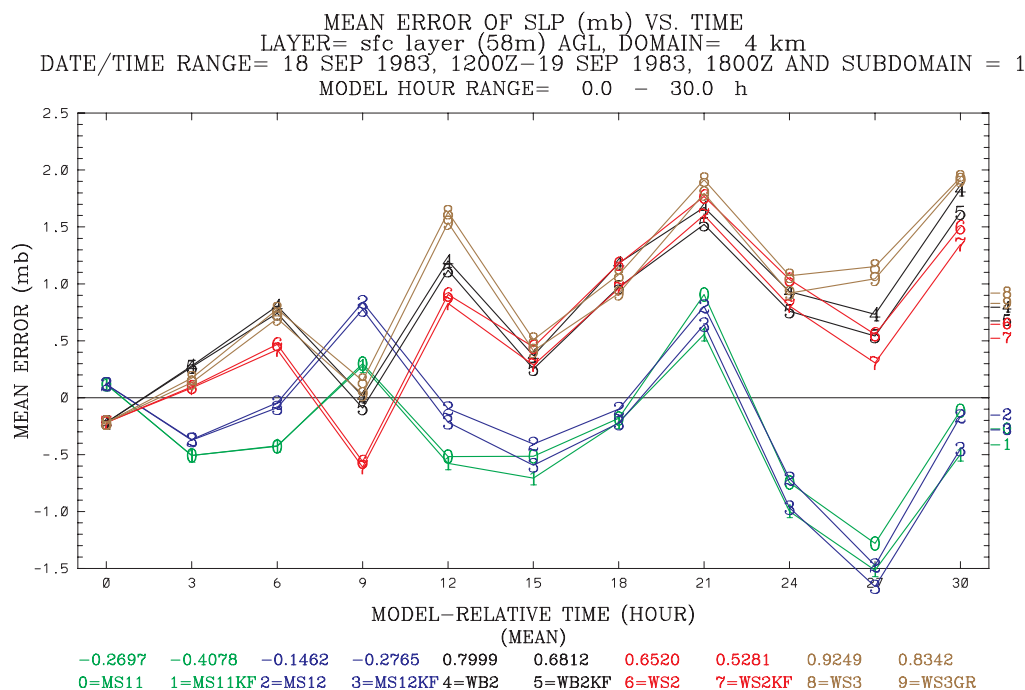


Figure 35 Model-simulated vertical profile vapor mixing ratio statistics ( $\text{g kg}^{-1}$ ) on the 4-km domain from 1200 UTC 18 September – 1800 UTC 19 September 1983 for all experiments. a) mean absolute error (MAE), and b) mean error (ME). The 32-layer mean statistics are plotted on the top of the chart with the digital values also included above the experiment key at the bottom of the figure.



a)



b)

Figure 36 Model-simulated sea-level pressure statistics (mb) on the 4-km domain from 1200 UTC 18 September – 1800 UTC 19 September 1983 for all experiments. a) mean absolute error (MAE), and b) mean error (ME) . The 30-hour mean statistics are plotted on the right side of the chart with the digital values also included above the experiment key at the bottom of the figure.

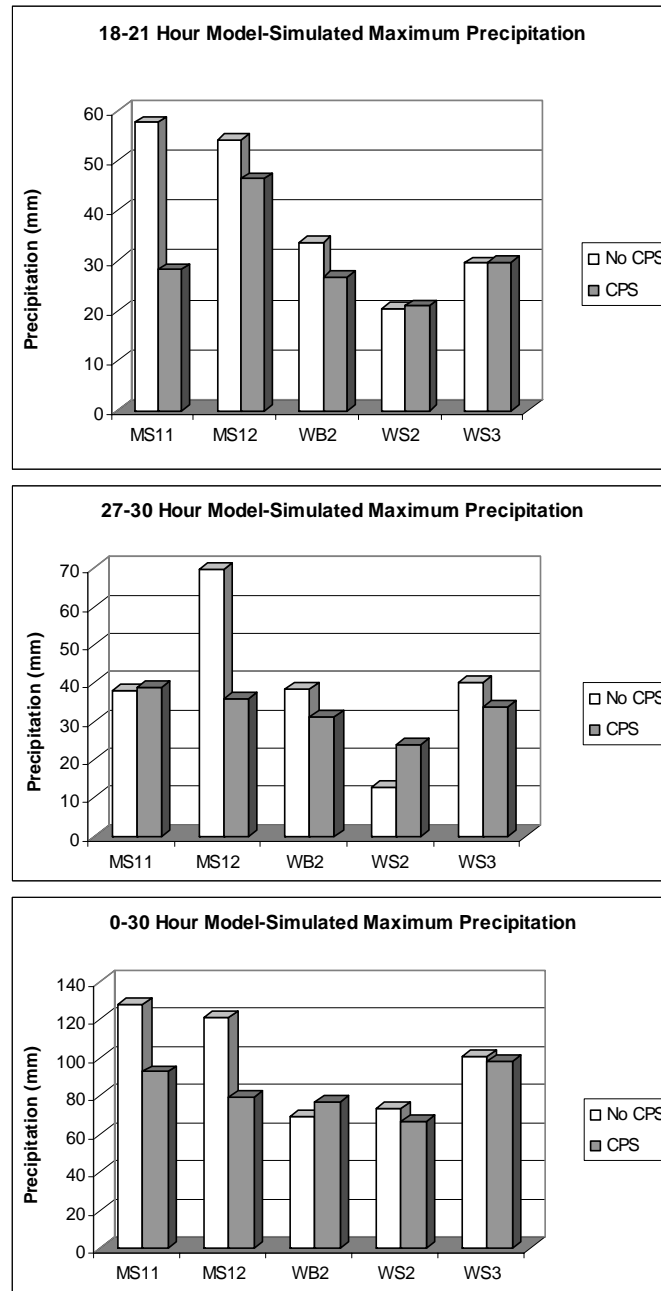


Figure 37 Maximum model-simulated precipitation amounts (mm) on the 4-km domain for all experiments with and without convective parameterization scheme (CPS), for the three-hour periods ending at 21 hours (0900 UTC 19 September 1983), and 30 hours (1800 UTC 19 September 1983), and the maximum total accumulated precipitation through the entire 30-hour period. These maximum values are computed from the sum of the parameterized subgrid precipitation (if a CPS is used) and the grid-resolved (explicit) precipitation for each model experiment.

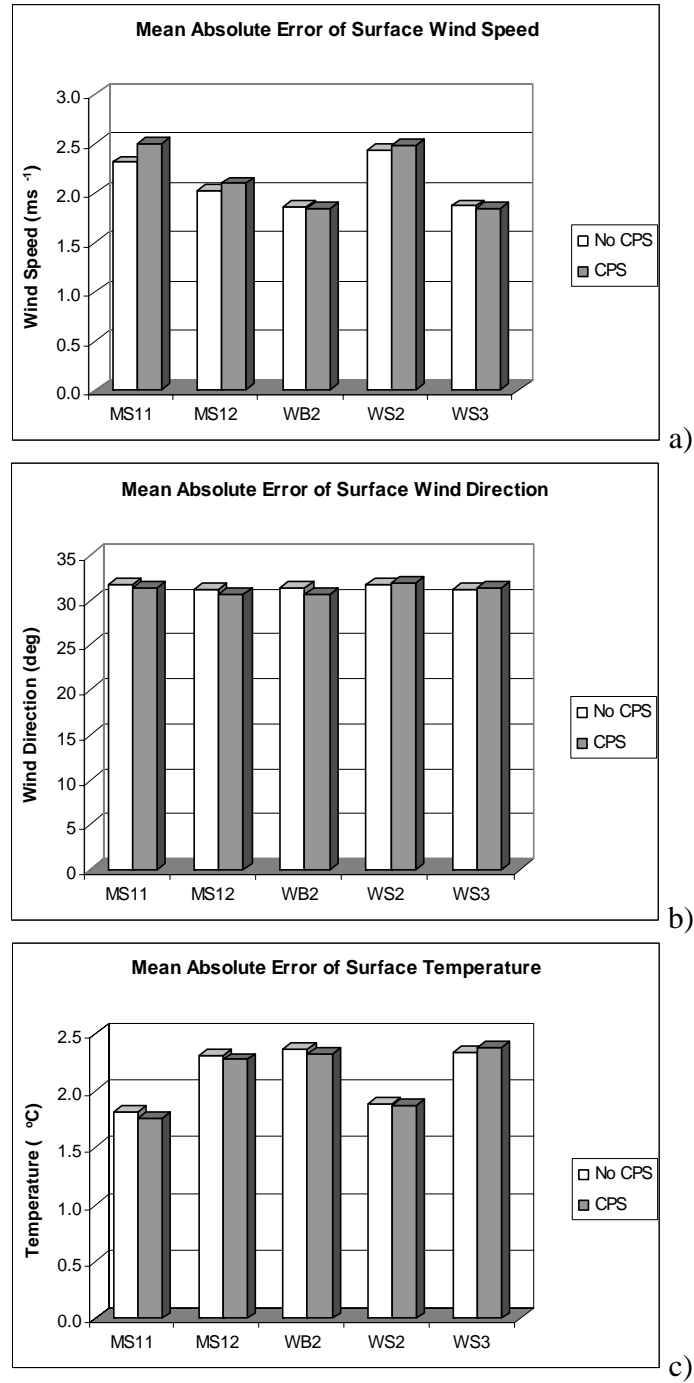
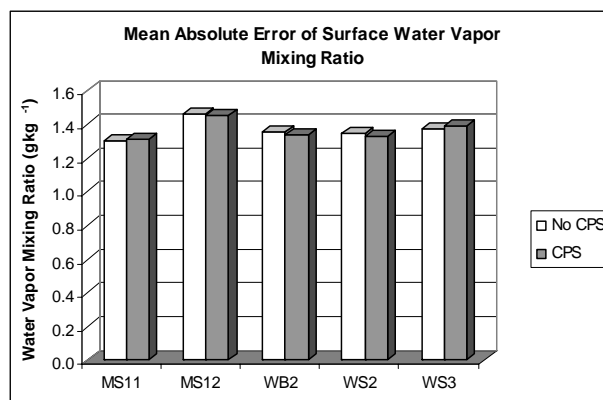
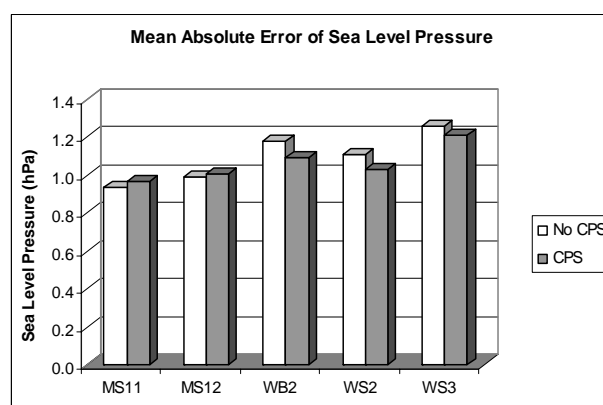


Figure 38 Model-simulated mean absolute error (MAE) for the surface layer averaged over the period 1200 UTC 18 September – 1800 UTC 19 September 1983, for all experiments both with and without convective parameterization scheme (CPS). a) wind speed (ms<sup>-1</sup>), b) wind direction (deg), c) temperature (C), d) vapor mixing ratio (g kg<sup>-1</sup>) and e) sea-level pressure (mb).



d)



e)

Figure 38 (Continued)

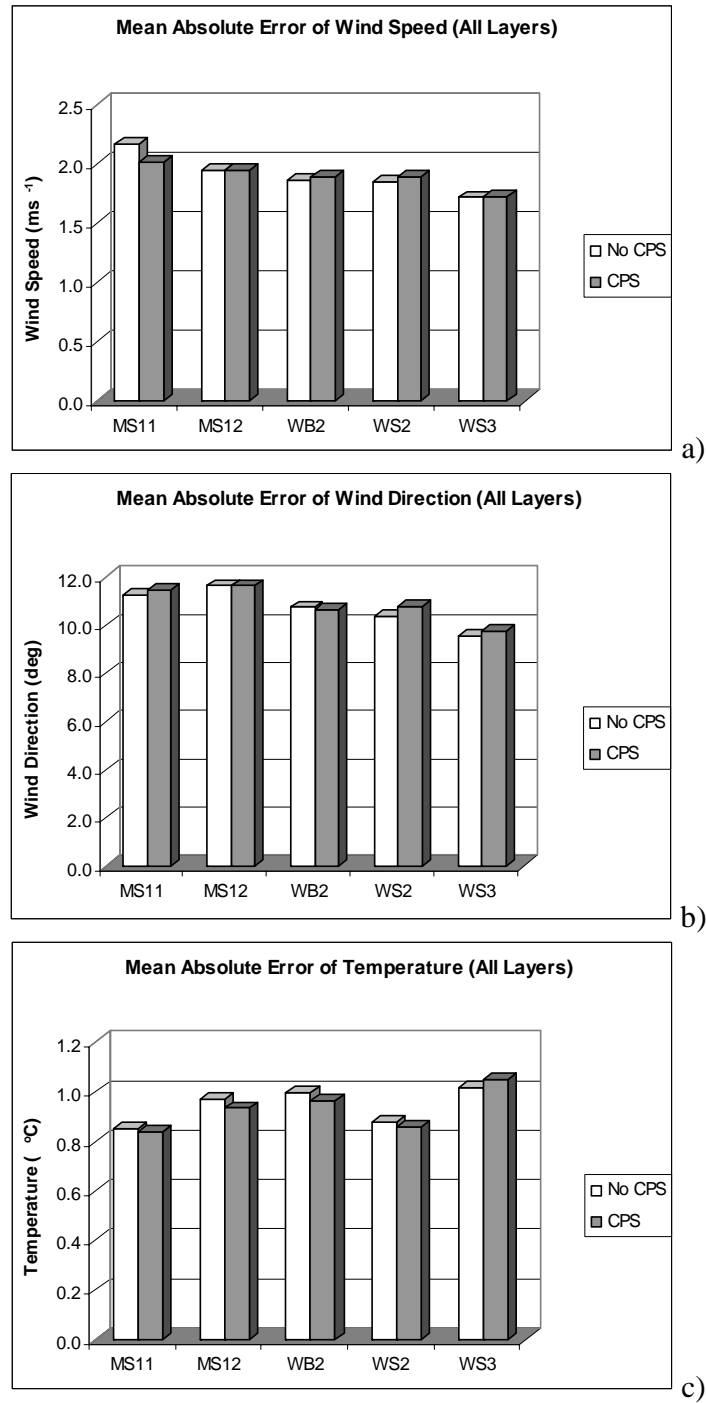


Figure 39 Model-simulated mean absolute error (MAE) averaged over all layers over the period 1200 UTC 18 September – 1800 UTC 19 September 1983, for all experiments, both with and without convective parameterization scheme (CPS). a) wind speed (ms<sup>-1</sup>), b) wind direction (deg), c) temperature (C) and d) vapor mixing ratio (g kg<sup>-1</sup>).

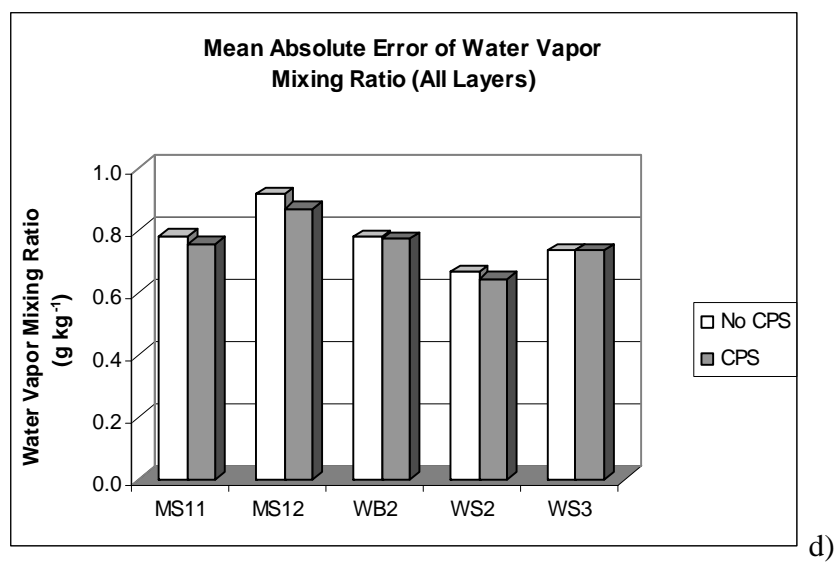


Figure 39 (Continued)